Fractional Fourier-Based Filtering and Applications

Subramaniam, Suba Raman

Awarding institution:
King's College London

DIVISION OF ENGINEERING

KING'S College LONDON

PhD Thesis

FRACTIONAL FOURIER-BASED FILTERING AND APPLICATIONS

by

SUBA RAMAN SUBRAMANIAM

June 2013

DECLARATION

This thesis was submitted to the Division of Engineering (King's College London) as part of the requirements of the PhD course and is solely the original work of its author, except where clearly specified otherwise. It has not been previously submitted to this or another university.

Supervised by:

DR. APOSTOLOS GEORGAKIS

Examined by:

PROFESSOR COLIN COWAN

PROFESSOR CAGATAY CANDAN

Date Examined: 07 February 2013

To everyone who has made this journey possible.

List of Contents

Acknowledgement

I would like to thank a lot of people for their contribution in completing this project, but my foremost gratitude goes to my supervisors, Dr. Apostolos Georgakis, Dr. Jeffrey Bamber and Dr. Wing-Kuen Ling for their immeasurable patience, guidance and support throughout the duration of the project. I am particularly grateful for the insightful suggestions that Dr. Apostolos Georgakis had provided me during the write-up of this dissertation.

I would also like to thank Dr. Mike Clode, Dr. Mahbub Gani, and Dr. Efstathios Kaliviotis for their individual support and words of encouragement.

Special thanks to Ji, Thomas, and Krishna for their lovely company during my time in the DSP research group.

Most importantly, I do not think that the completion of this project would have been possible if it was not for my family members. In particular, I would like to deeply thank my grandparents, parents, brother, uncle and aunty for their constant care and undivided support during the duration of this project.

Lastly, I would like to thank Dr. Gunasingam for his words of inspiration and spiritual guidance throughout my PhD.

FRACTIONAL FOURIER-BASED FILTERING AND APPLICATIONS

Fractional Fourier theory has provided a generalization of the classical Fourier transform, and as a result has become a rich area of new concepts and applications. For instance, the implicit relationship that exists between the fractional Fourier transform (FrFT) and time-frequency representations has revealed a continuum of time-frequency (T-F) rotated domains of which the well-known frequency domain is simply a special case. Consequently, the existence of such domains allows for the generalization of Fourier filtering in ways that make it possible to easily realize various time-varying operators. This can in turn lead to more effective signal processing approaches for a range of practical applications.

The main focus of this thesis is on the novel concept of fractional Fourier-based filtering. Particularly the work looks into the design of single, as well as multi-stage, systems for the restoration of both simulated and real-world signals. The thesis starts by first examining some of the essential properties of the fractional Fourier transform which relate to filtering. Precisely, the concept of rotated domains in the joint time-frequency plane is elaborated and further exploited for filtering. Results and improvements achieved are demonstrated and discussed through different application examples over the chapters of this thesis.

FRACTIONAL FOURIER-BASED FILTERING AND APPLICATIONS

Prominent contributions of this work include:

- A first time application of FrFT-based filtering on real-world signals. The structure of the proposed denoising circuit is informed by the prior design of the time-varying low-pass cutoff threshold in the T-F plane
- A novel derivation for optimized FrFT-based filtering in a single-stage system, which has distinct advantages over existing formulations
- A first time generalization, of the above single-stage derivation into an optimized multiple-stage formulation in which discrete FrFTs are directly engaged

Author's Publications

[1] A. Georgakis, and S. R. Subramaniam, "Estimation of the second derivative of kinematic impact signals using fractional Fourier filtering", **IEEE Trans. Biomed. Eng.**, vol. 56, pp. 996-1004, 2009.

[2] S. R. Subramaniam, and A. Georgakis, "A Simple Filter Circuit for denoising Biomechanical Impact Signals", **31st Annual International Conference of the IEEE Engineering in Medicine and Biology Society (EMBC)**, 2009, Minneapolis, Minnesota.

[3] S. R. Subramaniam, and A. Georgakis, "Fractional Fourier-based denoising of kinematic signals with multiple impacts", **10th International Symposium on Information Science, Signal Processing and their Applications (ISSPA)**, 2010, Kuala Lumpur, Malaysia.

[4] S. R. Subramaniam, Tsz K. Hon, A. Georgakis, and George Papadakis "Fractional Fourier-Based Filter for denoising Elastograms", **32nd Annual International Conference of the IEEE Engineering in Medicine and Biology Society (EMBC)**, 2010, Buenos Aires, Argentina.

[5] S. R. Subramaniam, Tsz K. Hon, Bingo Wing-Kuen Ling, and A. Georgakis, "Optimal Two-Stage Filtering of Elastograms", **33rd Annual International Conference of the IEEE Engineering in Medicine and Biology Society (EMBC)**, 2011, Boston, Massachusetts.

[6] S. R. Subramaniam, B. W.-K. Ling, and A. Georgakis, "Filtering in rotated time-frequency domains with unknown noise statistics", **IEEE Trans. Signal Process.**, vol. 60, no. 1, pp. 489 - 493, January 2012.

[7] S. R. Subramaniam, Bingo Wing-Kuen Ling, and A. Georgakis, "Motion Artifact Suppression in the ECG Signal by Successive Modifications in Frequency and Time", **35th Annual International Conference of the IEEE Engineering in Medicine and Biology Society (EMBC)**, 2013, Osaka, Japan.

Chapter 1

Introduction

The fractional Fourier transform (FrFT) can be considered as a generalization of the classical Fourier transform with an order parameter *a*. Mathematically, the a^{th} order fractional Fourier transform F^a refers to the a^{th} power of the classical Fourier transform operation F [1]. As such, the first-order fractional transform (i.e. $a = 1$) of a function is equal to its classical Fourier transform, whereas the zero-order fractional transform (i.e. $a = 0$) is the identity operator.

Fractional Fourier domains are unique domains which can be represented as rotated axes in the time-frequency (T-F) plane. In fact, it has been shown that, the FrFT can be seen as a rotational operation since the T-F distribution of the a^{th} order fractional Fourier transform of a function *f(t)*, can be obtained by simply rotating the T-F distribution of *f(t)* by $a\pi/2$ [2]. Thus, it can be observed that the well-known frequency domain is in fact a special case (i.e. when $a = 1$) of the FrFT operator.

The FrFT has made possible the introduction of new approaches for signal processing, such as the generalization of classical Fourier based filtering to fractional Fourier domains. Figure 1-1a illustrates the process of filtering in a single-stage system. The observed signal *y(t)* is first transformed into the a^{th} fractional Fourier domain, where it is multiplied with an appropriate window function. The modified signal is then transformed back into the time domain. This process of filtering can also be performed consecutively to form a multiple-stage system, as shown in Figure 1-1b. The aim of this thesis is to present the author's contributions to the advancement of this type of FrFT-based filtering.

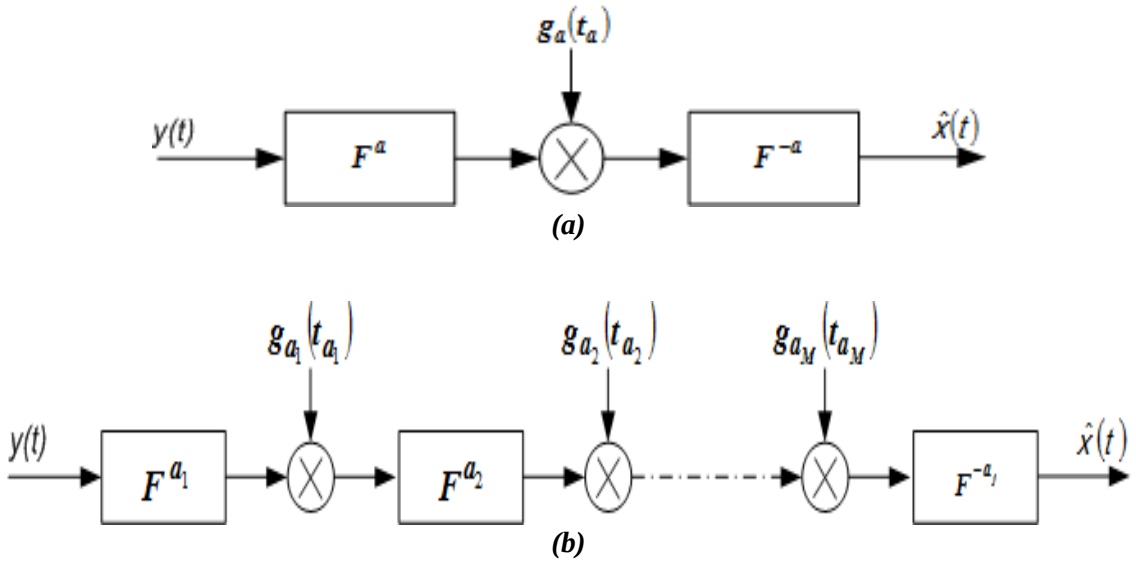

Figure 1-1 *Block diagram of* ***(a)*** *single-stage FrFT filter* ***(b)*** *multi-stage FrFT filter.*

1.1 Early Years/History

The notion of filtering in fractional Fourier domains was first described in 1994 by *Ozaktas et al.* [3], where they argued that two non-overlapping signal areas in the T-F plane could be separated through FrFT-based operations. This idea was reiterated by *Almeida et al.* [2] in the context of the closely related "swept-frequency filters". The idea was then put to the test for the first time in [4], where a filtering experiment based on an optical setup was described. The results, indicated that a signal corrupted by two chirp-like components can easily be removed in two consecutive fractional Fourier domains by a simple spatial band-stop filter, applied in each stage. The fractional orders used to obtain the most suitable domains ($\boldsymbol{a_{opt}}$) were determined manually by the theoretical slopes of the chirp components. Based on the above concept, the authors of [5] introduced "strip filters", and presented a simple signal separation example as an indication of the potential of this approach.

The possibility of filtering optimally in fractional Fourier domains was investigated in [1], [6], [7], [8], [9], and [10]. The first attempt was made in 1995 by *Kutay et al.* [6], where an optimised filtering function operating in a single fractional Fourier domain was

proposed. This filtering function was derived such that it minimized the mean-square-error (MSE) between the desired signal and the output of the system. The presented solution is completely analogous to the formulation of the classical optimal Wiener filtering problem. Some preliminary results were shown in [6]. This was then followed by a more extensive review conducted in 1997 by the same authors [7], which included more examples, a lengthy derivation and detailed implementation steps of the system both in continuous- and discrete-time cases. Furthermore in [8], *Kutay et al*. also proposed an alternative method of synthesizing/approximating a known general optimum linear system as a fractional Fourier domain filtering configuration. Since, this approach requires knowledge of the general linear estimator for a given application; it is more useful as a performance comparison between the two systems, rather than of any practical use. The most suitable fractional orders ($\boldsymbol{a_{opt}}$) used in [6], [7], and [8] were found by simply calculating the MSE for finely sampled values of a and choosing the one that minimizes the MSE – a trial-and-error approach.

The concept of consecutive filtering in more than one domain was discussed in [9] and [10]. The multi-stage system considered there, was a filtering configuration similar to that of Figure 1-1b with the exception that the ordinary Fourier operator was exclusively used. A way of optimising these repeated operations in the conventional time and frequency domains was also presented. Experimentation based on computer simulations showed that significant advantages can be achieved as compared to single-stage filtering. Further examples showing the potential usefulness of the above approach have been presented in Chapter 10 in [1].

The idea of filtering in fractional Fourier domains has been revisited recently in [11] and [12]. Precisely, in [11] new relations were derived between the Gabor transform and the FrFT, which provided additional proofs of the rotational effect of the FrFT in the T-F plane. This then naturally led to the re-introduction of the concept of fractional Fourier-

based filtering. Additionally, the authors in [11] also introduced the Gabor-Wigner distribution which they claimed to be a much better platform for determining the crucial parameters needed for fractional filtering (i.e. the most suitable fractional order and the filtering cutoff thresholds). Similarly in [12], the same authors also suggested that by using a time-frequency representation to design a time-varying filter, one could essential optimize the passband area of the filter such that the effect of noise can be reduced. In particular, they showed that the power of the remaining noise was lower when a two-stage rather than a single-stage system was used.

1.2 FrFT-Based Filtering Applications

It is only in the past decade that the concept of FrFT-based filtering has found applications in real-world problems, such as ultrasound [13]-[16], radar signal processing [18]-[22], and biomechanics [23, 24].

In ultrasound, FrFT-based filtering is especially useful in the analysis of ultrasonic measurements produced when layered structures are encountered. Due to the different physical properties in each layer, the transmitted chirp signal suffers from successive reflections in each layer [16], creating temporally overlapping echoes in the received signal. Thus, the FrFT is used for separating these echoes which incidentally are also chirped signals. The process of separation described in [13]-[16] can be generalised using Figure 1-1a which is as follows; firstly, the corrupted signal is transformed into the most suitable a^{th} domain, which was obtained by computing the following [17]:

$$\boldsymbol{a_{opt} = -\frac{2}{\pi}\tan^{-1}\left(\frac{{f_s}^2/N}{2b}\right)} \tag{1.1}$$

where f_s is the sampling frequency, N is the total number of samples and b is the desired chirp rate. This is then followed by a multiplication of the transformed signal with a

rectangular window function, whose width is designed such that it maximises the main lobe of the desired signal. Finally an inverse transform is performed to convert the filtered signal back in time again. As a conclusion, it was stated in [14] that this FrFT-based signal separation technique showed great potential due its ability to decompose overlapping signals in the T-F plane.

Another area where FrFT-based filtering has made a significant impact is in the field of radar signal processing [18]-[22]. For example, in [18] this concept of filtering was used iteratively to jointly detect strong moving objects and weak targets in airborne synthetic aperture radar (SAR) tracking. Existing techniques, such as classical Fourier-based filtering methods cannot efficiently isolate a particular object due the overlapping nature of other random targets and noise from background clutter. The process of filtering described in [18] is based upon the aforementioned single-stage filtering. The most suitable fractional order ($\boldsymbol{a_{opt}}$) was obtained using an exhaustive search similar to [7]. Meanwhile, the filtering function used was a narrow bandstop filter, whose center frequency was designed to match the center of the desired signal's narrowband spectrum. Results depicted, show that the FrFT-based filtering can substantially improve target detection in airborne SAR tracking.

A similar outcome was also reported in [19], where the FrFT denoising scheme was used to enhance monopulse radar tracking. Specifically, optimised fractional Fourier domain filtering was utilised to remove unwanted targets appearing in the look direction of the monopulse main beam [19]. It was further described that since the desired object can be modelled by a chirp signal, the most suitable fractional order could also be calculated using (1.1). The filtering steps were adopted from the discrete implementation of [7]. A further extension of this work was later presented in [20], where the same authors had implemented the single-stage FrFT filtering scheme to a pre-filtered version of a signal containing high power interference. As before, the most suitable order was obtained using

(1.1). However in this case, the filtering function used was simply a rectangular window, in which the width was manually designed to capture the region of maximum signal magnitude in the most suitable fractional Fourier domain. Results presented in [20], indicated that the proposed algorithm can successfully decrease the high power noise interference, and thereby improve the SNR of the recovered radar signal.

In the applications described above, the desired signal is always of chirped nature (i.e. the spectral content varies linearly with time). This is expected since the definition of the FrFT (which will be explored in Chapter 2) is appropriate for recovering these types of signals. However, this concept of filtering can also be used in denoising non-chirped signals. In [23, 24], an application of the FrFT-based filtering on signals whose spectral content do not vary linearly with time was presented. In fact, the proposed filter was applied to signals that exhibited considerable changes of their frequency content at distinct points in time. It should also be noted that this was the first time that a two-stage filtering scheme was applied to a real-world problem. The particular application considered experimentally acquired biomechanical signals, with the purpose of accurately estimating their second derivatives. The structure of the proposed denoising circuit was informed by the prior design of the time-varying low-pass cutoff threshold in the T-F plane. This implied that one could calculate the necessary fractional orders geometrically from the T-F plane. The proposed method compared favourably with existing conventional techniques and alternative advanced approaches.

1.3 Thesis Overview

This work focuses upon signal denoising and recovery using fractional Fourier-based filtering. Precisely these filters are applied to deal with specific problems in real-world applications, such as filtering of biomechanical impact signals, ultrasound elastography,

and ECG enhancement. In addition to this, novel derivations for optimised FrFT-based filtering in the least square-sense, in single and multiple-stage systems are also proposed.

The outline of the thesis is as follows. Chapter 2 describes the necessary background on the fractional Fourier transform and some of its essential properties with respect to filtering.

Chapter 3 presents the application of fractional Fourier transform in the context of filtering. In particular, a specific type of low-pass filters with time-varying cut-off thresholds is proposed, which can be realised by operating in distinctive fractional Fourier transform domains, to be applied in real-world problems. Comparisons will be shown between the suggested filters and current techniques for validation purposes. The work described in this chapter is primarily a continuation from earlier contributions on this topic [23, 24].

Chapters 4 & 5, explores the possibility of optimally designing single-stage and multi-stage fractional Fourier-based filtering configurations, respectively. Particularly in chapter 4, the optimization of single-stage configurations is revisited and an alternative solution is introduced which has particular advantages over existing ones. Similarly, in chapter 5, non-trivial challenges faced in optimizing multi-stage configurations are addressed and an optimal formulation in the least-square sense for this case is suggested for the first time in the literature.

References

[1] H. M. Ozaktas, Z. Zalevsky, and M. A. Kutay, The Fractional Fourier Transform with Applications in Optics and Signal Processing. New York: Wiley, 2001.

[2] L. B. Almeida, "The Fractional Fourier-Transform and Time-Frequency Representations," IEEE Transactions on Signal Processing, vol. 42, no. 11, pp. 3084-3091, Nov, 1994.

[3] H. M. Ozaktas, B. Barshan, and D. Mendlovic, "Convolution, Filtering, And Multiplexing In Fractional Fourier Domains And Their Relation To Chirp And Wavelet Transforms," Journal of the Optical Society of America A-Optics Image Science and Vision, vol. 11, no. 2, pp. 547-559, Feb, 1994.

[4] R. G. Dorsch, A. W. Lohmann, and Y. Bitran, "Chirp Filtering In The Fractional Fourier Domain," Applied Optics, vol. 33, no. 32, pp. 7599-7602, Nov 10, 1994.

[5] B. A. Weisburn, and R. G. Shenoy, "Time-frequency strip filters," IEEE International Conference on Acoustics, Speech, and Signal Processing, Vols 1-6, pp. 1411-1414, 1996.

[6] M. A. Kutay, H. M. Ozaktas, L. Onural, and O. Arikan, "Optimal Filtering In Fractional Fourier Domains," 1995 International Conference on Acoustics, Speech, and Signal Processing - Conference Proceedings, Vols 1-5, pp. 937-940, 1995

[7] M. A. Kutay, H. M. Ozaktas, and O. Arikan, "Optimal filtering in fractional Fourier domains," IEEE Transactions on Signal Processing, vol. 45, no. 5, pp. 1129-1143, May, 1997.

[8] M. A. Kutay. Generalized filtering configurations with applications in digital and optical signal and image processing. Ph.D. Thesis, Bilkent University, Ankara, 1999.

[9] M. F. Erden, and H. M. Ozaktas, "Synthesis of general linear systems with repeated filtering in consecutive fractional Fourier domains," Journal of the Optical Society of America A-Optics Image Science and Vision, vol. 15, no. 6, pp. 1647-1657, Jun, 1998.

[10] M. F. Erden, M. A. Kutay, and H. M. Ozaktas, "Repeated filtering in consecutive fractional Fourier domains and its application to signal restoration," IEEE Transactions on Signal Processing, vol. 47, no. 5, pp. 1458-1462, May, 1999.

[11] S.-C. Pei, and J.-J. Ding, "Relations between Gabor transforms and fractional Fourier transforms and their applications for signal processing," IEEE Transactions on Signal Processing, vol. 55, no. 10, pp. 4839-4850, Oct, 2007.

[12] S.-C. Pei, and J.-J. Ding, "Fractional Fourier Transform, Wigner Distribution, and Filter Design for Stationary and Nonstationary Random Processes," IEEE Transactions on Signal Processing, vol. 58, no. 8, pp. 4079-4092, Aug, 2010.

[13]M. Bennett, S. McLaughlin and T. Anderson, “Filtering of chirped ultrasound echo signals with the fractional Fourier transform,” IEEE International Ultrasonics Symposium, Vols 1-3, pp. 2036-2040, 2004.

[14]D. M. J. Cowell, and S. Freear, “Separation of Overlapping Linear Frequency Modulated (LFM) Signals Using the Fractional Fourier Transform,” IEEE Transactions on Ultrasonics, Ferroelectrics, and Frequency Control, vol. 57, no. 10, pp. 2321-2333, Oct, 2010.

[15]S. Harput, D. M. J. Cowell, J. A. Evans, N. Bubb, and S. Freear, “Tooth Characterization using Ultrasound with Fractional Fourier Transform,” IEEE International Ultrasonics Symposium, Vol. 1, pp. 1906-1909, 2009.

[16]S. Harput, T. Evans, N. Bubb, and S. Freear, “Diagnostic Ultrasound Tooth Imaging Using Fractional Fourier Transform,” IEEE Transactions on Ultrasonics Ferroelectrics and Frequency Control, vol. 58, no. 10, Oct, 2011.

[17]C. Capus and K. Brown, “Short-time fractional fourier methods for the time-frequency representation of chirp signals,” J. Acoust. Soc. Am., vol. 113, pp. 3223–3263, 2003.

[18]H. Sun, G. S. Liu, H. Gu, and W. M. Su, “Application of the fractional Fourier transform to moving target detection in airborne SAR,” IEEE Transactions on Aerospace and Electronic Systems, vol. 38, no. 4, pp. 1416-1421, Oct, 2002.

[19]S. A. Elgamel, and J. Soraghan, “Enhanced monopulse tracking radar using optimum fractional Fourier transform,” IET Radar Sonar and Navigation, vol. 5, no. 1, Jan, 2011.

[20]S. A. Elgamel, and J. Soraghan, “Using EMD-FrFT Filtering to Mitigate Very High Power Interference in Chirp Tracking Radars,” IEEE Signal Processing Letters, vol. 18, no. 4, pp. 263-266, Apr, 2011.

[21]C. Candan, "On the Implementation of Optimal Receivers for LFM Signals Using Fractional Fourier Transform," 2008 IEEE Radar Conference, pp. 1833-1836, May, 2008.

[22]C. Candan, "On the Optimality of Detectors Defined Over The Ambiguity Plane," 2009 IEEE Radar Conference, pp. 1082-1086, May, 2009.

[23]S.R. Subramaniam. Filtration of Non-Stationary Signals In the Fractional Fourier Domain: Accurate Estimation of the Acceleration of Impact Signals. MSc. Thesis, King’s College London, London, 2007.

[24]A. Georgakis, and S.R. Subramaniam, “Estimation of the second derivative of kinematic impact signals using fractional Fourier filtering”, IEEE Trans. Biomed. Eng., vol. 56, pp. 996-1004, 2009.

Chapter 2

The Fractional Fourier Transform

In this chapter the fractional Fourier transform (FrFT) and some of its fundamental properties will be presented. In particular, the unique relationship that exists between the FrFT and the Wigner distribution, which is a type of Time-Frequency distribution (TFD) that belongs to the Cohen class, will be drawn upon. Furthermore, it will be shown here that by exploiting this distinctive relationship, certain time-varying filtering operations can easily be implemented. In addition to this, the discrete fractional Fourier transform will also be briefly discussed. Some of the material in this chapter has been reported in [1], [2].

Introduction

As briefly mentioned in Chapter 1, the fractional Fourier transform can be mathematically defined as the a^{th} power of the classical Fourier transform operator F. Incidentally, the idea of fractional powers of the Fourier operator has appeared in mathematical literature as early as 1929 [3]. The prospective of this concept has only been recently discovered in the filtering applications described in the previous chapter, during the last decade. The reason fractional Fourier transform has gained such an attention over the years can be described by its potential for generalization and improvement as compared to traditional transforms, like the classical Fourier transform.

Furthermore, the importance of time-frequency analysis methods in signal processing could also be said to be a contributing factor to the mounting popularity of the FrFT. Time-

frequency analysis mainly considers signals of time-varying nature, in which their spectral content evolves over time. These types of signals are also referred to as non-stationary signals. Such signals are best represented by time-frequency distributions (TFDs), which show the energy distribution of the signal over a two dimensional time-frequency space. There exists a unique relationship between the FrFT and TFDs, which will be explored in detail later in this chapter. In essence, the FrFT has a rotational effect on the TFD of a given signal in the T-F plane. This process is further referred to as a T-F rotation. Utilizing this effect, a variety of time-varying filtering operations can easily be realized and implemented.

Moreover, it will be shown in this and subsequent chapters that, it is possible to improve the performance of a filter circuit, by using fractional Fourier transform instead of the ordinary Fourier transform (FT). This means that in some cases filtering in fractional Fourier domains as opposed to the ordinary Fourier domain, would lead to much better results. Since the fractional transform can be computed in the same time as the ordinary Fourier transform, these performance improvements come at no additional cost [4].

2.1 The Formal Definition

The a^{th}-order FrFT of a given signal *x(t)*, can appropriately be defined as [4], [21,22]:

$$F^a[x(t)] = x_a(t_a) = \int B_a(t_a, t)x(t)dt \tag{2.1}$$

where,

$$B_a(t_a, t) = C_\phi exp\left\{i\pi\left(-2\frac{t_a t}{\sin\phi} + ({t_a}^2 + t^2)\cot\phi\right)\right\} \tag{2.2}$$

with,

$$C_\phi = \frac{exp\{-i[(\pi\, sgn(\sin\phi))/4 - \phi/2]\}}{\sqrt{|\sin\phi|}}$$

where $\phi = a\pi/2$, with a being a real number in the interval $0 < a < 2$.

The kernel (2.2) is defined separately for *a=0* and *a=2* so that $F^0[x(t)] = x_0(t_0) = x(t)$ and $F^2[x(t)] = x_2(t_2) = x(-t)$. Some fundamental properties of the FrFT can be defined as follows:

(i) The transformation is linear (i.e. $F^a[a_1x(t) + a_2y(t)] = a_1F^a[x(t)] + a_2F^a[y(t)]$).

(ii) The transformation is additive in index (i.e. $F^{a_2}\left[F^{a_1}[x(t)]\right] = F^{a_1+a_2}[x(t)] = x_{a_1+a_2}(t_{a_1+a_2})$).

Based on these properties, the definition of the FrFT can easily be extended outside the interval (-2, 2) by noting that $F^{4l+a}[x(t)] = F^a[x(t)]$ for any integer l.

Furthermore, it can be seen that the classical Fourier transform emerges as a special case of the FrFT for *a=1*, $F^1[x(t)] = x_1(t_1) = X(f)$. In particular, when *a=1*, $\phi = \pi/2$, thus reducing the transform kernel in (2.2) to $exp\{-2i\pi t_1 t\}$, which can immediately be identified as the Fourier transform operator. In the same way, for *a=-1*, $F^{-1}[x(t)] = x_{-1}(t_{-1}) = X(-f)$ is the inverse Fourier transform. Thus, it is clear that the ordinary *time* and *frequency* variables can be viewed as special cases of the fractional variable t_a,. If t_a plays the role of *fractional time*, then *fractional frequency* will be given by t_{a+1}, since $F^1[s_a(t_a)] = s_{a+1}(t_{a+1})$. It is also obvious that $F^2[s(t)] = s(-t)$, $F^3[s(t)] = S(-f)$, $F^4[s(t)] = s(t)$, etc.

2.1.1 Implementation of the Continuous-Time FrFT

The FrFT of a signal can easily be computed in continuous-time by considering the following [5]:

Firstly, let's express the argument of the chirp component in (2.2) as follows:

$$-2\frac{t_a t}{\sin\phi} + ({t_a}^2 + t^2)\cot\phi = -2t_a t\csc\phi + {t_a}^2\cot\phi + t^2\cot\phi \qquad (2.3)$$

Then (2.1) can now be expressed as,

$$F^a[x(t)] = x_a(t_a) = C_\phi \int exp\{i\pi(t^2 \cot\phi - 2t_a t \csc\phi + {t_a}^2 \cot\phi)\}x(t)dt \qquad (2.4)$$

$$x_a(t_a) = C_\phi exp\{i\pi {t_a}^2 \cot\phi\} \int [x(t)exp\{i\pi t^2 \cot\phi\}]exp\{-i2\pi t(t_a \csc\phi)\}dt \qquad (2.5)$$

Thus from (2.5), it can be observed that the fractional Fourier transform of a signal can be implemented sequentially in 4 distinct steps:

1) Multiplying the signal with the scaled chirp component, $exp\{i\pi t^2 \cot\phi\}$
2) Performing the Fourier transform with the argument scaled by $\csc\phi$
3) Multiplying the result with another scaled chirp component, $exp\{i\pi {t_a}^2 \cot\phi\}$
4) Scaling the amplitude by C_ϕ

The above steps can also be visualized in the figure below:

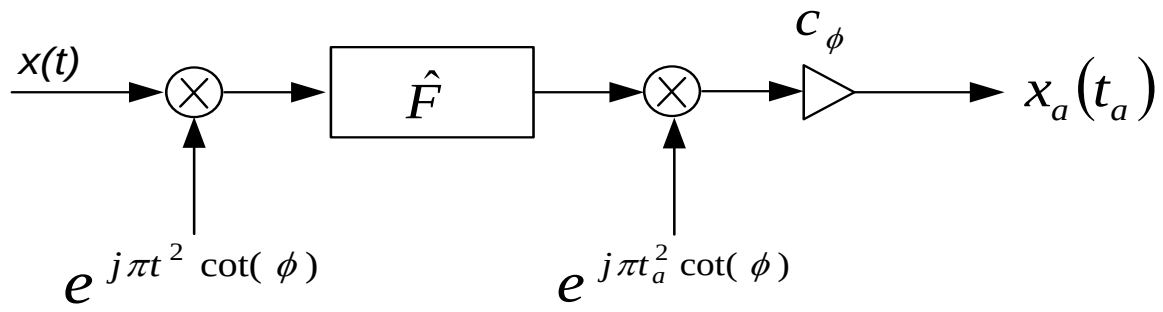

Figure 2-1 *Computation of the FrFT in continuous-time, where $\hat{F}$ represents the scaled Fourier operator.*

2.1.2 Rotation Interpretation in the Time-Frequency Plane

As with the classical Fourier transform, the eigenfunctions of the FrFT are also the Hermite-Gaussian functions $\psi_n(t)$ [4],

$$F^a[\psi_n(t)] = e^{-ian\pi/2}\psi_n(t_a) \qquad . \qquad (2.6)$$

The n[th]-order Hermite-Gaussian functions, which are known to form a complete and orthonormal set for the signal space $\mathcal{L}_2$, can be defined as follows:

$$\psi_n(t) = \frac{2^{1/4}}{\sqrt{2^n n!}} H_n(\sqrt{2\pi}t)e^{-\pi t^2} \qquad , \qquad (2.7)$$

where $H_n(t)$ is the nth-order Hermite polynomial,

$$H_n(t) = (-1)^n e^{t^2} \frac{d^n}{dt^n}\left(e^{-t^2}\right) \quad .$$

Consequently, the transform kernel in (2.2) can be expanded as follows [4]:

$$B_a(t_a, t) = \sum_{m=0}^{\infty} \psi_m [t_a] e^{-jam\frac{\pi}{2}} \psi_m[t] \quad . \tag{2.8}$$

In the light of the above, (2.1) can be interpreted as an inner product decomposing the signal into the Hermite-Gaussian basis. This can also be achieved by invoking the rotation operator defined by Folland [6]. This operator is similar to the FrFT in terms of its transform kernel and eigenfunctions, and has been used to effect T-F rotations for the implementation of 'strip filters' in [7], [8]. Therefore, it can be concluded that the FrFT is a transform which can be interpreted as a rotation operator in the T-F plane. This concept has been presented in more detail by *Almeida et al.* in [9].

2.2 Rotated Time-Frequency Domains

Traditionally, the *time* and *frequency* domains are represented in the T-F plane as a horizontal and a vertical axis, respectively. The right angle between them is in agreement with the geometric interpretation of the classical Fourier transform (FT) as a 90-degree rotation of the T-F coordinate system, which can be visualized in Figure 2-2. To illustrate this further, let's examine the Wigner distribution of a signal *x(t)*,

$$W_x(t, f) = \int x\left(t + \frac{\tau}{2}\right) x^*\left(t - \frac{\tau}{2}\right) e^{-j2\pi\tau f} d\tau \tag{2.9}$$

The Wigner distribution is a T-F representation of special theoretical importance because it satisfies a large number of mathematical properties, and thus provides a rigorous description of the T-F domain. Starting from (2.9) it is easy to show that if *X(f)* is the Fourier transform of *x(t)* then,

$$W_x(t, f) = W_X(f, -t) \tag{2.10}$$

which demonstrates that the representation of the signal in the T-F plane will be the same either the input is the original time waveform or its Fourier-transformed version, as long as the latter distribution is computed into its own coordinate system which is rotated anticlockwise by 90 degrees with respect to the horizontal time axis.

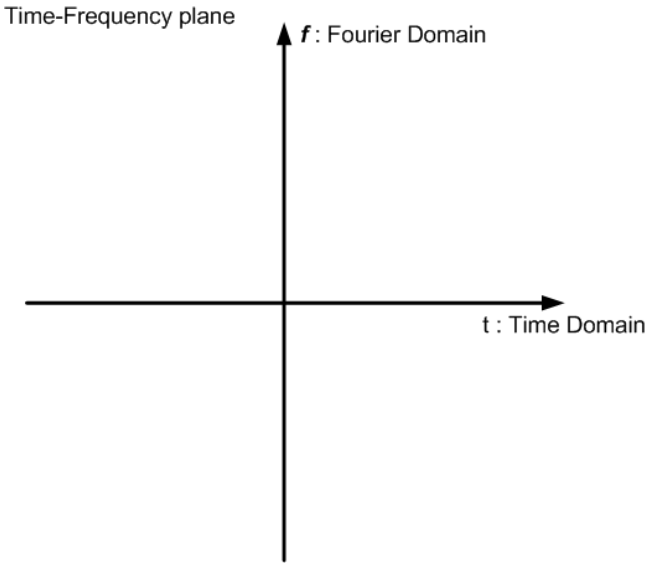

Figure 2-2:

*T-F coordinate system. Note that the frequency axis, **f** is orthogonal to the time axis, t.*

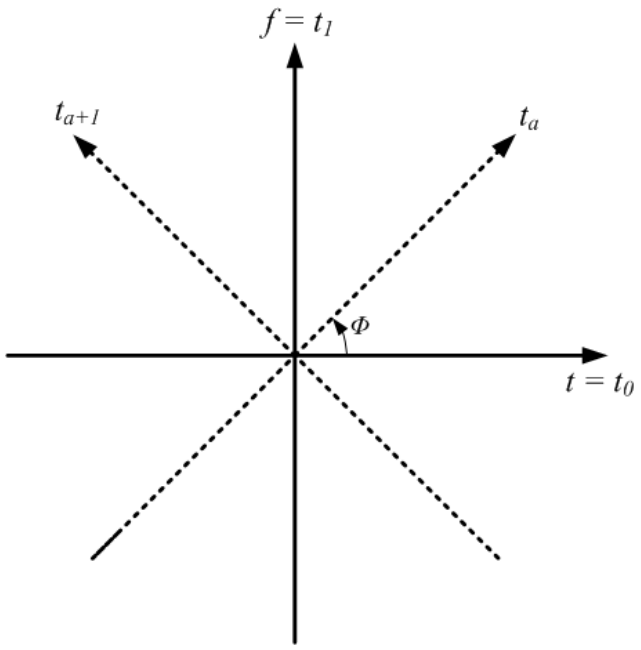

Figure 2-3:

Rotated coordinate system in the T-F plane.

Figure 2-3 depicts the rotational effect caused by the fractional Fourier transform in the T-F plane. The terms $t = t_0$ and $f = t_1$ are assumed to be the variables along *x*- and *y*– axis, respectively. This is similar to the time and frequency variables in the T-F plane, as depicted in Figure 2-2. If this coordinate system is rotated over an angle $\phi = a\pi/2$ (with *a* being a real number in the interval $0 < |a| < 2$.) counterclockwise (marked as the dotted axis in Figure 2-3), then the rotated variables will be denoted as t_a and t_{a+1} respectively. Furthermore, in accordance to the description provided in Section 2.1, this new rotated axes can also be termed as fractional axes.

2.2.1 Relationship between the FrFT and the Wigner Distribution

As shown in Figure 2-3, the FrFT can also admit a T-F rotation interpretation. This observation can further be supported by the following fundamental relationship between the FrFT and the Wigner distribution (WD) [9, 10],

$$W_{x_a}(t_a, t_{a+1}) = W_x(t_a \cos\phi - t_{a+1} \sin\phi\,, t_a \sin\phi + t_{a+1} \cos\phi) \tag{2.11}$$

As it was pointed out earlier, the WD possess several desirable mathematical properties and consequently, is considered to be a very important time-frequency analysis tool. One such property is the time and frequency marginals, which will be discussed shortly.

It can be observed that (2.11) is an extension of (2.10), signifying a counterclockwise rotation of the coordinate system by the angle ϕ. Therefore, the transformed signal $x_a(t_a)$ resides in a domain which can be symbolized as an oblique T-F axis at an angle ϕ with the horizontal time axis (as shown in Figure 2-3), hence the term 'rotated T-F domain'. Accordingly, the FrFT can be considered as a T-F rotation operator.

The aforementioned time and frequency marginals property refers to the projections of the energy distribution of a given signal in the time-frequency plane onto the time and frequency axes, respectively. They can be described by (2.12) and (2.13),

$$\int W_x(t,f)\,df = |x(t)|^2 \tag{2.12}$$

$$\int W_x(t,f)\,dt = |X(f)|^2 \tag{2.13}$$

Subsequently, an extension to the above, which is the *fractional marginal*, can similarly be expressed as:

$$\int W_{x_a}(t_a, t_{a+1})\,dt_{a+1} = |x_a(t_a)|^2 \tag{2.14}$$

Where $x_a(t_a) = F^1[x_{a-1}(t_{a-1})]$. Clearly, (2.12) and (2.13) are special cases of (2.14) for *a=0* and *a=1*, respectively. When (2.11) is inserted into (2.14) one can easily recognize that the integral in (2.14) becomes the Radon transform of the WD,

$$R_\phi[W_x] = \int W_x(t_a\cos\phi - t_{a+1}\sin\phi\,, t_a\sin\phi + t_{a+1}\cos\phi)\,dt_{a+1} \tag{2.15}$$

In light of (2.14) and (2.15), it becomes obvious that the integral projection of the WD of the original signal onto the oblique axis t_a (which makes angle ϕ with the time axis) equals the squared magnitude of the a^{th}-order FrFT of the signal. This further implies that the modification of a signal in a rotated domain will have an overall effect along the direction orthogonal to the corresponding axis in the T-F plane. A special case of this notion is the global effect that a fixed band-pass Fourier filter has on the entire time waveform.

Combining this property with the rotational effect induced by the FrFT in the T-F plane, a more effective method of filtering can be defined, which is filtering in rotated T-F domains. Precisely, a window $g_a(t_a)$ can be used to modify the signal in fractional frequency,

$$\hat{x}_a(t_a) = g_a(t_a)x_a(t_a)\,. \tag{2.16}$$

The equivalent process when operating directly in the T-F plane can be described by way of a convolution, along the fractional-time axis t_{a-1}, of the Wigner distributions of $g_{a-1}(t_{a-1})$ and $x_{a-1}(t_{a-1})$,

$$W_{\hat{x}_{a-1}}(t_{a-1}, t_a) = W_{g_{a-1}}(t_{a-1}, t_a) \;{}^{*}_{t_{a-1}}\; W_{x_{a-1}}(t_{a-1}, t_a)\,. \tag{2.17}$$

For the sake of visualizing the operation described in (2.16), one can consider a segment on the t_a axis – corresponding to a bandpass window – and expand it along the direction of the t_{a-1} axis to form a strip-shaped region. The outlined strip constitutes a slanted pass band in the T-F plane in the sense that any components lying outside this area will be eliminated by the process in (2.17). If the windowing in (2.16) takes place in the conventional frequency domain then the strip is parallel to the time axis and the result is an LTI filter. In any other case, one obtains a filter which is still linear but has a time-varying behavior.

2.2.2 Filtering in Rotated Time-Frequency Domains

As previously mentioned, the unique relationship that exists between the FrFT and the Wigner distribution has allowed the definition of an alternative and a more effective method of filtering. In filtering applications, a common goal is to restore an observed signal $y(t)$ which has been corrupted by additive noise. Significant performance advantages can be obtained if the filtering operation takes place in the domain in which either the signal or the noise (or both) are maximally concentrated. This may be a rotated T-F domain other than that of the ordinary frequency, depending on the orientation of the signal and noise components in the T-F plane.

To implement a rotated T-F domain-based filter the input signal should first be transformed into the related fractional frequency domain where it can then be multiplied with an appropriate window. The modified signal is finally transformed back into the time domain,

$$\hat{x}(t) = F^{-a}[g_a(t_a)\, y_a(t_a)]\,, \tag{2.18}$$

where $y_a(t_a) = F^a[y(t)]$. The configuration of the above system was shown in the block diagram of Figure 1-1a. Alternatively, since multiplication in fractional frequency is

equivalent to convolution in the associated fractional time – by virtue of the relevant property of the Fourier transform – the process in (2.18) can equally be performed as:

$$\hat{x}(t) = F^{-(a-1)}[g_{a-1}(t_{a-1}) * y_{a-1}(t_{a-1})] \,. \tag{2.19}$$

The function $g_{a-1}(t_{a-1})$ can be considered as the impulse response of the corresponding filter in fractional time, whereas $g_a(t_a)$ plays the role of the filter's fractional-frequency response. It is clear that conventional Fourier filtering is a special case of (2.18) for $a = 1$. Further to (2.19), it is straightforward to show that the multiplication-convolution duality also holds for fractional domains related by ordinary Fourier transform (that is, domains forming an angle of 90° between them in the T-F plane, as depicted in Figure 2-3). The fractional-time convolution property can be expressed as;

$$g_{a-1}(t_{a-1}) * y_{a-1}(t_{a-1}) \overset{FT}{\longleftrightarrow} g_a(t_a)\, y_a(t_a).$$

The flexibility offered by the parameter a is advantageous for signal separation and noise elimination applications, particularly in cases where desired and unwanted components exhibit minimal overlap in specific domains other than those of time or frequency. In [11], an optimized (in the mean square error (MSE) sense) filtering function $g_a(t_a)$ was analytically derived. The authors considered the observation model $y(t) = H[x(t)] + n(t)$, (where $H(\cdot)$ denotes a known linear degradation process), and further assumed that the autocorrelation functions of the signal $s(t)$ and noise $n(t)$ were known. The optimum fractional domain for the operation described in (2.18) was found by iteratively applying the optimized function $g_a(t_a)$ for different values of a, and choosing the one that minimized the MSE.

Further improvements in filtering performance can be achieved if more than one fractional Fourier domains are involved. A way of doing this is by repeated filtering in consecutive domains [2], [12], and [13]. Such a scheme can be formulated as follows,

$$\widehat{x(t)} = F^{-a_j}\left[g_{a_M}(t_{a_M})F^{a_M}\left[\dots\left[g_{a_2}(t_{a_2})F^{a_2}\left[g_{a_1}(t_{a_1})F^{a_1}[y(t)]\right]\right]\right]\right], \qquad (2.20)$$

Where $a_i$is the i^{th} FrFT domain, $g_{a_i}(t_{a_i})$ are the corresponding filtering functions, M is the total number of domains employed and a_j represents the cumulative sum of this total number, i.e. $a_j = \sum_{i=1}^{M} a_i$. The configuration of the above system was shown in the block diagram of Figure 1-1b. Obviously, when $\sum_{i=1}^{M} a_i = 4$, the inverse transformation is not required since the signal is already in the time domain. Similarly, if $\sum_{i=1}^{M} a_i = 2$, the result needs only to be time-reversed. It is also clear that instead of using inverse-FrFT at the end of the process, one can equally apply a suitable direct-FrFT to reach the time domain.

In [14], the authors had claimed that the operation of (2.20) was reduced to an equivalent form that employed only ordinary Fourier transforms. However, this claim has been somewhat inaccurate. As it was shown in [15], to construct this equivalent form one has to implement a structure similar to Figure 2-1 in between each fractional stage. In other words, the pre- and post- chirp multiplications of Figure 2-1 would have to be absorbed into the multiplicative filters, before and after each fractional transform stage and thus leaving only a scaled ordinary Fourier transform in between each stage. However, the solution provided in [14], does not employ the structure described in [15], and therefore is a mere implementation of repeated filtering in conventional Fourier domains. Incidentally, it was also pointed out in [3] that this equivalent form is not necessarily beneficial in practice since the modified filters often exhibit oscillatory behavior due to the included chirp components. Furthermore, this 'reduction configuration' may not be trivial to implement in discrete form due to the need of finely sampling chirp signals, and requirement of scaling (as shown in Figure 2-1). In fact, it was stated in [15] that one does not need to implement such a structure since there is no added advantage to the overall system.

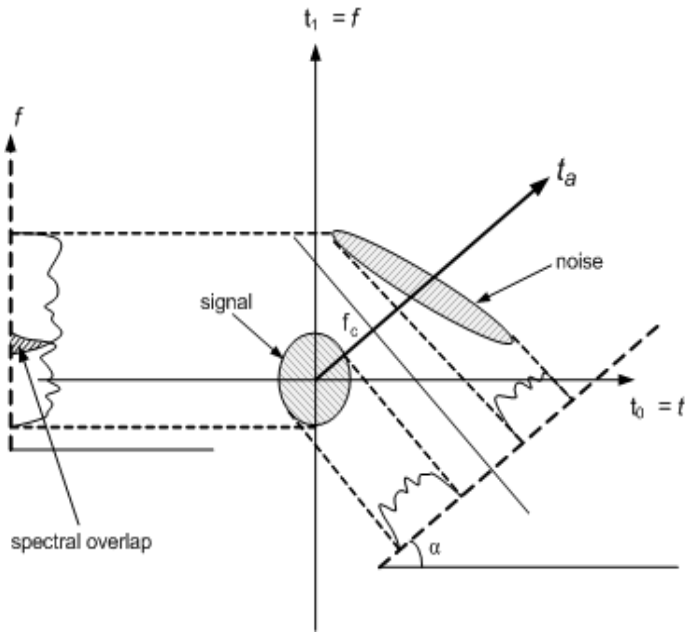

Figure 2-4a:

Visualization of a low-pass filtering effect in a single fractional Fourier domain.

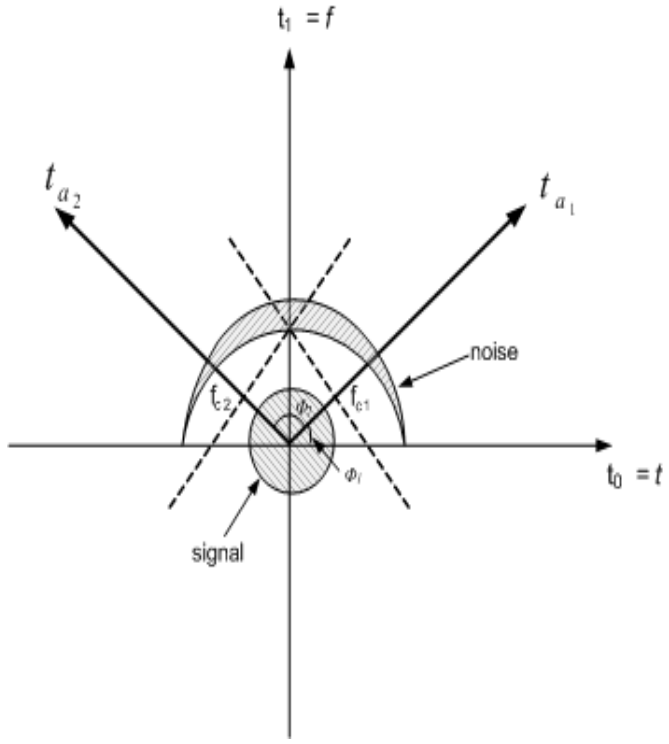

Figure 2-4b:

Visualization of repeated low-pass filtering effect in two fractional Fourier domains.

The ability to visualize fractional Fourier filtering operations in the T-F plane helps to both understand these processes and inform the design of appropriate filtering schemes. Figure 2-4 illustrates this by means of two tutorial examples. Figure 2-4a depicts a case where the spectra of the useful signal and the unwanted term overlap in the frequency axis. Thus, no Fourier-based method could accurately separate the two components, whereas a

simple low-pass filter with cutoff at f_c in the fractional Fourier domain specified in Figure 2-4a can easily discard the unwanted component. In more complex cases where no single fractional domain can be found to isolate the desired signal, the repeated use of fractional domain filtering could still provide a solution, as shown in Figure 2-4b. This should become clear shorty.

Furthermore based upon this concept of repeated filtering, different polygon-shaped passband regions can be implemented in the T-F plane with the number of vertices being equal to *2*n*, where *n* is the number of fractional domains involved. Figure 2-5 illustrates a rhombic passband region that can be achieved by filtering in two consecutive fractional domains. In this resulting rhombic passband region, the negative part is actually a direct consequence of the periodicity of the FrFT of the discrete-time impulse response of the applied filters.

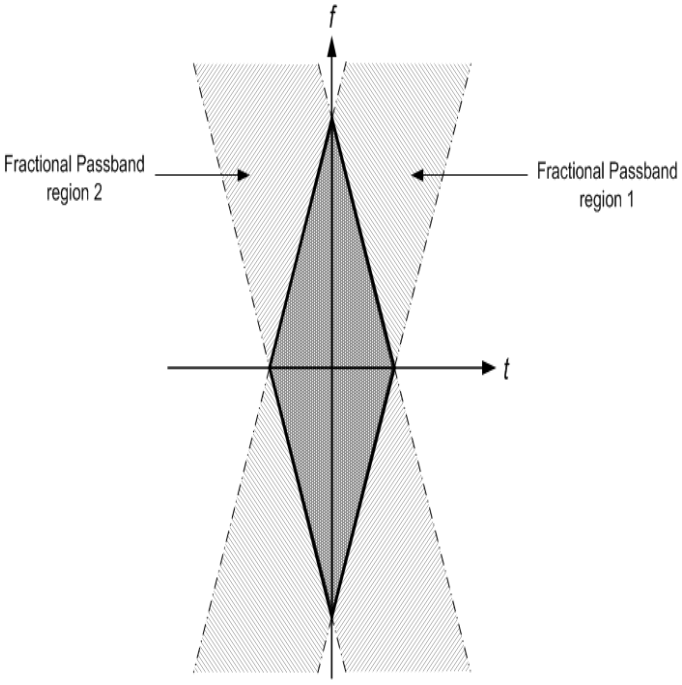

Figure 2-5:

The resulting rhombic passband region (dark grey-shaded area) of a repetitive Fractional Fourier filter based on two consecutive FrFT domains.

2.2.2.1 Rotated Time-Frequency Filtering Examples

This concept of filtering in rotated domains offers a unique opportunity to implement a number of time-varying filtering operations which otherwise would be impossible with

conventional filtering methods. This is especially valuable in signal denoising and recovery applications, when the corrupting noise overlaps with the useful signal components both in the classical time and frequency domains. As previously revealed, due to the global effect caused by conventional filtering methods, this type of overlapping noise can't easily be treated. Examples 2.1 and 2.2 have been provided to further demonstrate this scenario.

Example 2.1

Figure 2-6d depicts a Gaussian signal corrupted by a chirp component in the T-F plane. As clearly depicted in this figure, the two components cannot be effectively separated by conventional low-pass filtering in the Fourier domain. The equivalent operation in the T-F plane is shown in Figure 2-7b where the grey-shaded area represents the filter's passband region. Instead, if the signal is fractional Fourier-transformed (*a=0.5)* as shown in Figure 2-8, both components could easily be separated. The cutoff threshold of the filter in this fractional domain can now be drawn as a straight line normal to the axis $t_{0.5}$, in the same way that the cutoff threshold of a low-pass filter applied to an ordinary time waveform would appear as a straight line perpendicular to the frequency axis $f=t_1$. The equivalent cutoff threshold of this filtering operation is shown in Figure 2-9 as a straight line normal to the oblique axis $t_{0.5}$. Note that the method in which the appropriate order (i.e. rotational angle) was obtained will be discussed at the end of this chapter, in the appendix section.

So far in this example, the method described above essentially isolates the corrupting noise component (chirp signal) from the desired component (Gaussian signal) in a single rotated domain. Since the chirp signal used here has a strong directional orientation in the T-F plane, it can easily be eliminated in a single rotated domain. However, in most practical scenarios this may not be the case since the corrupting components could have a wide spread in the T-F plane. Thus, filtering in a single rotated domain would be

insufficient and the use of repeated filtering in consecutive domains may be necessary, as shown in the following example.

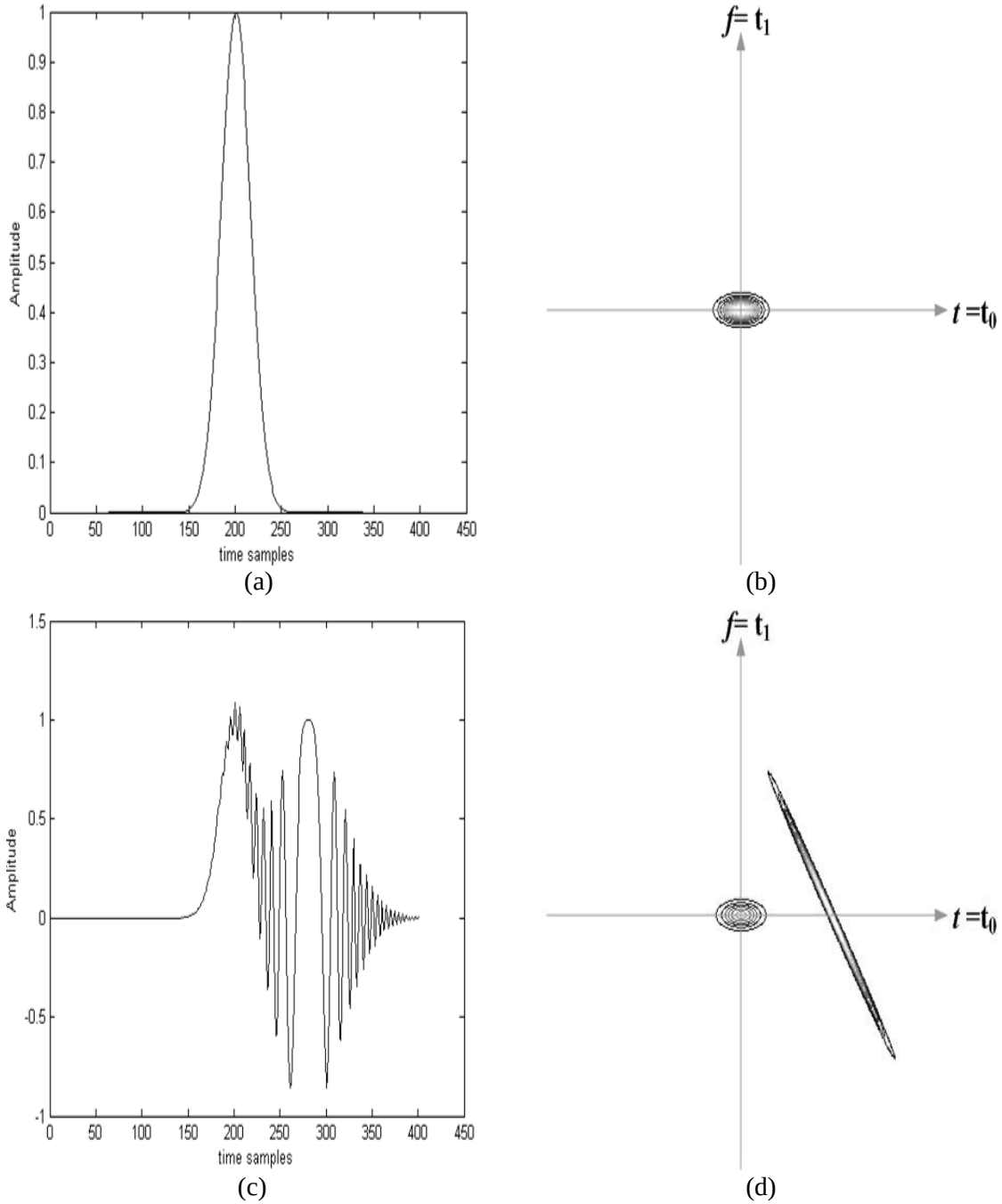

Figure 2-6 *(a) The ideal signal and (b) Time-Frequency distribution of the ideal signal. (c) The corrupted signal and (d) Time-Frequency distribution of the corrupted signal.*

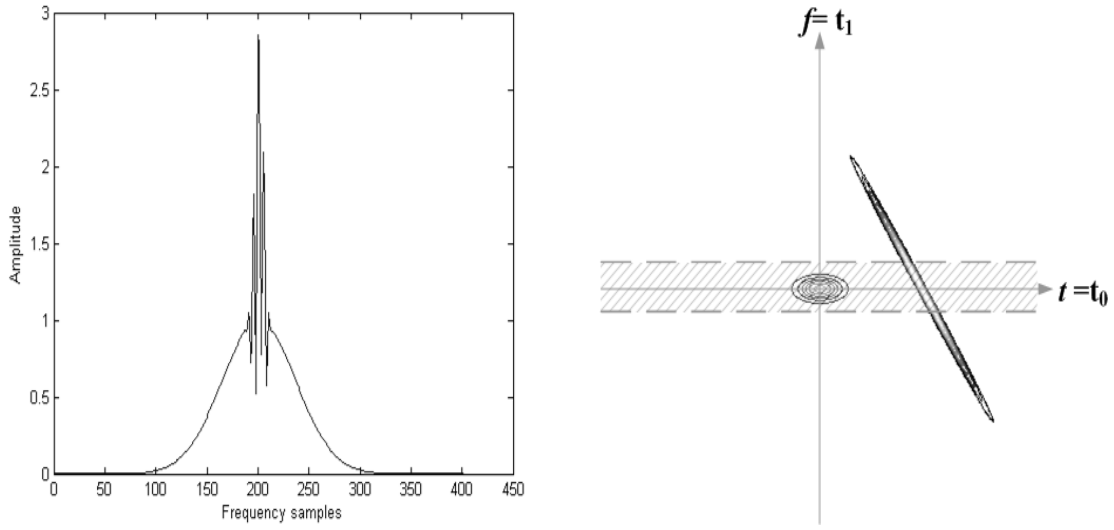

(a) (b)

Figure 2-7 *(a) Fourier transform of the corrupted signal, (b) Low-pass filtering effect in the Fourier domain t_1 shown in the original T-F plane.*

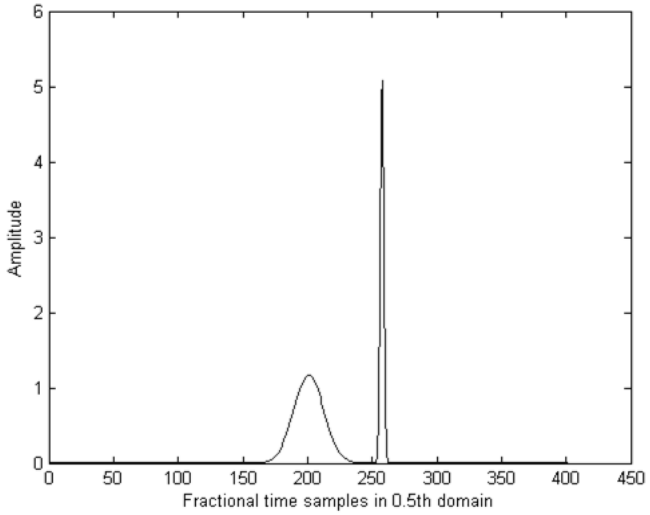

Figure 2-8:

The chirp component together with Gaussian signal in the $t_{0.5}$ domain.

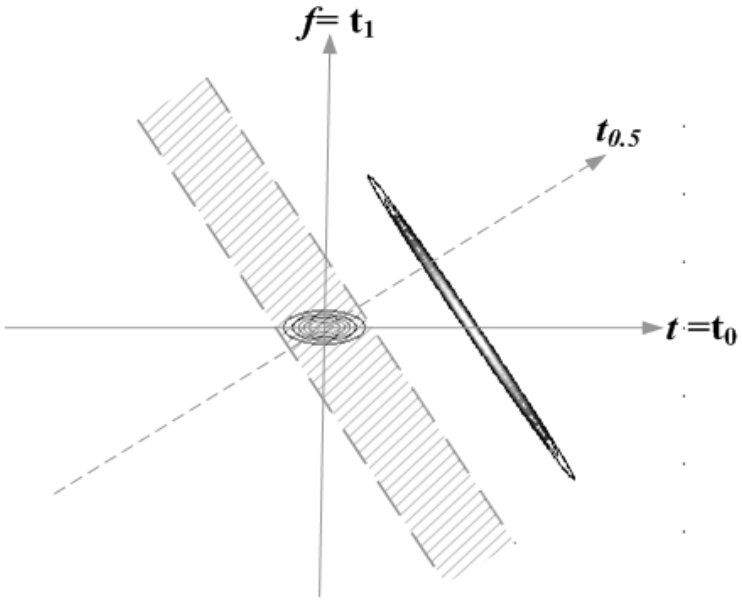

Figure 2-9:

Equivalent low-pass filtering effect in the fractional Fourier domain $t_{0.5}$ shown in the original T-F plane.

Example 2.2

Figure 2-10d shows two Gaussian atoms centered around the origin in the T-F plane, being corrupted by a quadratic chirp. In this example, the method of elimination is exactly the same as before with the exception that the process of filtering is repeated consecutively in three different fractional Fourier domains (t_{a1}, t_{a2}, and t_{a3}) as indicated in Figure 2-11.

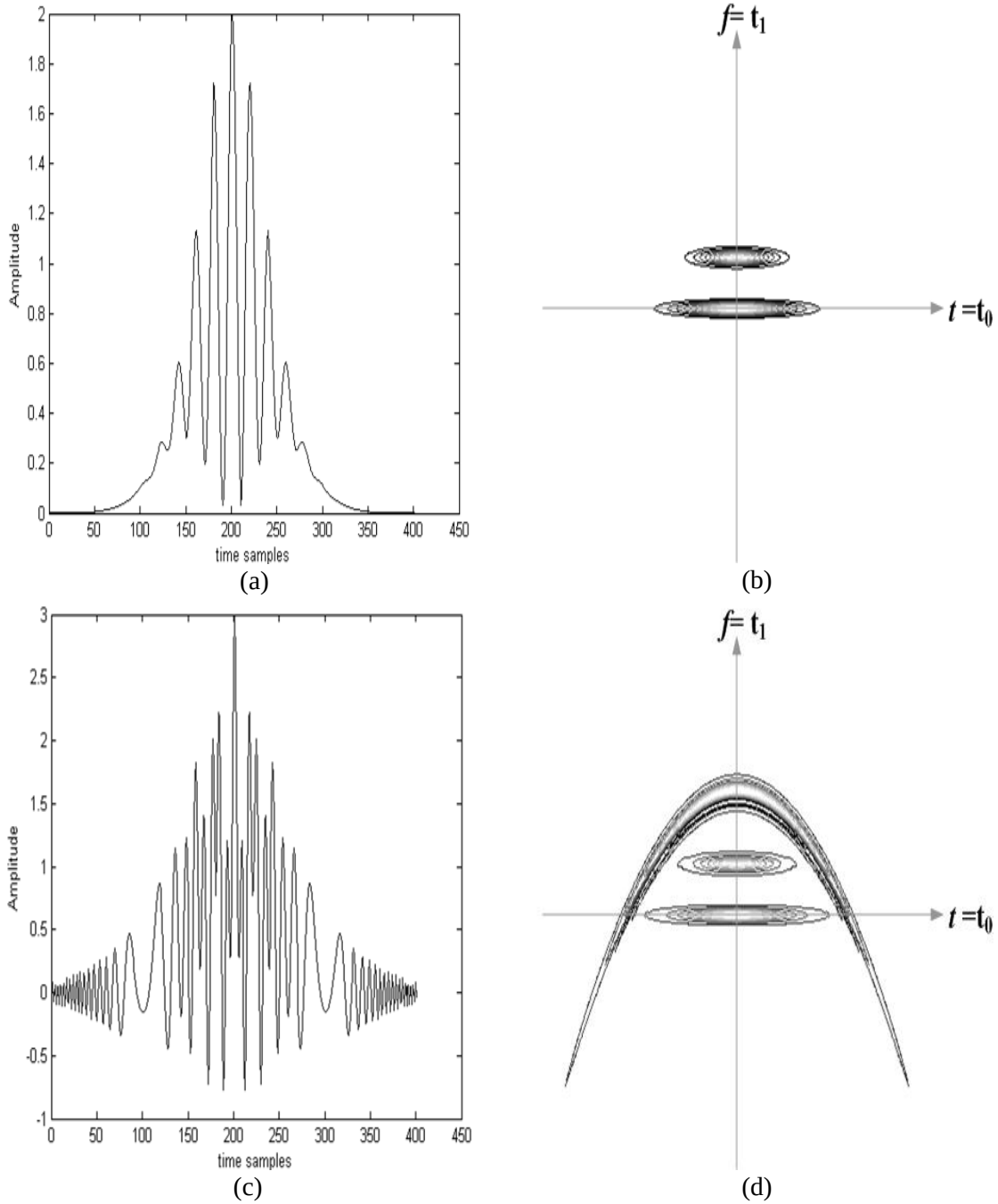

Figure 2-10 *(a) The ideal signal and (b) Time-Frequency distribution of the ideal signal. (c) The corrupted signal and (d) Time-Frequency distribution of the corrupted signal.*

This is due to the large overlap region between the desired components (Gaussian atoms) and unwanted signal. This type of filtering is also referred to as a three-stage FrFT denoising process. Based on Figure 2-11, it is clear that by applying such a denoising scheme on the corrupted signal, the unwanted part of the signal can be completely removed while retaining the desired part (Gaussian atoms). Thus, it can be said that, repeated filtering in consecutive rotated domains may be more robust and effective in removing overlapping interference terms (such as noise) as compared to filtering in a single rotated domain.

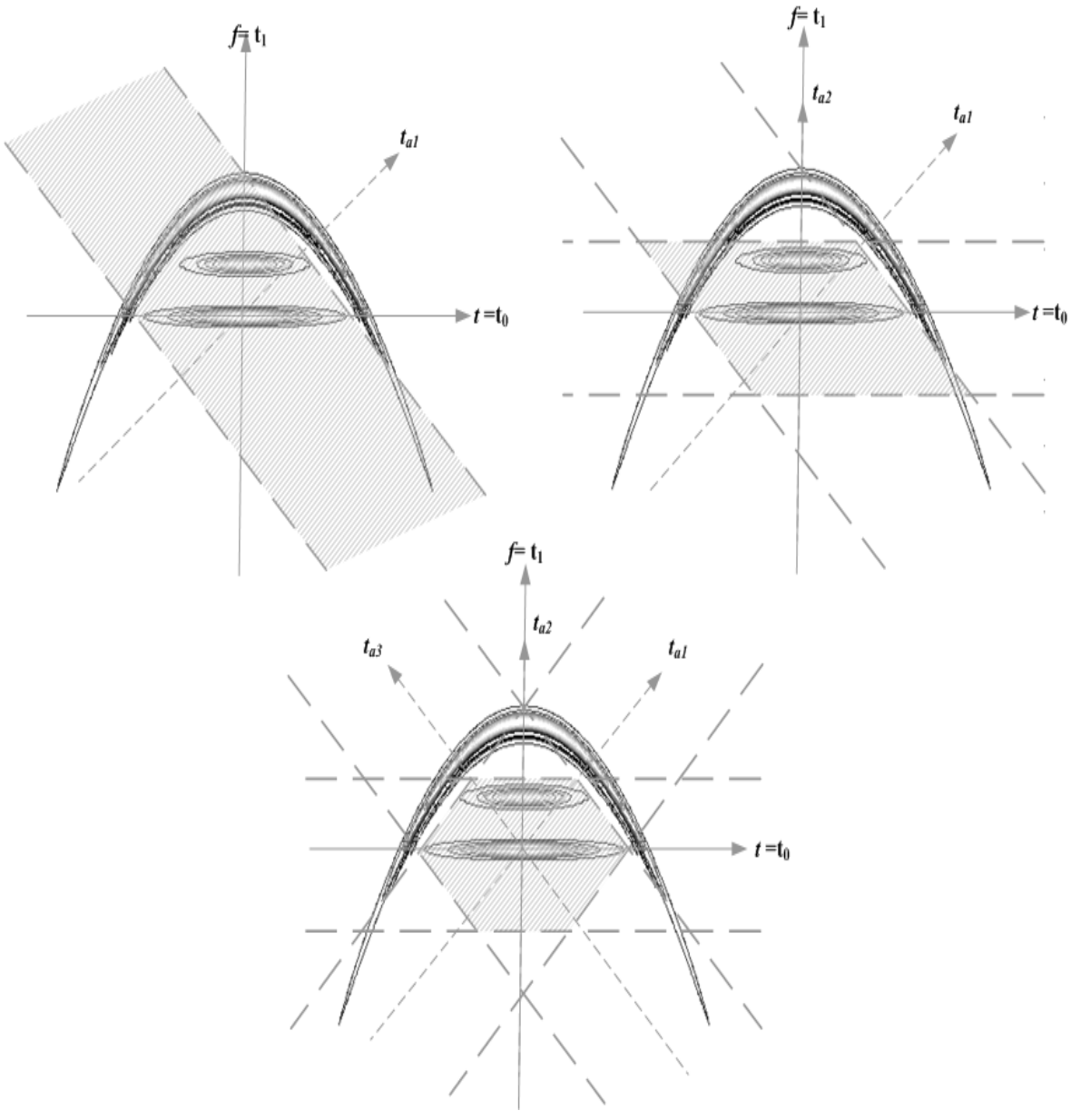

Figure 2-11 *The 3-stage consecutive FrFT filtering process.*

2.3 The Discrete Fractional Fourier Transform

A great deal of effort has gone into defining a discrete FrFT which has resulted in a variety of formulations [4], [16], [17]-[20]. Although each of these approaches comes with its relative advantages, a major drawback in most of them is that they may not satisfy certain key properties expected from a discrete FrFT F_a such as:

i. Unitarity, i.e. ${F_a}^H = {F_a}^{-1}$, where ${F_a}^H$ is the conjugate transposed matrix F_a;

ii. Index additivity;

iii. Reduction to the Discrete Fourier transform (DFT) when $a = 1$;

iv. Replication of the behaviour of the continuous FrFT.

For instance, both definitions in [4] and [19] do not satisfy properties (i) and (ii), while the approach described in [20] does not conform to property (iii). As it is apparent in the discussion provided in Section 2.1, the problem of developing a discrete form of the FrFT is a difficult task. To our knowledge thus far, only the work in [16] best meets the requirements (i)-(iv) listed above. Following the work in [17] and [18], the authors in [16] have provided an analytical development of a discrete FrFT, and generated the corresponding kernel as the discrete analogue of (2.8). First, a discrete version of the defining eigen-equation of the Hermite-Gaussian functions was constructed in a way proportional to the continuous-time case. It was then shown that the above equation shared a common set of eigenvectors with the DFT matrix, and it was further proved that this was a unique and orthogonal set. Subsequently, the related eigenvectors were sorted such that a one-to-one correspondence to the continuous Hermite-Gaussian functions was established. Thus, the discrete FrFT matrix could finally be defined as [16]:

$$F_a[m,n] = \sum_{k=0,k\neq(N-1+(N)_2)}^{N} u_k[m] e^{-j\frac{\pi}{2}ka} u_k[n] \tag{2.21}$$

where $u_k[n]$ denotes the k^{th} discrete Hermite–Gaussian function, and $(N)_2 \equiv N \bmod 2$, with N being equal to the number of signal samples.

2.4 Summary

Thus far in this chapter, the well-known Fractional Fourier transform has been explored and additionally, by using its defining eigenfunctions together with its fundamental relationship with the Wigner distribution, presented the interpretation of this transform as a rotation operator in the T-F plane. It has further been shown that by utilizing this unique property, a more advantageous and flexible filtering scheme could be defined. In the following chapters, the above developed ideas will be employed to deal with some significant and non-trivial signal processing problems.

Appendix

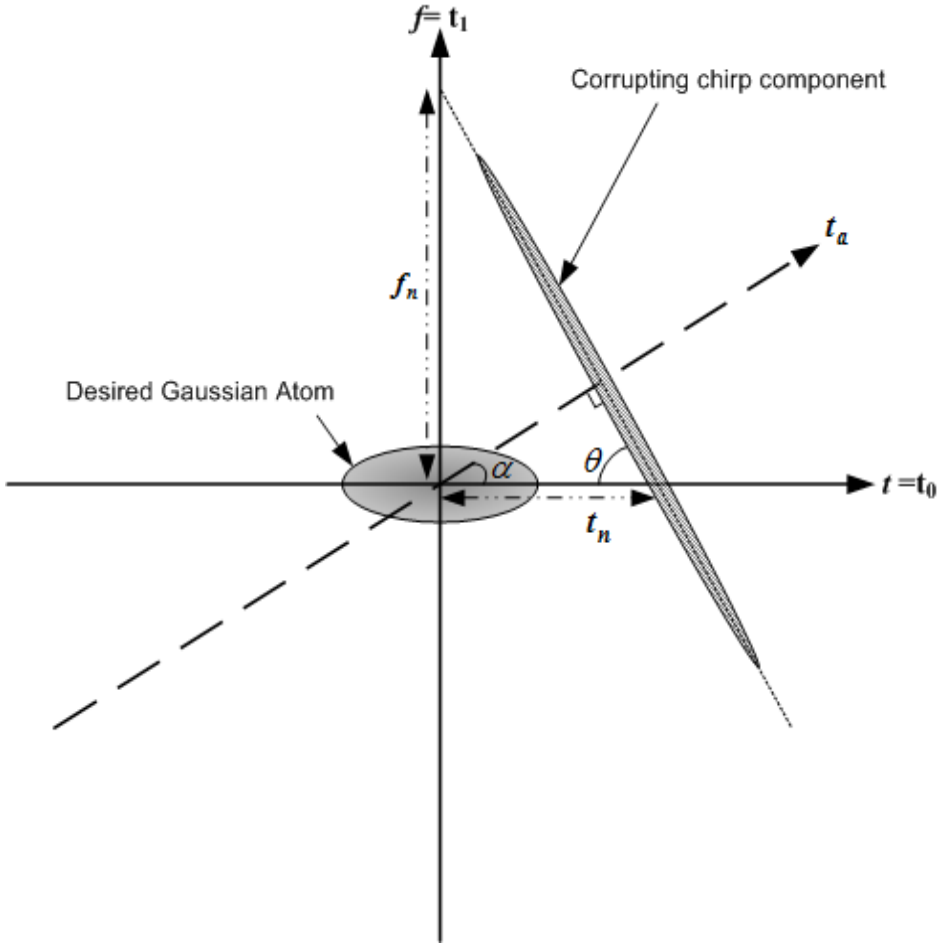

Figure 2-12 *Determining the most suitable a (geometrically) for Example 2.1*

From Example 2.1 and the Figure 2-12, if the linear chirp is given by $e^{j\phi}$, where $\phi = 2\pi(-0.5(t-4)^2)$, then its instantaneous frequency can be expressed as,

$$\frac{d\phi}{dt} = (-t+4)$$

$\frac{d\phi}{dt}$ intersects the time and frequency axes at: t = 4s and f = 4Hz. In the discrete grid, one has: t_n = 4/Ts = 80 and f_n = 4/((Fs)/N) = 80, where Ts = 1/Fs, Fs=20, and N = 401, then the following can be obtained, $\theta = \tan^{-1}\left(\frac{f_n}{t_n}\right) = 45^{\circ}$

$$\alpha = (90-\theta) = 45^{\circ}$$

Therefore, the most suitable fractional domain t_a, can then be determined to be equal to $\alpha/90$, which is 0.5.

References

[1] S. R. Subramaniam, B. W.-K. Ling, and A. Georgakis, “Filtering in rotated time-frequency domains with unknown noise statistics”, IEEE Trans. Signal Process., vol. 60, no. 1, pp. 489 – 493, January 2012.

[2] A. Georgakis, and S.R. Subramaniam, “Estimation of the second derivative of kinematic impact signals using fractional Fourier filtering”, IEEE Trans. Biomed. Eng., vol. 56, pp. 996-1004, 2009.

[3] M. A. Kutay. Generalized filtering configurations with applications in digital and optical signal and image processing. Ph.D. Thesis, Bilkent University, Ankara, 1999.

[4] H. M. Ozaktas, O. Arikan, M. A. Kutay, and G. Bozdagi, “Digital computation of the fractional Fourier transform,” IEEE Trans. Sig. Proc., vol. 44, pp. 2141–2150, 1996.

[5] T. Erseghe, P. Kraniauskas, and G. Cariolaro, “Unified fractional Fourier transform and sampling theorem,” IEEE Transactions on Signal Processing, vol. 47, no. 12, pp. 3419-3423, Dec, 1999.

[6] G. B. Folland, Harmonic Analysis in Phase Space. Princeton University Press, 1989.

[7] B. A. Weisburn and T. W. Parks, “Design of Time Frequency Strip Filters,” in 29th Annual Asilomar Conf. on Signals, Systems and Computers, Oct. 29 1995.

[8] B. A. Weisburn and R.G. Shenoy, "Time-frequency strip filters," in IEEE ICASSP Proceedings, vol.3, no., pp.1411-1414, 7-10 May 1996.

[9] L. B. Almeida, “The Fractional Fourier-Transform and Time-Frequency Representations,” IEEE Transactions on Signal Processing, vol. 42, no. 11, pp. 3084-3091, Nov, 1994.

[10] D. Mustard, “The fractional Fourier transform and the Wigner distribution,” J. Austral. Math. Soc. B—Appl. Math., vol. 38, pp. 209–219, 1996.

[11] M. A. Kutay, H. M. Ozaktas, and O. Arikan, “Optimal filtering in fractional Fourier domains,” IEEE Transactions on Signal Processing, vol. 45, no. 5, pp. 1129-1143, May, 1997.

[12] H. M. Ozaktas, B. Barshan, and D. Mendlovic, “Convolution, Filtering, And Multiplexing In Fractional Fourier Domains And Their Relation To Chirp And Wavelet Transforms,” Journal of the Optical Society of America A-Optics Image Science and Vision, vol. 11, no. 2, pp. 547-559, Feb, 1994.

[13] S. C. Pei, and J.-J. Ding, “Fractional Fourier Transform, Wigner Distribution, and Filter Design for Stationary and Nonstationary Random Processes,” IEEE Transactions on Signal Processing, vol. 58, no. 8, pp. 4079-4092, Aug, 2010.

[14]M. F. Erden, M. A. Kutay, and H. M. Ozaktas, “Repeated filtering in consecutive fractional Fourier domains and its application to signal restoration,” IEEE Transactions on Signal Processing, vol. 47, no. 5, pp. 1458-1462, May, 1999.

[15]H. M. Ozaktas, “Repeated fractional Fourier domain filtering is equivalent to repeated time and frequency domain filtering,” Sig. Proc. , 54:81-84, 1996.

[16]Ç. Candan, M.A. Kutay, H.M. Ozaktas, The discrete fractional Fourier transform, IEEE Trans. Signal Process. 48 (2000) 1329–1337.

[17]S. C. Pei and M. H. Yeh, “Improved discrete fractional Fourier transform,” Opt. Lett., vol. 22, pp. 1047–1049, 1997.

[18]S. C. Pei, C. C. Tseng, M. H. Yeh, and J. J. Shyu, “Discrete fractional Hartley and Fourier transforms,” IEEE Trans. Circuits Syst. II, vol. 45, pp. 665–675, 1998.

[19]O. Arıkan, M. A. Kutay, H. M. Ozaktas, and Ö. K. Akdemir, “Discrete fractional Fourier transformation,” Proc. IEEE SP Symp. Time-Freq. Anal., vol. 4, pp. 205–207, 1996.

[20]N. M. Atakishiyev and K. B.Wolf, “Fractional Fourier-Kravchuk transform,”J. Opt. Soc. Amer. A., vol. 14, pp. 1467–1477, 1997.

[21]H.M. Ozaktas, M.A. Kutay, C. Candan, "Chapter 14: Fractional Fourier Transform" in Transforms and Applications Handbook 3rd Edition, Edited by: Alexander D. Poularikas, 2010.

[22]A. Bultheel and H. Martinez-Sulbaran, "Recent developments in the theory of the fractional Fourier and linear canonical transforms," Bull. Belg. Math. Soc. Simon Stevin Volume 13, Number 5 (2007), 971-1005.

Chapter 3

Fractional Fourier-Based Low-Pass Filtering

In this chapter the application of fractional Fourier-based filtering is detailed. In particular, a specific type of low-pass filtering system operating in distinctive fractional Fourier transform domains is, applied in real-world problems. The work described in this chapter is a continuation of earlier contributions on this topic [1, 2], and has been reported in, [3], [4], and [5].

Introduction

In Chapter 2, it was stated that working in rotated T-F domains may be advantageous for filtering non-stationary signals. In this chapter, this idea is revisited to develop unique filtering configurations based on the FrFT for the denoising of non-stationary signals occurring in the area of biomechanics and ultrasound elastography. These selected case studies will help us illustrate both the need for – and the advantages of employing –FrFT based filtering schemes.

The first application is concerned with the accurate estimation of the second derivative of noisy kinematic signals involving single impact events [1, 2, and 3]. The proposed algorithm operates in predetermined consecutive FrFT domains with the aim of achieving a low-pass filter with time-varying cut-off threshold, which can successfully accommodate the impact-induced changes in the frequency content of the signals. Results obtained from this experiment are summarized in Section 3.1.1.2.

It is then shown that it is straightforward to extend the above system to deal with kinematic signals with multiple impacts [1, 4]. This time, the proposed method is designed such that its time-varying cutoff threshold has the ability to accommodate the frequency expansions caused by multiple distinct non-stationarities present in the signal. The results obtained from this experiment are reviewed in Section 3.1.1.3.

The second application deals with a problem appearing in the area of ultrasound elastography [5]. In ultrasound elastography, tissue axial strains are obtained through the differentiation of axial displacements. However, application of the gradient operator greatly amplifies the noise present in the displacement rendering unreadable axial strains. Therefore it is imperative to effectively remove the noisy components, prior to differentiation. Since the axial strains also contain distinct non-stationarities, a comparable filter circuit as described above can be specified to achieve such a task. The results from this experiment are studied in Section 3.1.2.2.

3.1 Case Studies

3.1.1 Filtering of Kinematic Impact Signals

Biomechanics has recently been considered to be a fundamental tool for the analysis of human motion in the areas of Health, Exercise and Sport Industry. Information extracted from the study of human motion is advantageous to surgeons, clinicians, physiotherapists [25-27], trainers, athletes [28] and even athletic accessory companies [29]. In this way, patients with movement problems can be relieved or even healed, athletes can avoid injuries and make better use of their training time and competitive athletes may even be able to improve their performance. Furthermore, better quality products (e.g. walking and running shoes, exercise equipment and etc.) can be manufactured to be beneficial not only in the sports world but also in improving the comfort of everyday life.

In order for human motion to be quantitatively studied, the motion must first be captured. This can be accomplished by using various optical or magnetic devices, which provides coordinates of special indicators (markers) affixed to the body within a calibrated three-dimensional (3-D) space. The acquired displacement data forms the so-called kinematic signals. Subsequently, the kinematic data can then be processed to compute linear or angular higher derivatives such as velocity and acceleration. It may also be possible to directly measure the acceleration of a considered set of skeletal points by affixing accelerometers on them. Other important information, such as ground-reaction forces can be additionally collected from devices known as force plates which register the magnitude of the total force exerted on the foot during ground contact. These signals (i.e. displacement, acceleration and ground-reaction force) are invaluable for the quantitative study of human motion and can lead to an in-depth knowledge of the underlying phenomena.

Particularly, the acceleration data can either be used in combination with the ground reaction forces to estimate joint dynamics, or with further processing using optimization procedures to estimate muscular forces responsible for movement in humans [30]. In general, the acceleration data is obtained from a simple differentiation process of the acquired displacement signal. However, the processing of biomechanical data is susceptible to errors caused by a number of factors [6]. A common problem is that the derivatives computed from experimentally acquired displacement signals are in most cases, inaccurate. This is because differentiation is a process which can severely obscure the resulting derivatives by magnifying the high frequency components – which are mainly due to noise. It is therefore mandatory that appropriate denoising of the signal must be performed prior to differentiation.

Several conventional schemes for kinematic data filtering have been proposed in the past, including Butterworth digital low-pass filtering and splines fitting [7]. These methods

implicitly presuppose that the signal at hand is stationary, which, however, is a non-realistic assumption [8]. In fact, the frequency content of biomechanical signals may undergo considerable changes especially when activities that involve impacts are considered; there is an abrupt transition from the low-frequency part of the movement (aerial or swing phase) into higher frequencies (impact phase) and vice versa. Conventional methods are unable to cater for these changes so they either under-smooth or over-smooth the displacement data [7]-[14].

Recently, time-frequency/scale de-noising techniques have been introduced to deal with the problem of filtering impact signals. These have been based either on wavelet transforms [10], [11], or the Wigner distribution (WD) [12], [13]. The rationale behind the time-frequency/scale approaches is that for effective filtering of non-stationary signals different cut-off thresholds must be applied at different times [14]. Indeed, published results have demonstrated that these methods can achieve good estimation of the second derivative of noisy signals. However, current wavelet de-noising algorithms exhibit certain limitations [11]. Firstly, the quality of the results depends on the choice of the particular wavelet employed. Secondly, the discontinuities in the transform domain caused by the wavelet coefficients' thresholding process produces pseudo-Gibbs artifacts which appear particularly amplified in the calculated derivatives. On the other hand, the WD-based approach yields a better overall denoising performance but it is highly non-linear, restricting its applicability in real-time scenarios.

3.1.1.1 Methodology

The work presented here, draws upon the successful idea of using the time-frequency (T-F) plane to design a suitable time-dependent cut-off threshold for the low-pass filtering of the aforementioned impact data. Thus to realize such a filter, it follows from Chapter 2, to implement it by operating in consecutive fractional Fourier domains. The main differences

between the proposed approach and previous work on FrFT filtering - can be crystallized as follows [2]:

- No assumptions are made about the noise statistics, and no a-priori knowledge of the signal is available,
- The proposed algorithm operates successively in two specific fractional Fourier domains,
- The filtering procedure is carried out by way of convolution with known, well-behaved filters,
- The implementation of the algorithm is informed by the prior design of the time-variant cut-off threshold in the time-frequency plane,
- The filter is applied to experimentally acquired signals which exhibit considerable changes of their frequency content at distinct points in time.
- The signal is processed in consecutive fractional Fourier domains, rendering a faster, linear algorithm with physically meaningful parameters.

As it was pointed out earlier, the frequency content of kinematic signals may undergo considerable changes upon impact. This is attributed to the fact that higher frequencies emerge due to the resulted sudden changes in the time waveform. Moreover, these nonstationarities only last for several milliseconds (impact duration) and occur at distinct points in time that correspond to collisions of the moving body with other objects or rigid surfaces. The range of impact-induced frequencies is proportional to the severity of the collision, which is also reflected in the magnitude of the acceleration profile of the movement. It is clear that these frequencies are an essential part of the signal and should be preserved. Therefore, the designed filtering boundary has to extend towards higher frequencies in the impact neighborhood while maintaining a narrow profile at all other times (e.g. [12]). A simple realization of such a boundary can be seen in Figure 3-2. It can easily be observed that as opposed to conventional filtering where a single cutoff

frequency is applied to the whole signal (Figure 3-1); Figure 3-2 clearly provides a more appropriate threshold.

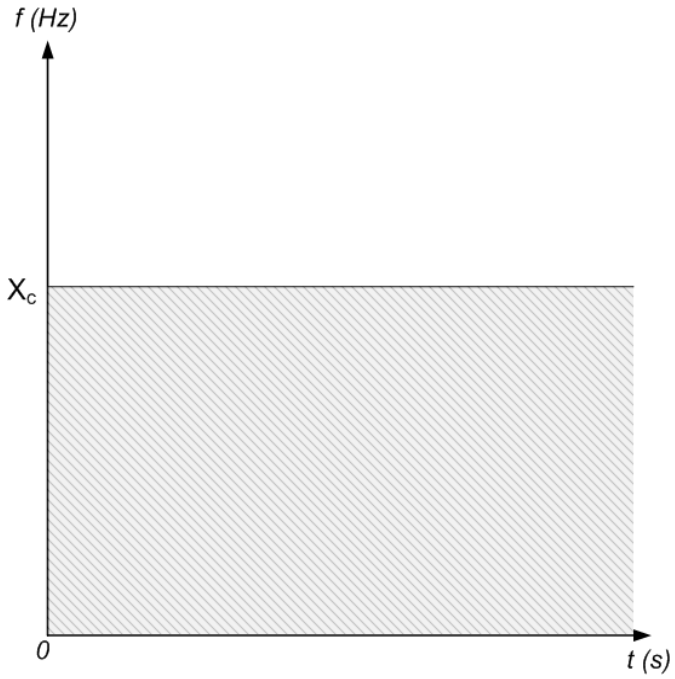

Figure 3-1:

The global effect of the cutoff threshold corresponding to conventional filtering in the frequency domain.

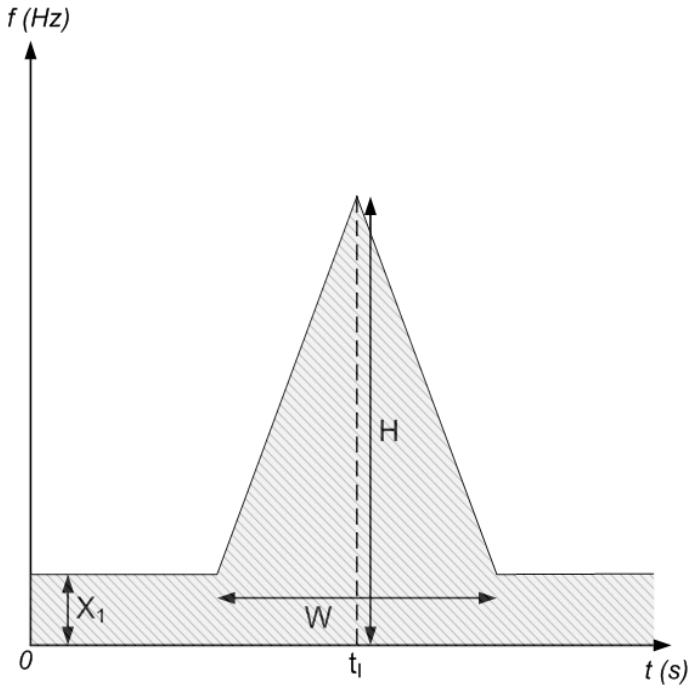

Figure 3-2:

The designed time-varying cutoff frequency threshold. The frequency response of the filter equals to one inside the areas shaded in gray and zero otherwise.

The time-varying filtering boundary presented in Figure 3-2 is controlled by the four parameters shown in this figure, which should be adjusted accordingly in order to achieve

a good filtering performance. The selection of suitable values for these parameters is based on simple, empirical algorithms that can be described as follows [2];

The cutoff threshold X_1 corresponds to the low-frequency content of the aerial phases of the signal and can thus be well fixed at a low frequency value. Point t_I around which the triangle is centered, is chosen as the time of maximum acceleration (absolute values). This can easily be identified from the second derivative of the displacement signal, pre-filtered with cutoff at $2X_1$.

The width W of the triangle relates to the duration of the impact. To estimate this, the signal is first low-pass filtered with the cutoff frequency at X_1, and the second derivative of the result is then calculated. Focusing on the neighborhood of the impact, one should notice that the calculated acceleration increases/decreases monotonically around its peak value. Then W can be considered to be equal to twice the distance between point t_I and the first point to its left where the slope of the acceleration changes sign.

The height H of the triangle corresponds to the impact-induced expansion of the frequency content and may be determined by iterative calculations of the energy of the residual signal for different cutoff thresholds. In particular, the impact neighborhood would first have to be extracted (using the values of t_I and W) and afterward low-pass filtered at gradually increasing cutoff values. The residual, i.e. the error between the original segment and its filtered version can then be obtained. As before, based on some experimentation, the energy of this residual was found to be a monotonically decreasing function of the cutoff threshold. Thus, the frequency at which the rate of change of the residual energy falls below a predetermined level is subsequently chosen as the value for H. To visualize the empirical processes described above, illustrations have been provided in the appendix section at the end of this chapter.

To simplify the implementation of the proposed scheme, the signal is first positioned so that the identified time of impact t_I coincides with $t=0$. The triangular T-F filtering

boundary is accordingly centered at the origin in order to preserve the impact-induced frequencies. Figure 3-3a illustrates the two fractional Fourier domains determined by the triangular boundary. These are the domains t_{a_1} and t_{a_2}, which are perpendicular to the right and left sides of the triangle, respectively. The intersections of the sides of the triangle with the specified axes t_{a_1} and t_{a_2} provide the low-pass cutoff values for each fractional domain. Based on the geometry of the given isosceles triangle, one can easily determine the angle $\phi_1=a_1\pi/2$ as well as the distance of the right side from the origin, i.e. the cutoff value X_{a_1}, as follows (Figure 3-3b),

$$\phi_1 = \arctan(\frac{w}{2h}) \text{ and } X_{a_1} = h\sin\phi_1 \tag{3.1}$$

where $w=W/T_s$ and $h=H/F_s$, with T_s the sampling period and F_s the frequency step. At this point, one can either design an appropriate multiplicative function $g_{a_1}(t_{a_1})$ and carry out the masking operation in (2.18), or equivalently, transform the signal into the $(a_1\text{-}1)^{\text{th}}$ domain and convolve with $g_{a_1-1}(t_{a_1-1})$, as described in (2.19). Note that the $(a_1\text{-}1)^{\text{th}}$ domain is located at angle $-\theta_1$ as shown in Figure 3-3b, with $\theta_1=90^0-\phi_1$.

Next, the angle ϕ_2 of the second fractional domain t_{a_2} can be obtained (Figure 3-3c). Clearly, $\phi_2 = 180°-\phi_1$ and $X_{a_1} = X_{a_2}$. The signal from the $(a_1\text{-}1)^{\text{th}}$ domain is now transformed into the $(a_2 - 1)^{th}$ domain via a second FrFT of order $2\theta_2/\pi$, where $\theta_2 = 180^0 - 2\phi_1$. The result can then be convolved with a suitable low-pass filter, and transformed back into the time domain through a final FrFT of order $-2\theta_3/\pi$, where $\theta_3=90^0-\phi_1$. The overall fractional filtering process can be summarized as follows,

$$\widehat{s_{HF}(t)} = F^{\frac{-2\theta_3}{\pi}}\left[g_{a_2-1}(t_{a_2-1}) * F^{\frac{2\theta_2}{\pi}}\left[g_{a_1-1}(t_{a_1-1}) * F^{\frac{-2\theta_1}{\pi}}[s_{HF}(t)]\right]\right] \tag{3.2}$$

where $s_{HF}(t)$ is the original and $\widehat{s_{HF}(t)}$ the resulted high-frequency component of the signal.

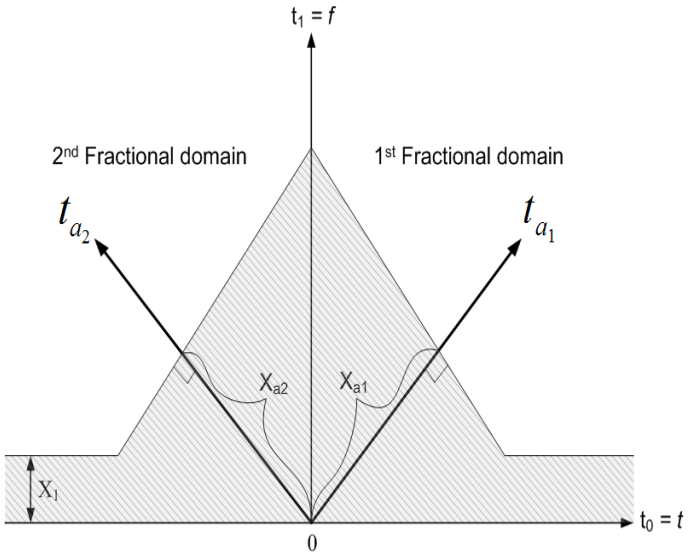

Figure 3-3a:

The overall time-varying pass-band, the two fractional domains considered and the corresponding cutoff thresholds (the reflection of the pass-band in negative frequencies is omitted).

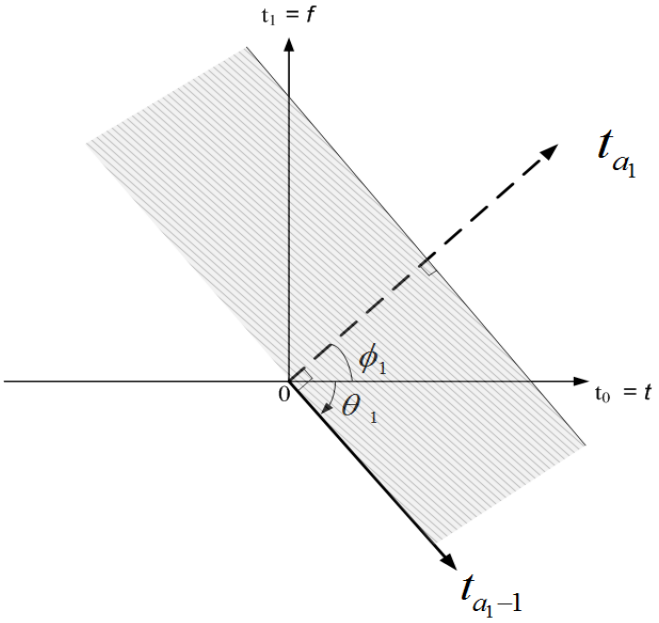

Figure 3-3b:

Visualization of the first stage of the fractional Fourier transform filter in the time-frequency plane (only positive fractional frequencies are shown).

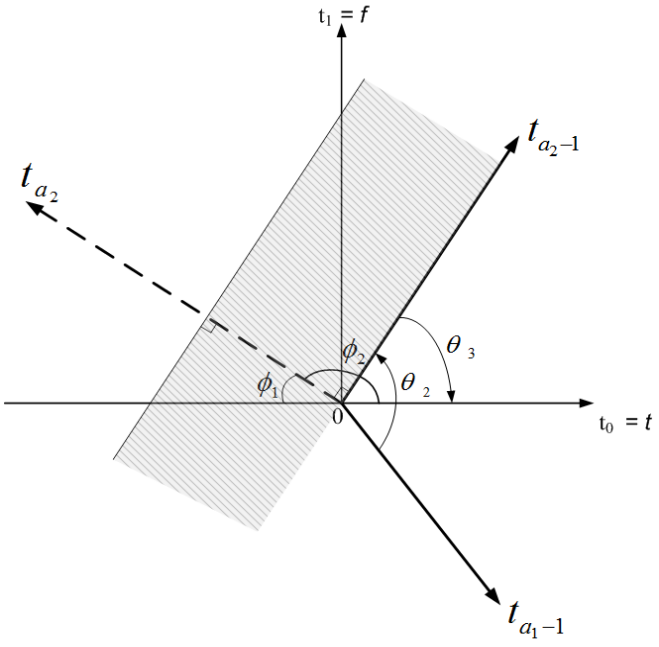

Figure 3-3c:

Visualization of the second stage of the fractional Fourier transform filter in the time-frequency plane (only positive fractional frequencies are shown).

The block diagram of the proposed filter is presented in Figure 3-4 [1, 2]. This diagram indicates that the proposed method belongs to the class of generalized filtering configurations called filter circuits in [15]. Determining the structure of such circuits in general, is a difficult problem that has not been explored in the literature. The proposed method offers a way to overcome this difficulty by using the designed time-varying cutoff frequency threshold to guide the configuration of a suitable filter for the signal at hand.

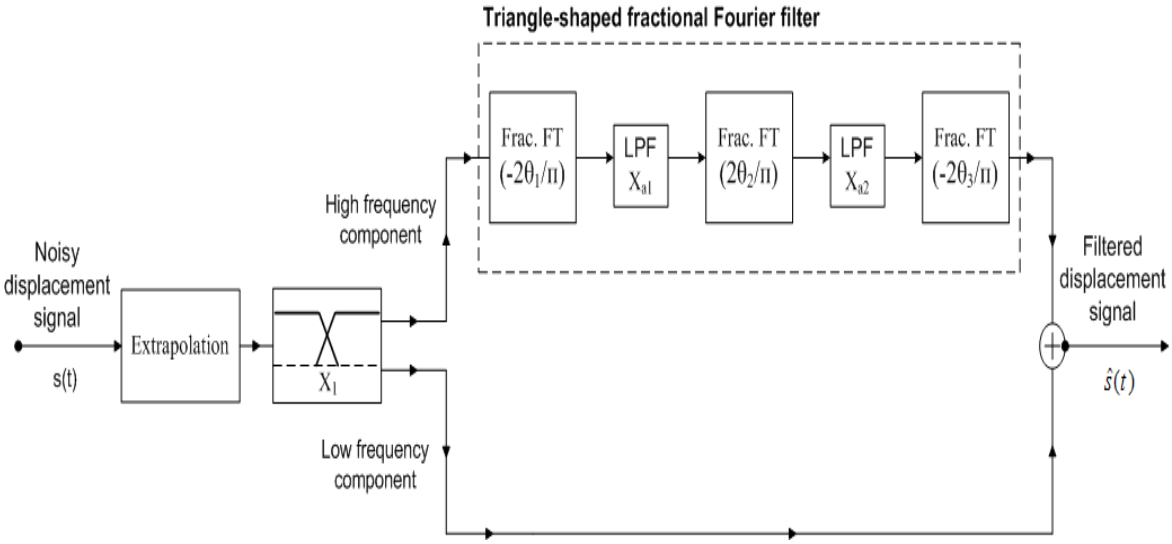

Figure 3-4 *Block diagram of the proposed filter circuit.*

3.1.1.2 Experimental Results

To gauge its performance, the proposed method is then applied to a set of thirteen test signals (S_1- S_{13}) obtained from three different impact experiments. The acquisition of these signals is accurately described in Section IV-A in [2]. Two automatic conventional and two semi-automatic advanced techniques were also considered.

The proposed algorithm was implemented according to the process described alongside Figure 3-3. Zero-phase (forward and reverse pass) Butterworth filters were employed for the high/low frequency separation and the two successive convolutions of (3.2). The cutoff threshold X_1 was fixed at 12 Hz for all signals. Parameters W and t_I were estimated in a

fully automatic manner as described in conjunction with Figure 3-2. To determine suitable values for the height *H* of the triangle, the test signals (described in Section IV-A in [2]) were first separated into high-impact and low-impact ones. For the high-impact signals the threshold for the rate of change of the residual energy was set to 0.01, whereas for the low-impact ones the corresponding threshold was fixed at 0.3. The selection of these thresholds reflects the proportional relationship between impact severity and the extent of impact-induced frequencies. As an indication of the robustness of this specific algorithm, it was observed that the nine high-impact signals originated from different experiments (i.e. different types of impact and levels of noise), as was the case for the four low-impact signals [2].

As previously discussed, two established automatic noise removal techniques were employed for comparison with the proposed algorithm. The first one was the generalized cross validation spline-fitting (GCVSPL) method [8], applied with fifth-order splines in this study. The second technique was the power spectrum assessment method [9], which is an implementation of the linear-phase autoregressive model-based derivative assessment (LAMBDA) algorithm [16].

The wavelet denoising approach was also used in the experiments. This approach was based on Donoho's three-step denoising technique [17]. The orthogonal Daubechies and the biorthogonal interpolating spline wavelet families were also considered here in line with previous studies [10], [11]. An extensive search was performed for each signal in order to identify which members of the above wavelet families should be employed. The number of decomposition levels, as well as the threshold selection and rescaling rules were also manually determined for each signal. Soft thresholding was used for all signals. Several acceleration profiles of the denoised signals yielded severe end-point problems, so the first and last fifty points were excluded from the calculation of their RMS errors. The WD-based TF filter was also employed for the comparisons, implemented as in [2].

Two different error measures were used to quantify the efficiency of the proposed method and compare it with alternative approaches. The RMS error, defined as

$$RMS = \sqrt{\frac{1}{N}\sum_{n=0}^{N-1}\left(\alpha[n] - \widehat{\alpha[n]}\right)^2} \tag{3.3}$$

is a measure of the overall quality of the filtering process. In (3.3), $\alpha[n]$ is the reference acceleration (as measured by accelerometers) and $\widehat{\alpha[n]}$ is the second derivative of the filtered displacement data, while N is the number of time samples of the signal. The peak error,

$$peak\ error = \frac{|\widehat{\alpha(n_I)}| - |\alpha(n_I)|}{|\alpha(n_I)|} \tag{3.4}$$

where n_I is the sample closest to the acceleration peak value at impact, provides the accuracy in which the impact acceleration is estimated. A positive value of (3.4) is an overestimation of the acceleration peak, while a negative result corresponds to underestimation. It should be noted that the reference acceleration $\alpha[n]$ is only an approximation to the ideal result since it is itself susceptible to a number of errors, such as noise imposed by the measurement devices, and post-impact vibrations due to the insufficient rigidity with which accelerometers are usually attached to the body.

Since the signal S_1 described in [2] is a popular test signal in the literature, the calculated acceleration of this signal obtained after filtering with the different algorithms described above is depicted in Figure 3-5. The motion in S_1 involved a horizontally rotating pendulum that impacts with a non-rigid barrier [14]. The angular coordinate was recorded with a motion capture system at 512Hz. At the same sampling rate, the angular acceleration was directly measured by a system of accelerometers. This measured acceleration (i.e. reference acceleration) is then directly contrasted to the obtained results. The individual results for all signals with respect to the percent peak error and the overall RMS error are presented in Tables I and II, respectively in [2].

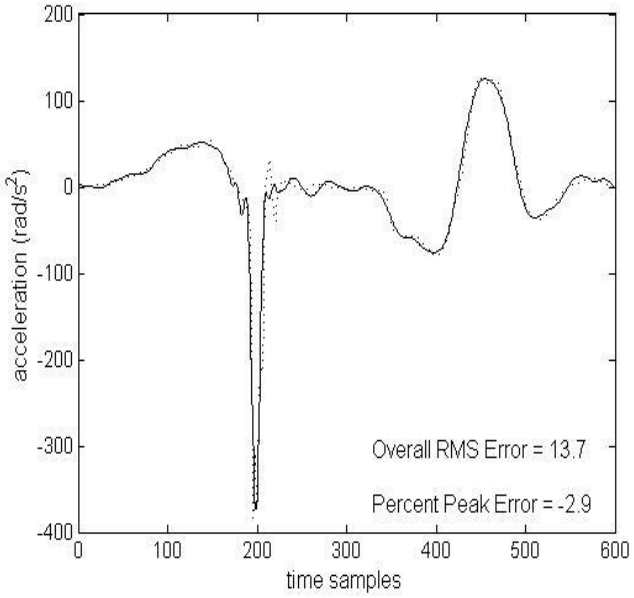

Figure 3-5a:

Calculated acceleration for signal S_1 (solid lines) after applying the proposed repeated FrFT filter contrasted against the reference acceleration (dotted lines)

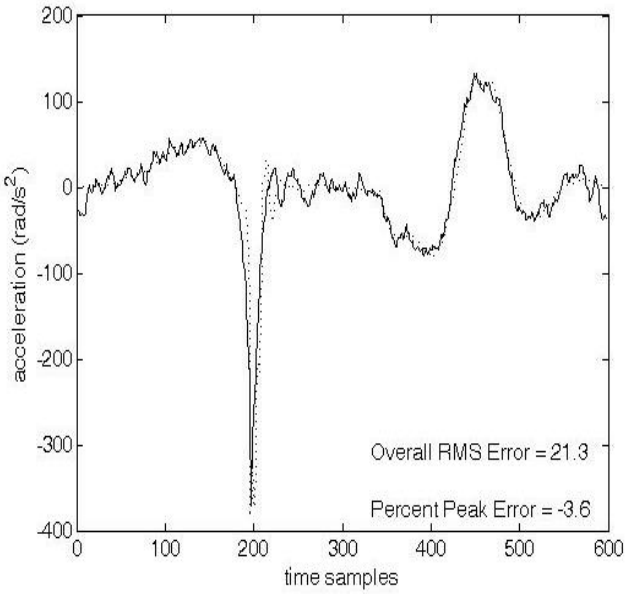

Figure 3-5b:

Calculated acceleration for signal S_1 (solid lines) after applying time-frequency filtering in the Wigner distribution

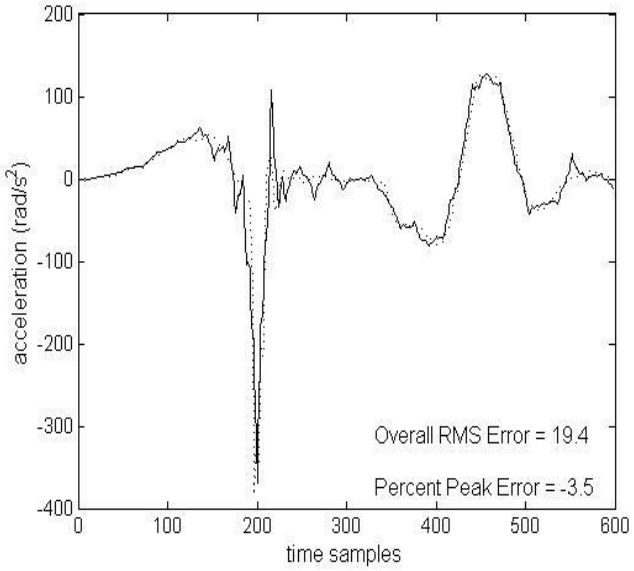

Figure 3-5c:

Calculated acceleration for signal S_1 (solid lines) after applying wavelet denoising using the Daubechies ['db12' in MATLAB's wavelet toolbox, 4 decomposition levels] wavelet.

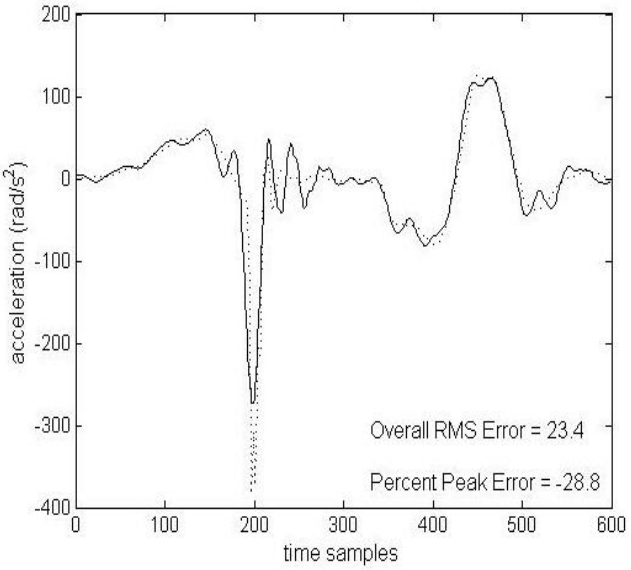

Figure 3-5d:

Calculated acceleration for signal S_1 (solid lines) after applying wavelet denoising using the biorthogonal ['bior6.8' in MATLAB's wavelet toolbox, 8 decomposition levels] interpolating spline wavelet

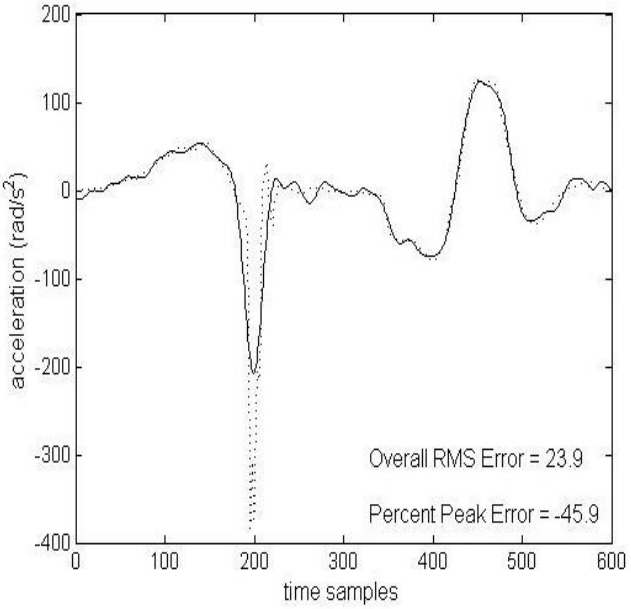

Figure 3-5e:

Calculated acceleration for signal S_1 (solid lines) after applying the LAMBDA method

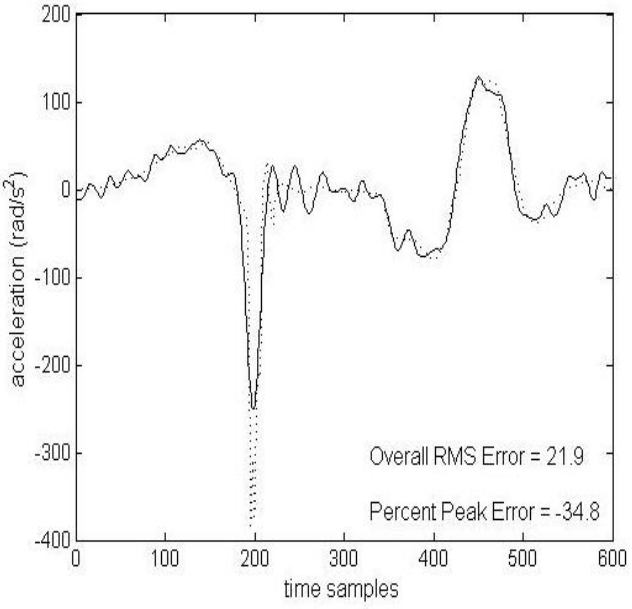

Figure 3-5f:

Calculated acceleration for signal S_1 (solid lines) after smoothing with the GCVSPL method

The average peak error (average absolute value of Eq. (3.4) over all 13 signals) was 5.6% for the introduced FrFT-based filter, 12.7% for the WD-based filtering technique, 7.2% for the wavelet denoising approach based on biorthogonal wavelets, 9.2% for the wavelet denoising approach based on Daubechies wavelets, 18.1% for the LAMBDA method, and 32.9% for the GCVSPL algorithm. The average overall RMS error of the calculated second derivatives was 8.8 for the FrFT-based filter, 8.0 for WD-based filtering, 26.1 for the wavelet denoising approach using biorthogonal wavelets, 28.1 for the wavelet denoising approach using Daubechies wavelets, 9.3 for LAMBDA, and 76.5 for GCVSPL. The results showed that the proposed technique performed well both in terms of acceleration peak estimation and overall noise removal. In addition, it proved to be robust against the different impact severities, noise levels, and types of impact involved in this study. The second best algorithm for acceleration peak estimation was the wavelet denoising approach employing biorthogonal wavelets. However, this method yields rough overall accelerations as it is evident by its high RMS error values. The biorthogonal wavelet in this work captured the maximum accelerations more accurately than the orthogonal one as opposed to the findings of [11], probably due to the different type of signals involved in the two studies. The WD-based filter yielded the lowest RMS errors for most signals. However, the method did not produce good peak acceleration estimates for low-impact signals, in agreement with a previous study [13]. The two automatic conventional methods proved insufficient for most signals, as expected. It should be stressed that approaches based on classical Fourier filtering, even when manually optimized cannot deal with impact displacement signals for the reasons detailed in tandem with Figure 3-1.

Additionally, in [3] the robustness of the overall filtering scheme presented in Figure 3-4, is further examined against noise. Different levels of white Gaussian noise were added to the aforementioned signal S_1. It should be noted that this signal already contained noise

TABLE 3-1

RMS AND PEAK ERRORS OF THE CALCULATED ACCELERATIONS CORRESPONDING TO DIFFERENT LEVELS OF ADDED WHITE NOISE FOR DIFFERENT SNR VALUES DENOISED WITH THE PRESENTED FILTER CIRCUIT (USING BUTTERWORTH FILTERS) AND CONVENTIONAL LOW-PASS FILTERING

Method \ SNR(dB)		100	50	40	30	20	10	0
Proposed	RMSE	13.76	13.76	15.34	15.77	19.06	30.87	41.66
	Peak (%)	2.96	2.96	6.63	11.20	17.60	24.70	35.40
Conventional LP filtering	RMSE	34.70	34.61	34.21	34.92	43.16	64.65	163.13
	Peak (%)	9.91	10.33	15.36	29.15	42.75	47.80	63.68

and no assumptions were made about its statistics. Table 3-1 presents the RMS and absolute peak (AP) errors achieved after denoising with the presented scheme in Figure 3-4. For comparison, results obtained using a conventional Butterworth filter – a popular choice in Biomechanics – are also presented. The cutoff frequency of this filter, as well as its order, was determined so that the combined RMS and AP error was minimized. The listed RMS and AP errors are averages over 100 realizations of the noisy inputs. The low-pass nature of the proposed scheme implies that noise lying below the cutoff frequency X_1 cannot be eliminated. Thus, there is a limit with respect to the minimum level of noise that the method can deal with. For the signal at hand, this was found to be equal to 40 dB SNR. However, the time-varying cutoff threshold can protect the signal much more effectively than any conventional low-pass filter. To focus on the impact phase in particular (which consists of frequencies well above the X_1 value), added noise of colored nature is further experimented with, i.e. noise residing above X_1. The results from this experiment are presented in Table 3-2. As expected, the scheme could now cope with noise down to 0 dB SNR.

Based on the results presented in [2] and [3], it can easily be concluded that the proposed filter circuit can efficiently remove noise from biomechanical impact data while preserving the high-frequency impact components and thus, providing accurate estimates of the acceleration. Besides, it can be observed that this method could be useful in a wide range of application areas, where signals with characteristic non-stationarities at distinct

points in time are considered. One such example would be a kinematic signal with multiple impact regions, which shall be examined in the next section.

TABLE 3-2

RMS AND PEAK ERRORS OF THE CALCULATED ACCELERATIONS CORRESPONDING TO DIFFERENT LEVELS OF ADDED NOISE ABOVE X1 WITH DIFFERENT SNR VALUES DENOISED WITH THE PRESENTED FILTER CIRCUIT (USING BUTTERWORTH FILTERS) AND CONVENTIONAL LOW-PASS FILTERING

SNR(dB) / Method		100	50	10	0	-10	-20	-30
Proposed	RMSE	13.76	13.76	13.99	14.59	17. 81	21.91	28.27
	Peak (%)	2.96	2.96	3.08	9.51	14.07	15.82	34.04
Conventional LP filtering	RMSE	32.09	32.09	32.22	33.65	35.16	34.77	65.07
	Peak (%)	8.08	8.08	8.88	16.38	29.42	43.10	45.15

3.1.1.3 Multiple-Impact Study

The motivation for the work presented here is similar to that of in the previous section. The aim is now to denoise kinematic signals with multiple impacts. The filtering scheme proposed in Figure 3-4 can easily be adopted to work with such signals. Figure 3-6 illustrates a simple version of such a flexible boundary [4].

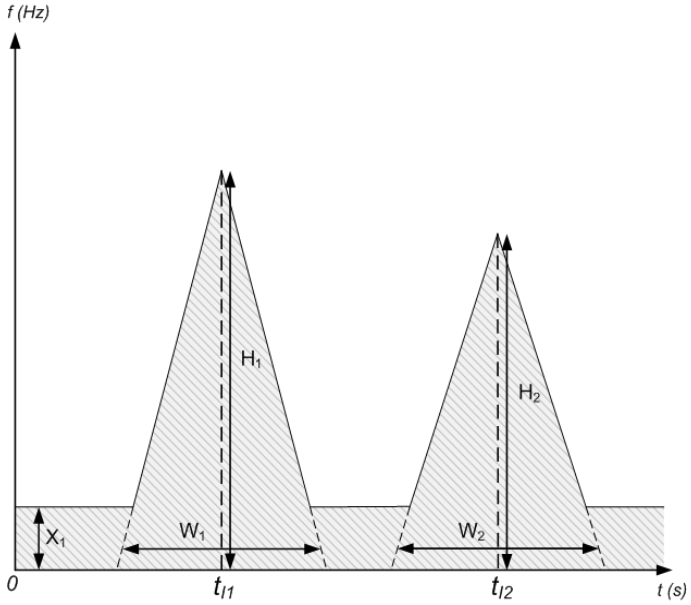

Figure 3-6:

Proposed time-varying filtering boundary. The frequency response of the filter equals to one inside the areas shaded in gray and zero otherwise.

The time-varying cut-off threshold of Figure 3-6 is designed to accommodate two

impact events occurring at times t_{I1} and t_{I2}, respectively. As before, the cutoff frequency X_1 corresponds to the smooth phases of the motion. The widths W_1 and W_2 of the triangles refer to the durations of the two impact regions. The heights H_1 and H_2 of the triangles correspond to the impact-induced expansions of the signal's frequency content in the two impact regions. These parameters were estimated in a similar manner, as before. The appropriate fractional domains in which to filter, as well as the necessary cutoff values can be calculated geometrically, as described in (3.1).

In order to have the desired low-pass effect on the above specified fractional frequency domains, a similar approach as in (3.2) was taken, in which the appropriate filters were convolved in their corresponding fractional time domains. . The required fractional time domains were easily obtained by subtracting 90 degrees from each of the angles $\phi_1$to ϕ_4. This approach allowed us to choose from a wide range of available well-studied low-pass filters (i.e the Butterworth low-pass filter). The overall filter circuit to implement the above scheme is shown in Figure 3-7.

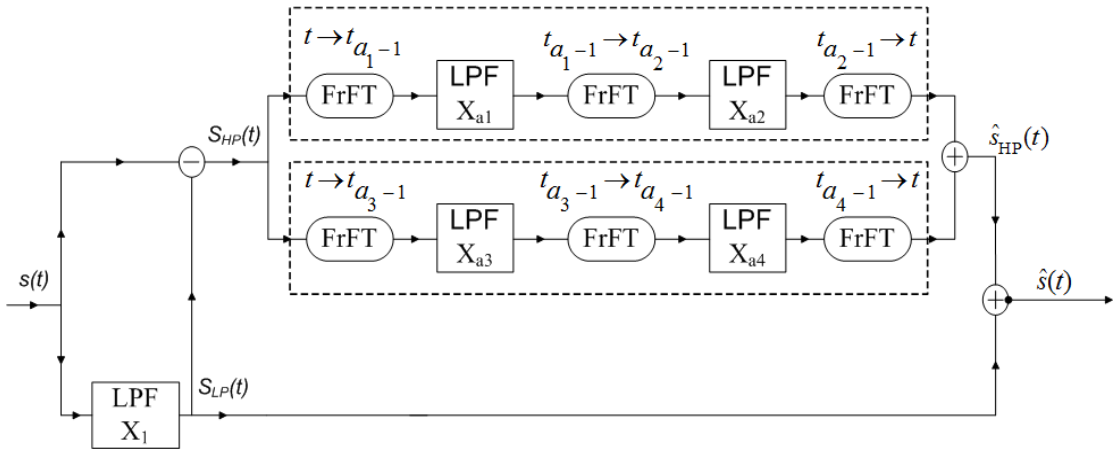

Figure 3-7 *Block diagram of the proposed filter circuit.*

Once more, to gauge its performance, the proposed method is applied on a particular test signal containing 2 impact points. The test signal employed here is the running simulation data provided by Van den Bogert and de Koning [18].

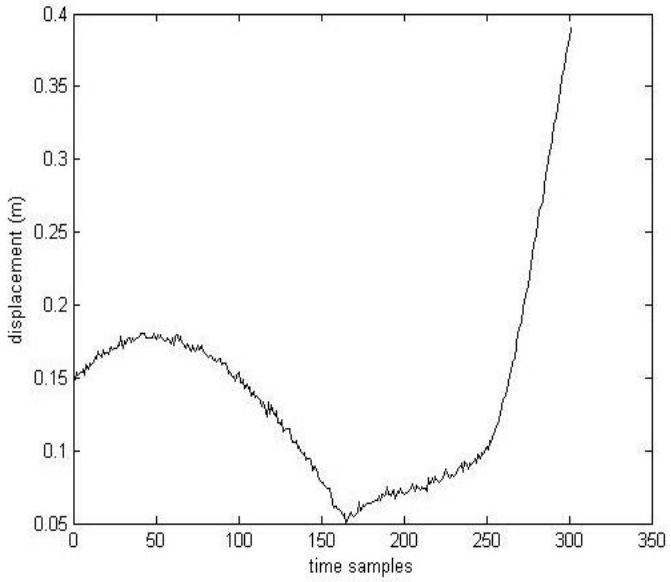

Figure 3-8 *Kinematic signal with added white noise (30dB SNR).*

The motion involved the vertical position history of the ankle resulting from running (as depicted in Figure 3-8). The initial sampling rate was 10000 Hz but the data was subsequently downsampled to 500 Hz to yield a more common sampling rate. This test signal contained two distinct impact regions; the first was the heel strike at time sample 164, followed by the softer forefoot impact at time sample 259. The displacement signal was extrapolated on either edge to compensate for end-point problems. Zero phase (forward and reverse pass) filtering was used throughout to avoid phase-shift distortions. As suggested before, the values for the parameters of both triangles were determined empirically. The accelerations $\widehat{a(t)}$ were computed using the second-order forward differences of the filtered signals and the reference acceleration $a(t)$ was the second derivative of the original clean signal.

Since the test signal was simulated, noise had to be added artificially. To this end, white Gaussian noise at different SNR levels was added to the signal. Table 3-3 presents the overall RMS and acceleration-peak errors achieved after denoising with this new presented

scheme. Peak errors were calculated using (3.4). For comparison, results obtained using a conventional Butterworth filter is also presented in a similar manner as in Section 3.1.1.2.

Figure 3-9 shows the resulted accelerations at 30dB SNR. For the signal at hand, the proposed filter performed well for noise levels down to 10dB SNR, whereas the conventional filter could provide acceptable results only for noise levels higher than 40dB SNR. It should be stressed that the peak in the second derivative of the raw signal was not discernible even for added noise at a level as low as 65dB SNR. Thus, it can be summarized that for a range of signals that exhibit individual non-stationarities, this simple approach adopted here outperforms conventional low-pass filtering because the shape of its cutoff can protect the signal against noise more effectively than a flat cutoff frequency. Finally, it should also be pointed out that, this new presented method can be tailored to accommodate any number of distinct non-stationarities by including additional parallel branches in the block diagram of Figure 3-7, as appropriate.

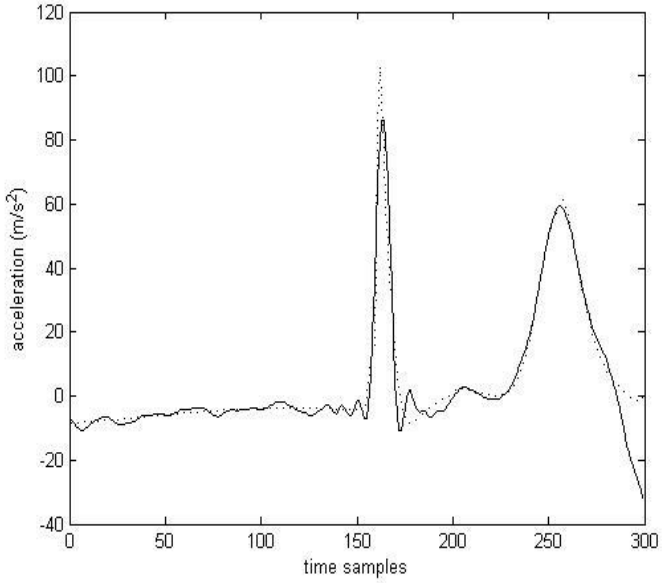

Figure 3-9a:

Calculated acceleration after applying the proposed filter circuit with added white noise at 30dB SNR. The reference acceleration is also shown (dotted lines).

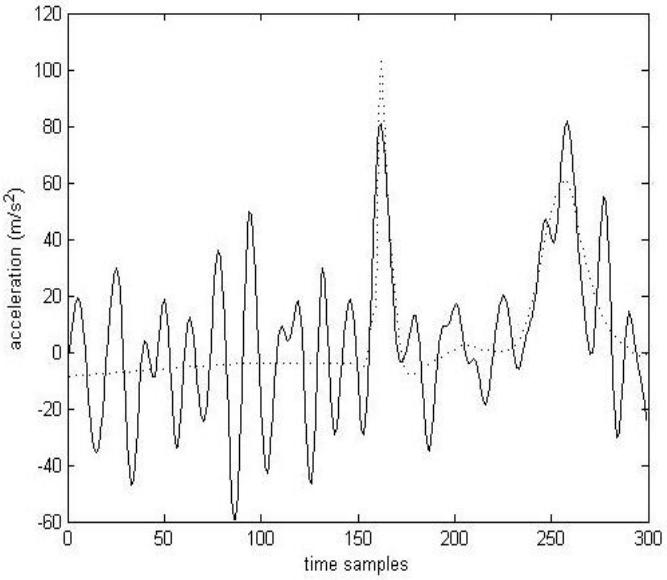

Figure 3-9b:

Calculated acceleration after applying the Butterworth digital low-pass filter at the same SNR level.

TABLE 3-3

RMS AND PEAK ERRORS OF THE CALCULATED ACCELERATIONS FOR DIFFERENT LEVELS OF ADDED WHITE GAUSSIAN NOISE AFTER APPLYING THE PRESENTED FILTER CIRCUIT AND CONVENTIONAL LOW-PASS FILTERING.

SNR(dB) / Method		70	60	50	45	40	30	20	10	0
Proposed	RMSE	1.56	2.94	4.52	5.00	5.86	9.86	12.02	15.33	25.76
	Peak (%)	2.66	5.98	6.70	8.98	10.25	13.17	18.19	25.18	53.86
Conventional LP filtering	RMSE	3.45	10.76	10.93	13.10	14.92	21.45	29.05	48.24	121.67
	Peak (%)	3.21	8.89	9.47	13.32	17.67	24.72	33.51	53.95	94.01

3.1.2 Filtering of Axial Strains in Ultrasound Elastography

This area of application focuses upon the accurate estimation of strain images in the field of ultrasound elastography [5]. In fact, ultrasound elastography is now becoming an important step for imaging the stiffness distribution of soft tissues [19]. It can provide vital information about changes in the tissue stiffness which could be attributed to abnormal pathological processes, such as cancer [20]. The stiffness distribution can easily be estimated from the strain image. A strain image is produced when small amounts of external compression are first applied to the tissue, followed by the estimation of the local displacements in the axial direction using the cross-correlation analysis between gated pre-

and post-compression ultrasonic A-line windows. Finally, the axial strains are calculated as the first order derivatives of the axial displacements [19], [20]. The resulting strain matrix which is typically displayed as a grey scale image is termed the elastogram.

Elastograms consist largely of low frequencies apart from the areas of the boundary between the (healthy) medium and the (potentially malicious) inclusion, where relatively higher frequencies are present. However, the spatial distribution of the tissue scatterers used for displacement tracking undergoes changes under the applied compression (speckle pattern de-correlation) and thus, the measured displacements become corrupted with noise. As it was previously discussed, accurate calculation of higher-order derivatives becomes challenging when noise is present in the measurements. In addition, as it was observed before in the case of biomechanics, conventional filters cannot deal with this problem, especially when the spectral content of the signal changes dramatically with time/space. Therefore, schemes relying on conventional filters, despite their accessibility are unable to denoise elastography signals effectively and yield either under-smoothed or over-smoothed results.

3.1.2.1 Methodology

The denoising method proposed here is essentially based upon the exact idea of filtering as in Section 3.1.1, (i.e. filtering in fractional Fourier domains) so as to realize a space-varying cutoff threshold to overcome the limitations of conventional low-pass filtering. Similarly this could be achieved by means of a simple filter circuit which involves a small number of linear low-pass filters operating in fractional Fourier domains.

In elastography it is known that there are abrupt changes in the displacement estimates around inclusion region of a potential tumor [21]. This is due to the sudden transition between the medium and the inclusion. These abrupt transitions induce higher frequencies in the signal as compared to the overall smooth displacement of the medium and inclusion

regions. Therefore, the filtering threshold should be designed so as to extend toward higher frequencies around the boundary of the inclusion while maintaining a low cutoff value at all other points. Figure 3-10 shows a slice of a space-varying cut-off threshold which was designed to accommodate the medium-to-inclusion and inclusion-to-medium transitions occurring at spatial points x_{p1} and x_{p2}, respectively [5]. The cutoff frequency Δ_1 corresponds to the smooth areas of the displacement. The width W of the triangle refers to the duration of the transition region. The height H of the triangle corresponds to the range of frequencies induced by the transition region. The fact that these parameters are proportional to the physical characteristics of the displacement enables the development of application-specific methods to estimate them, such as the empirical algorithms used in Section 3.1.1.1. The appropriate fractional domains in which to filter, as well as the necessary cutoff values can be calculated geometrically, similar to the process described in (3.1). The overall filter circuit to implement the above scheme is analogous to Figure 3-7.

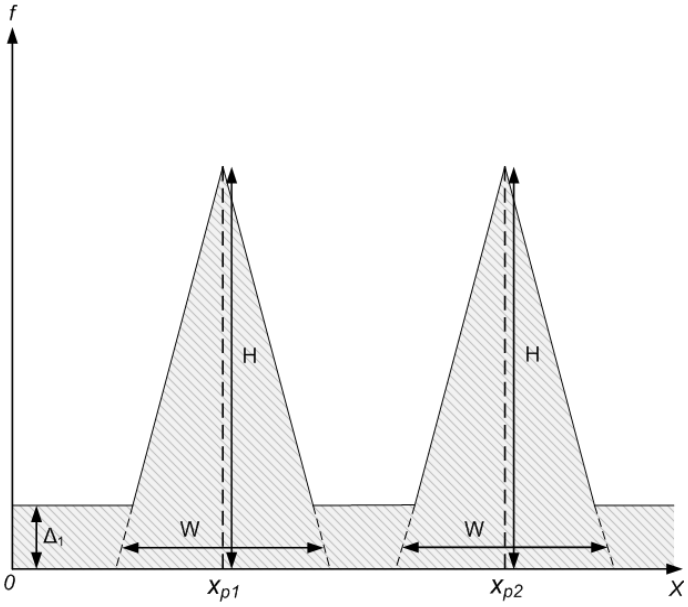

Figure 3-10:

Proposed space-varying cutoff frequency. Only the positive spatial frequencies are shown.

3.1.2.2 Experimental Results

The tissue displacement data that was used in the following experiments was simulated using the 2-D analytic model equations introduced by Muskhlishvili [22]. An ideal mechanical strain image using this 2-D model is depicted in Figure 3-11a. The model assumes that the tissue was subjected to an inward uniaxial compression of 314 Pa, under the condition that the strain is minimal in the outward direction of the plane (plane-strain state). The dimension of the simulated phantom was 100 x 100mm with an inclusion radius of 10mm which is assumed to be 4 times stiffer than the background medium.

The triangles of the filter were centered at the points of transition (i.e. the boundaries of the inclusion). Zero phase (forward and reverse pass) filtering was used throughout to avoid phase-shift distortions during the filtering process. The values of the parameters of both triangles were determined empirically in a similar manner as before. The strain signal was computed using first-order forward differences of the filtered signal and the reference strain was the first derivative of the original displacement signal.

Zero mean white Gaussian noise was added to the simulated 2-D tissue displacement field. The level of noise that was added to the signal was 26dB SNRst (where SNRst is the equivalent signal-to-noise ratio in the strain signal). The resulting elastogram is illustrated in Figure 3-11b. It can be observed how severely the differentiation process amplifies the amount of noise and degrades the strain profiles. The contrast-to-noise ratio (CNRe) proposed in [23] was used to evaluate the performance of the proposed filter. This performance measure can be expressed as follows:

$$\mathrm{CNR_e(dB)} = 20\log_{10}\left(\frac{2(\mu_{s1}-\mu_{s2})^2}{(\sigma_{s1}^2+\sigma_{s2}^2)}\right) \tag{3.5}$$

where μ_{s1} and μ_{s2} represent the mean value of strain in the inclusion and the medium, and σ_{s1} and σ_{s2} denote the strain variances, respectively. A high CNRe signifies a readable elastogram whereas low values of this metric indicate a poor image. The noisy

displacement and calculated strain profile along the centre of the inclusion of the elastogram are depicted in Figure 3-12a and Figure 3-12b, respectively.

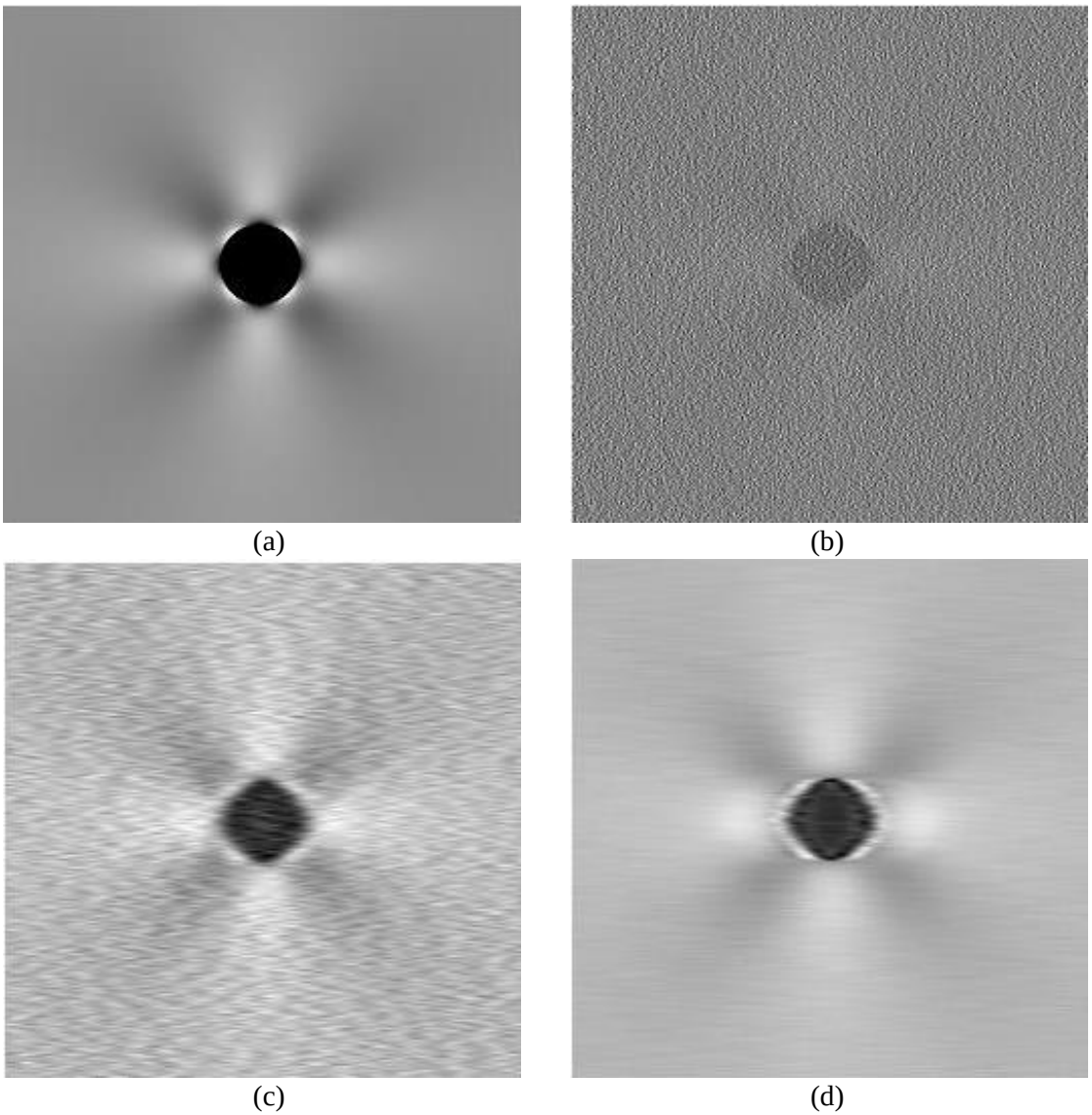

Figure 3-11 *(a) The ideal elastogram, and (b) the corrupted elastogram (SNRst = 26dB). Calculated elastogram after denoising with: (c) the Butterworth digital low-pass filter, and (d) the proposed filter circuit.*

For comparisons, results obtained using a conventional Butterworth filter were also presented. The cutoff frequency for the conventional Butterworth filter as well as its order were empirically determined so as to maximize the overall quality of the corresponding elastogram with respect to the ideal strain image (maximize the obtained CNRe result) . For all comparisons 100 realizations of the noisy displacement input were implemented. Figures 3-11c and 3-11d show the filtered elastograms; their corresponding strain profiles

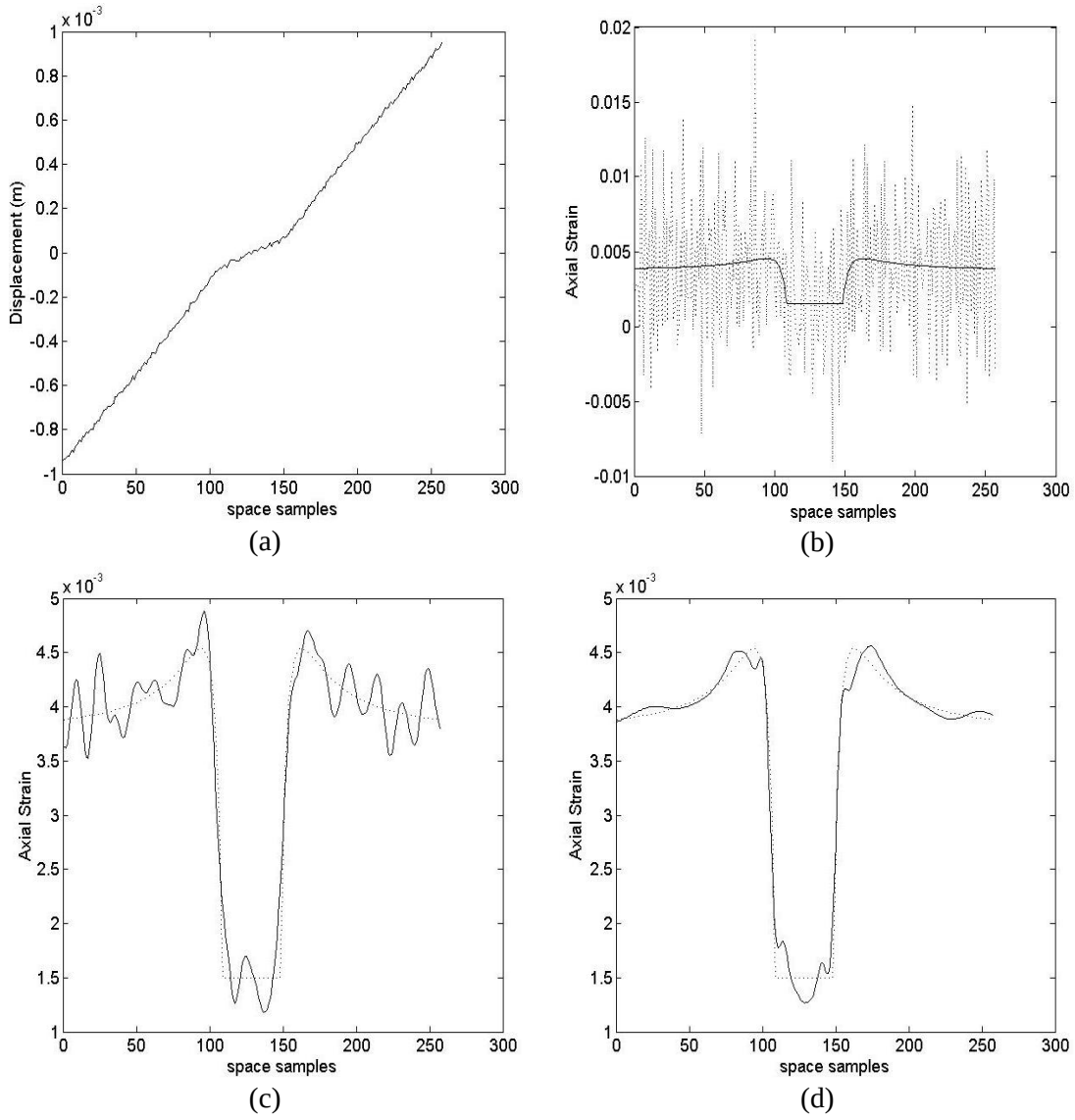

Figure 3-12 *(a) Noisy displacement profile taken along the center of the displacement image (b) Calculated axial strain slice (dotted line) taken along the center of the elastogram (SNR_{st} = 26dB) contrasted to the ideal axial strain (solid line). Corresponding axial strain slice after denoising with: (c) the Butterworth digital low-pass filter (solid line), and (d) the proposed filter circuit (solid line). The reference axial strain is also shown (dotted line).*

along the center of the inclusion are depicted in Figures 3-12c and 3-12d. The proposed filter resulted in a CNRe value of 56.92dB whereas the conventional filter achieved a lower ratio of 52.21dB, as expected. The CNRe values achieved at different SNR levels by the proposed scheme and the conventional filter are presented in Figure 3-13.

Therefore through this work, an alternative filtering scheme for denoising elastograms has been devised. The method improves the CNRe of the elastogram by providing a space-varying cutoff threshold that can accommodate the distinct non-stationarities caused by the

sudden changes in the tissue stiffness. Experimentation with clinical data could be conducted in the future, to assess the potential of the proposed method with actual elastographic measurements.

3.2 Discussion

So far, it has been well understood that the best strategy for denoising highly non-stationary signals like the examples presented in Section 3.1.1 and 3.1.2, is to employ a cut-off threshold that follows the time evolution of their frequency content. T-F analysis has provided a convenient platform for such operations leading to more accurate results than traditional methods. Nevertheless, although the design of appropriate time-variant

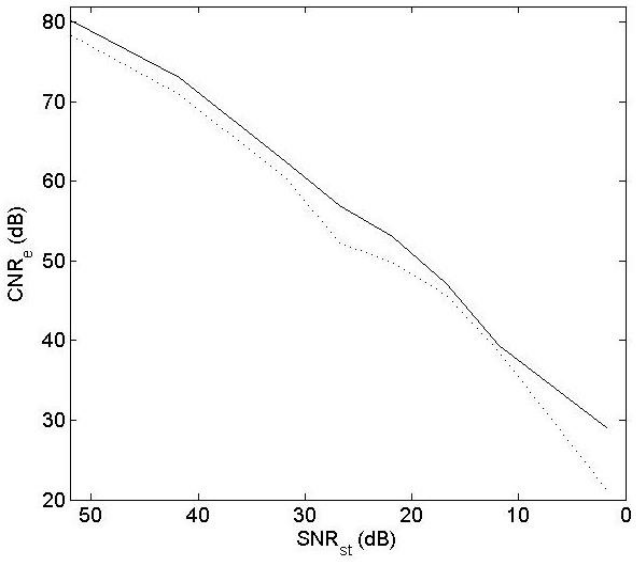

Figure 3-13 *Contrast-to-noise ratio achieved for different strain signal-to-noise ratios by the proposed filter (solid line) and the Butterworth digital low-pass filter (dotted line).*

thresholds is facilitated in the T-F plane, masking approaches in the T-F domain itself result in highly non-linear schemes. In all of the presented filtering schemes, the rotated T-F concept discussed in Section 2.2 has been exploited, so as to determine the time-variant cutoff boundary and furthermore, implemented it in rotated T-F domains (i.e. FrFT filtering). Essentially, by taking advantage of the relationships between the FrFT and the

WD one is able to reduce the non-linear, two-dimensional low-pass T-F masking process into a series of linear filters operating in predetermined one-dimensional fractional Fourier domains. The presented triangular scheme in both applications requires no more than two conventional low-pass filters cascaded in-between appropriate fractional Fourier transformations.

Moreover, the flexibility offered by filtering in fractional Fourier domains overcomes the limitation of the fixed cutoff frequency imposed by classical Fourier domain filters. As a consequence, approaches such as the ones adopted in these examples, can protect a signal against noise more effectively without distorting its useful features, i.e. edges or other transients of interest. The success of filtering in fractional Fourier domains relies on certain key variables such as the FrFT orders, the applied filtering functions, and the structure of the filter circuit. The problem of optimally determining these factors is non-trivial and remains largely unexplored. In both Sections 3.1.1 and 3.1.2, the fractional orders, the cutoff values, and the overall filter configuration employed were specified in the T-F domain, based on the geometry of the designed cutoff frequency threshold. The choice of the specific, simple triangular boundary was motivated by the nature of both applications and was vindicated by the quality of the obtained results. Furthermore, it should also be stressed that the advantages achieved whilst filtering in fractional Fourier domains, come at a very low computational cost, since the complexity of the FrFT itself is $O(NlogN)$ [24], which is identical to that of the classical Fourier transform.

An additional comparative advantage of the proposed triangular filtering scheme is that its parameters are physically meaningful in both of the presented applications. For instance in the case of the kinematic signals, parameter H represents the range of frequencies applied on the body upon impact. These frequencies constitute the resultant transient shock wave which travels throughout the skeletal structure. Thus, the method does not only remove noise from the signal but can also provide useful information on the intensity of

impact loading. In contrast, wavelets involve scales that do not have an exact match with natural frequencies/vibrations. On the other hand, the WD-based filter – although it employs a similar time-variant boundary – cannot provide meaningful parameters due to its non-linear characteristics. This is because its boundary's values have to be adjusted to deal with the existence of cross-terms and the propagation of noise in the passband area. Consequently, the parameters used by that method do not accurately represent the frequency content of the signal. A similar argument also holds for the case of elastograms.

3.2.1 Alternative Implementation

As previously mentioned, the proposed filter circuits belong to the class of generalized filtering configurations described in [15]. These may include series and parallel interconnections of linear time-invariant filters placed in-between FrFTs of appropriate orders. Determining the optimized structure for such a circuit in general is a non-trivial problem. Therefore, an additional advantage of the proposed approach is that it facilitates the design of the circuit based on the required time-varying cutoff frequency threshold. Of course, there may exist more than one possible configuration for achieving the same filtering result. One such alternative solution to the circuits presented before (e.g. Figure 3.4) is the system depicted in Figure 3-14. This system operates as follows:

The signal is first low-pass filtered by X_1 to separate the low-frequency component from the high-frequency component, as before. Then the high-frequency component is passed through the parallel filter circuit, as shown in Figure 3-14, with the aim of isolating and subsequently subtracting the noise. The T-F plane depicted in Figure 3-15 is the resultant T-F distribution from the upper branch. The region of white space indicates the absence of any waveform. This is expected since a high pass filter was used. Similarly Figure 3-16 illustrates the resultant T-F distribution from the lower branch.

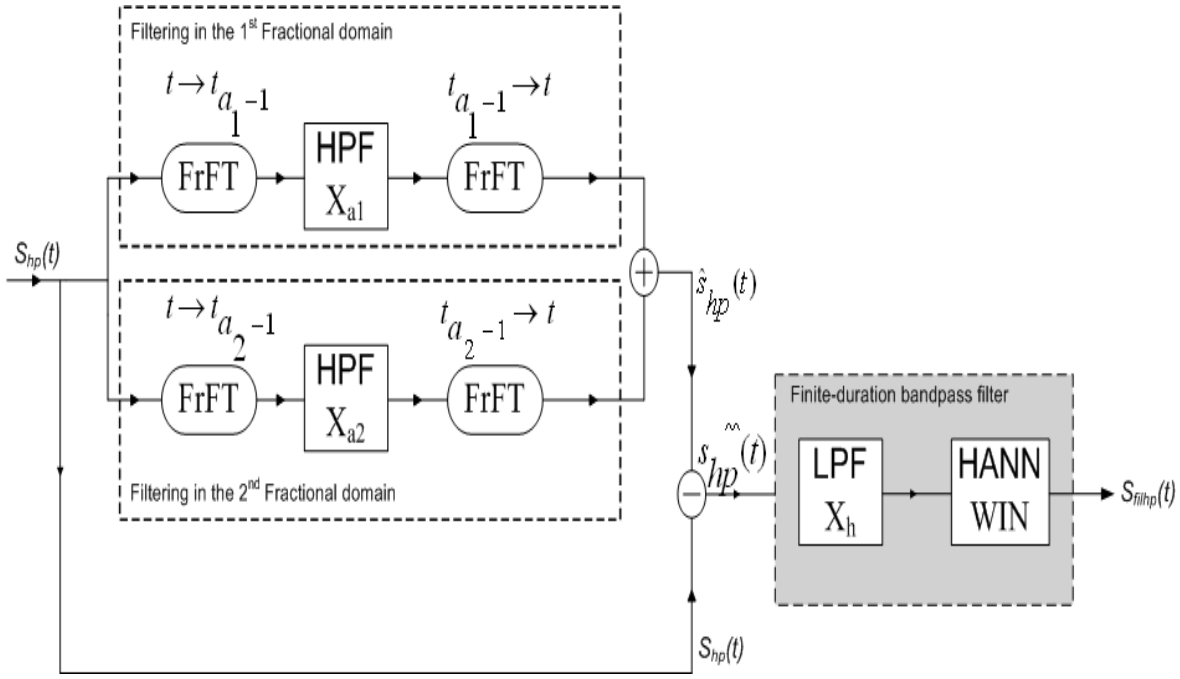

Figure 3-14 *Block diagram of the alternative filter circuit.*

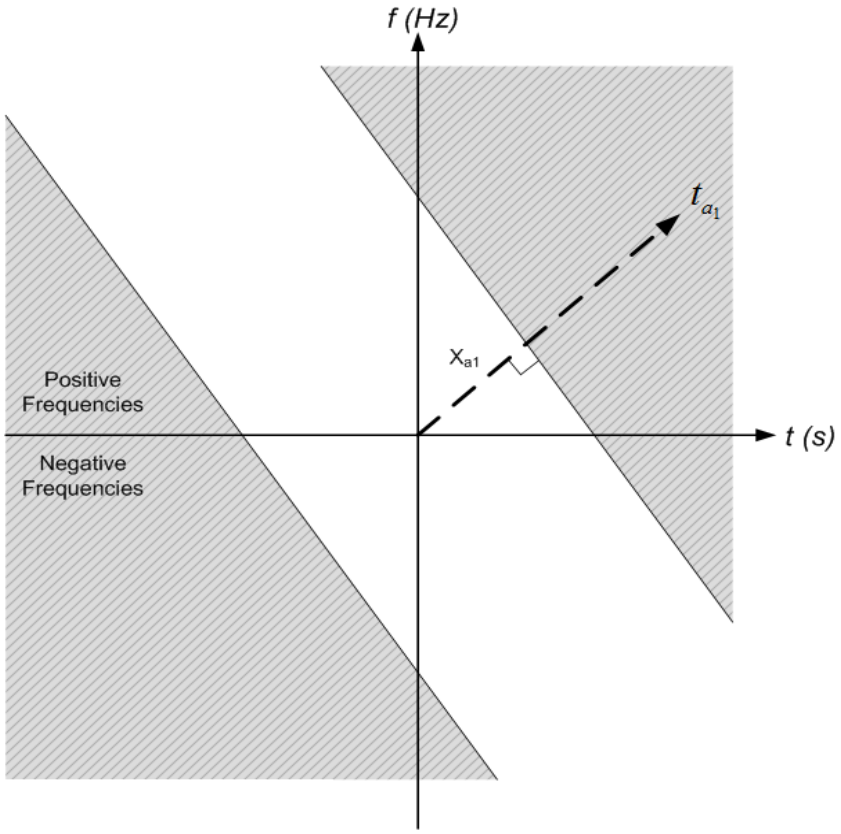

Figure 3-15 *Resultant T-F distribution after filtering using the upper branch.*

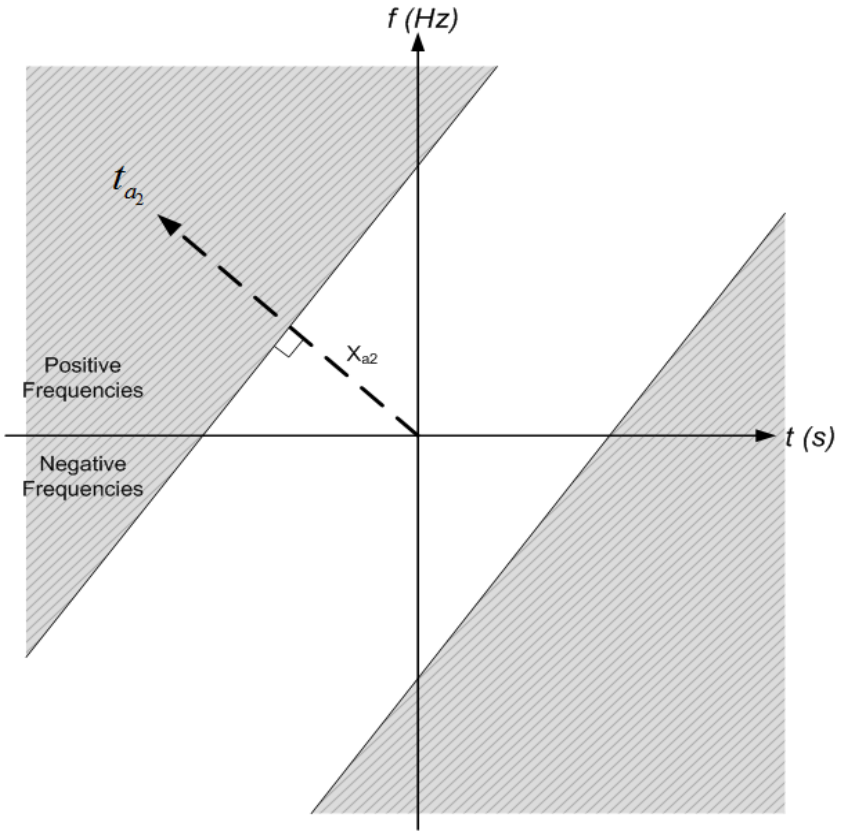

Figure 3-16 *Resultant T-F distribution after filtering using the lower branch.*

Next, these two filtered waveforms are then combined to form $\hat{S}_{hp}(t)$. The resulting T-F distribution for this new signal is shown in Figure 3-17. It can be observed that this new signal now includes overlapping noise regions around the vertices of the rhombus, indicated by the darker shades.

To restore back the original signal and consequently remove the different regions of noise, the filtered signal $\hat{S}_{hp}(t)$ is first subtracted with the original high frequency component of the signal, as shown in Figure 3-14. The result, depicted in Figure 3-18, now includes the useful signal components, indicated by the solid area. However it can still be observed that there are some noisy regions around the vertices of the rhombus. This can be easily removed by applying a finite-duration bandpass filter around the boundary of the rhombus as portrayed in Figure 3-18. It is accomplished by applying a low-pass filter on the signal with the cut-off frequency (X_h) being equal to H and then followed by

windowing in time with the duration, now being equal to the width of the triangle, *W*. Experiments with all possible windows (Blackman, rectangular, hamming, Kaiser, Gaussian and etc.) were performed, and the results indicated that the Hanning window was the most suitable choice, as it introduced the least amount of distortions at the edges of the filtered signal.

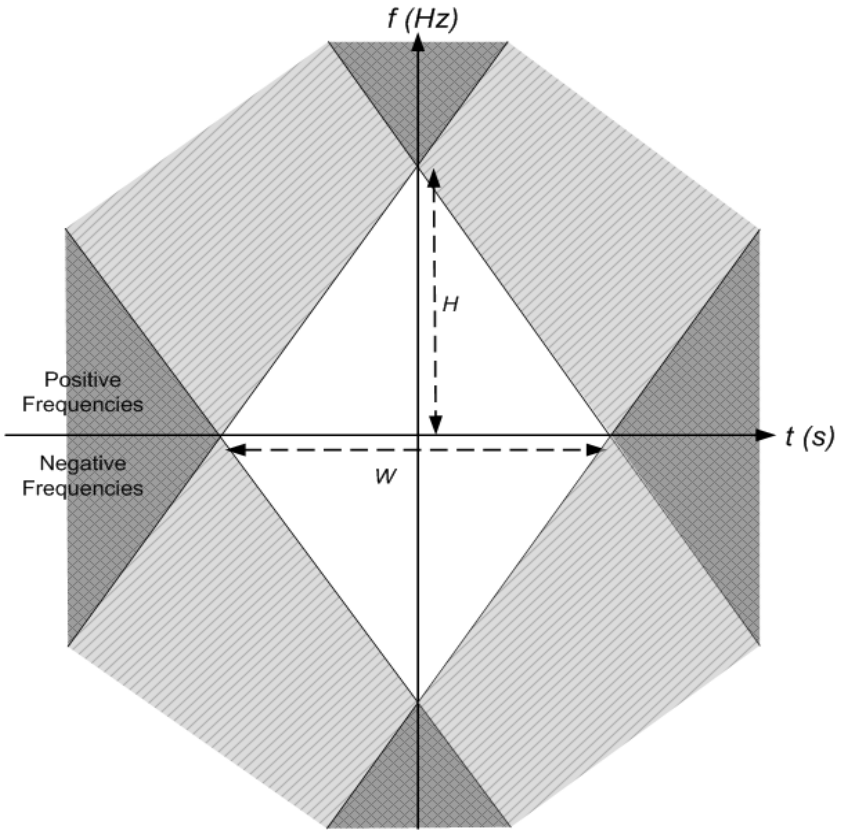

Figure 3-17 *T-F distribution of* $\hat{S}_{hp}(t)$.

Once again, the appropriate fractional domains in which to filter, as well as the necessary cutoff values can be calculated geometrically, based on the parameters *H*, and *W*, as described in (3.1). This approach can easily be extended to accommodate multiple non-stationarities. Despite the fact that the above circuit is equivalent to the one in Figure 3-4, it can be observed that the implementation is actually more complicated as compared to the

former serial filtering approach. The reason for discussing this alternative implementation is solely to showcase the flexibility in designing these filter circuits.

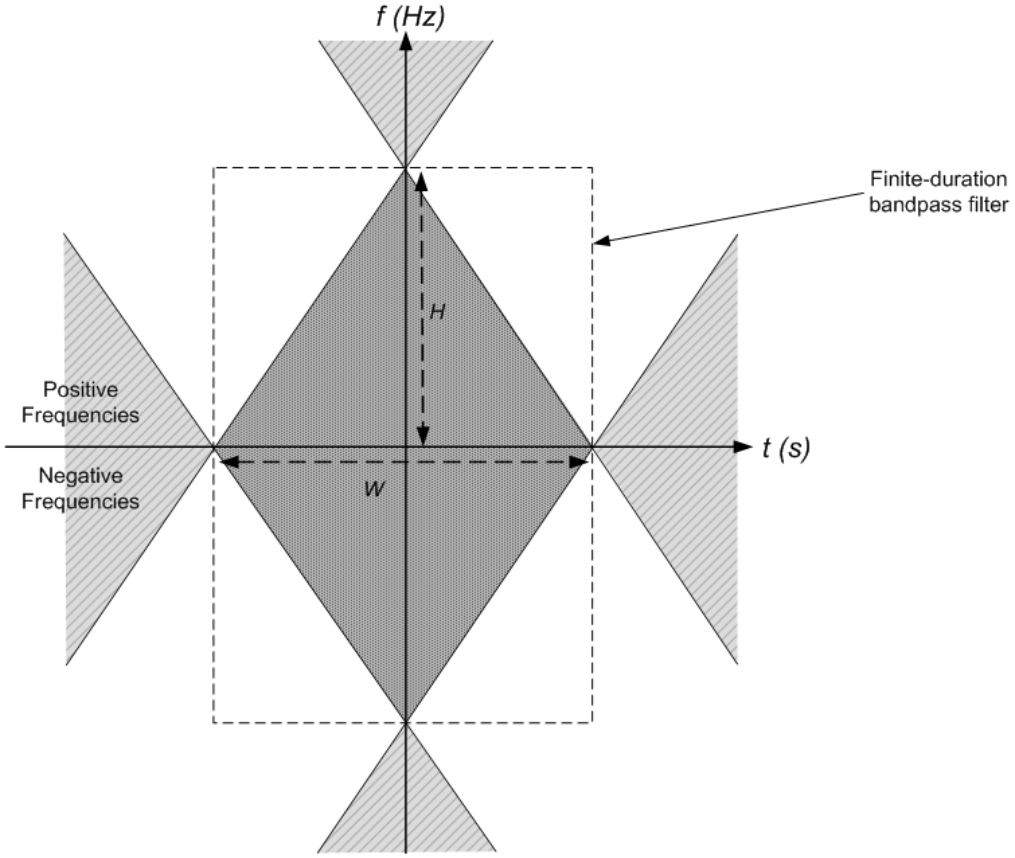

Figure 3-18 *T-F plane of the resultant signal after subtraction.*

3.3 Summary/Key Contributions

In this chapter, the application of FrFT-based filtering on real-world problems has been presented for the first time in the literature. Particularly, the proposed two-stage fractional Fourier filtering scheme has been successfully applied to denoise biomechanical impact signals and ultrasound elastograms. The choice of the specific, two-stage filtering scheme was motivated by the nature of both applications and can be vindicated by the quality of the presented results. The fractional orders, the cutoff values, and the overall filter configuration employed in all the examples presented in sections above, were specified

manually in the T-F domain, informed by the geometry of the designed cutoff frequency threshold. This was made possible by the choice of the simple triangular boundary, which in turn, was again motivated by the nature of the signals used.

However, in some cases, it might become a bit difficult to determine the exact nature or behavior of certain types of signals and thus affecting the design of the filtering boundary. In such scenarios, the implementation of a filtering configuration yielding an optimized passband may be more of an appropriate choice. On the other hand, the problem of optimally designing such systems is non-trivial and remains largely unexplored. Thus in the remaining chapters of this report, the challenges faced are further explored and novel techniques in designing these optimized estimators are subsequently proposed.

Appendix

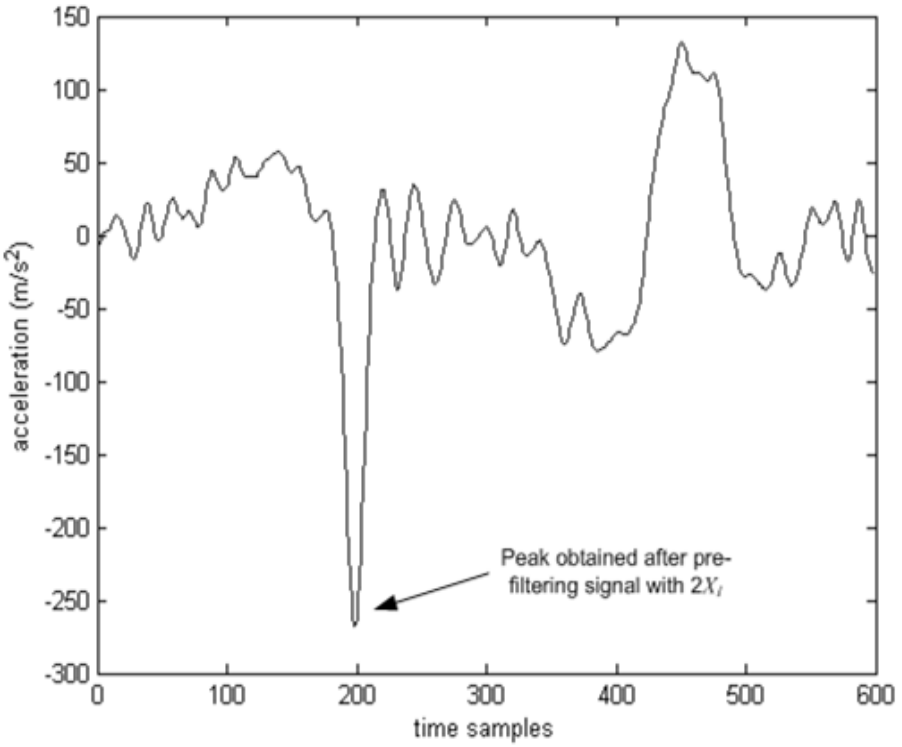

Figure 3-19 *Using the signal S1 to depict the detection algorithm for the time of impact,* t_I

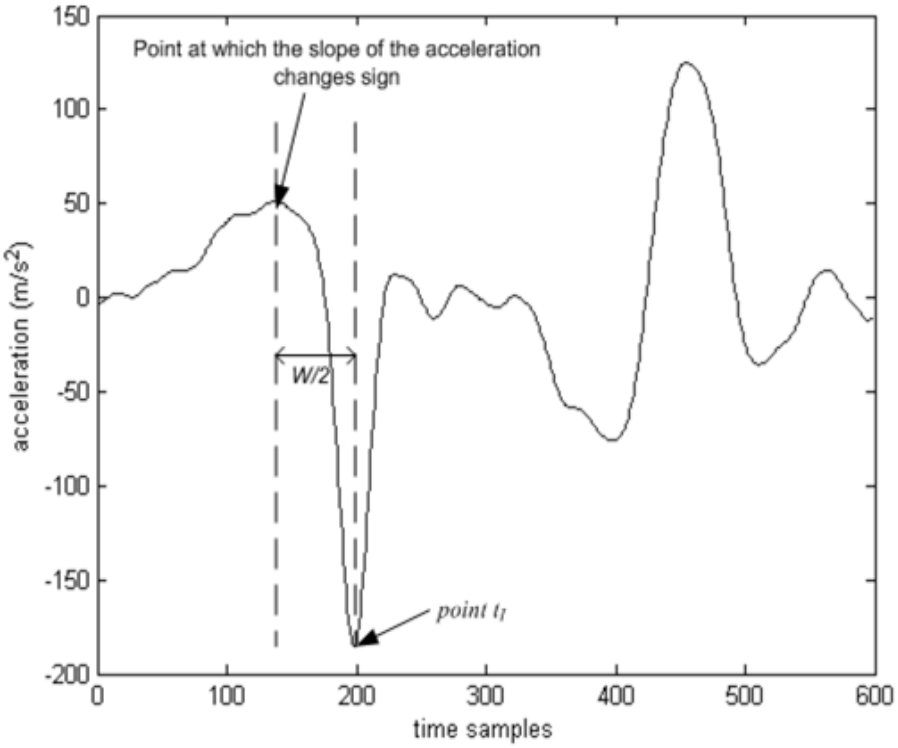

Figure 3-20 *Using the signal S1 to depict the detection algorithm for the width of the triangle,* ***W*** *(duration of impact)*

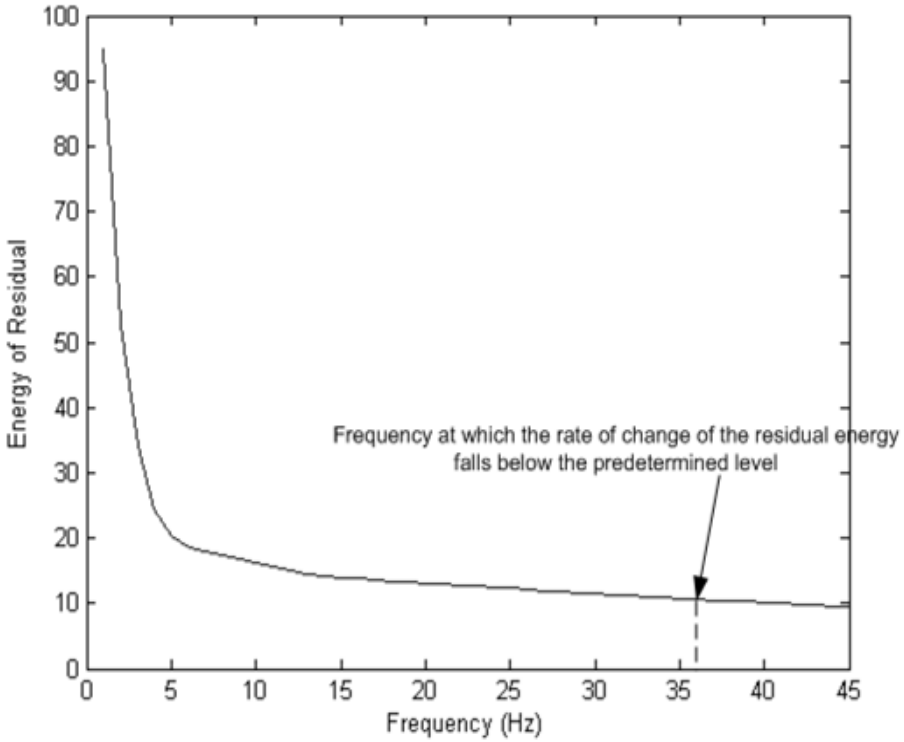

Figure 3-21 *Using the signal S1 to depict the detection algorithm for the height of the triangle,* ***H*** *(maximum frequency range induced by the impact)*

References

[1] S.R. Subramaniam. Filtration of Non-Stationary Signals In the Fractional Fourier Domain: Accurate Estimation of the Acceleration of Impact Signals. MSc. Thesis, King's College London, London, 2007.

[2] A. Georgakis, and S.R. Subramaniam, "Estimation of the second derivative of kinematic impact signals using fractional Fourier filtering", IEEE Trans. Biomed. Eng., vol. 56, pp. 996-1004, 2009.

[3] S.R. Subramaniam, and A. Georgakis, "A Simple Filter Circuit for denoising Biomechanical Impact Signals", 31st Annual International Conference of the IEEE Engineering in Medicine and Biology Society (EMBC), 2009, Minneapolis, Minnesota.

[4] S.R. Subramaniam, and A. Georgakis, "Fractional Fourier-based denoising of kinematic signals with multiple impacts", 10th International Symposium on Information Science, Signal Processing and their Applications (ISSPA), 2010, Kuala Lumpur, Malaysia.

[5] S.R. Subramaniam, Tsz K. Hon, A. Georgakis, and George Papadakis "Fractional Fourier-Based Filter for denoising Elastograms", 32nd Annual International Conference of the IEEE Engineering in Medicine and Biology Society (EMBC), 2010, Buenos Aires, Argentina.

[6] H. Hatze, "The fundamental problem of myoskeletal inverse dynamics and its implications," J. Biomech., vol. 35, pp. 109-115, 2002.

[7] J. A. Walker, "Estimating velocities and accelerations of animal locomotion: A simulation experiment comparing numerical differentiation algorithms," J. Exp. Biol., vol. 201, pp. 981-985, 1998.

[8] H. J. Woltring, "Smoothing and differentiation techniques applied to 3-D data," in Three-Dimensional Analysis of Human Movement, P. Allard, I. A. F. Stokes, and J.-P. Blanchi, Eds., Champaign, IL: Human Kinetics 1995, pp. 79-99.

[9] G. Giakas and V. Baltzopoulos, "A comparison of automatic filtering techniques applied to biomechanical walking data" J. Biomech., vol. 30, pp. 847-850, 1997.

[10] A.R. Ismail, and S.S. Asfour, "Discrete wavelet transform: A tool in smoothing kinematic data," J. Biomech., vol. 32, pp. 317-321, 1999.

[11] M. P. Wachowiak, G. S. Rash, P. M. Quesada, and A.H. Desoky, "Wavelet-based noise removal for biomechanical signals: A comparative study," IEEE Trans. on Biomed. Eng., vol. 47, pp. 360-368, 2000.

[12]A. Georgakis, L. K. Stergioulas, and G. Giakas, "Wigner filtering with smooth roll-off boundary for differentiation of noisy non-stationary signals", Signal Processing, vol. 82, pp. 1411-1415, 2002.

[13]A. Georgakis, L. K. Stergioulas, and G. Giakas, "An automatic algorithm for filtering kinematic signals with impacts in the Wigner representation", Medical & Biological Engineering & Computing, vol. 40, pp. 625-633, 2002.

[14]J. Dowling, "A modeling strategy for the smoothing of biomechanical data", in Biomechanics, B. Johnsson, Ed., Champaign, IL: Human Kinetics 1985, pp. 1163-1167.

[15]H. M. Ozaktas, Z. Zalevsky, and M. A. Kutay, The Fractional Fourier Transform with Applications in Optics and Signal Processing. New York: Wiley, 2001.

[16]M. D'Amico, and G. Ferrigno, "Technique for the evaluation of derivatives from noisy biomechanical displacement data using a model-based-bandwidth-selection procedure", Med. Biol. Eng. Comput., vol. 28, pp. 407-415, 1990.

[17]D.L. Donoho, "De-noising by soft thresholding", IEEE Trans. Inform. Theory, vol. 41, pp. 613-627, 1995.

[18]Bogert, A.J. van den, and J.J. de Koning, "On optimal filtering for inverse dynamics analysis," Proc. 9th CSB Congress, Burnaby, B.C., pp. 214-215, 1996.

[19]J. Ophir, I. Cespedes, H. Ponnekanti, Y. Yazdi and X.Li, "Elastography: A quantitative method for imaging the elasticity of biological tissues", Ultrasonic Imaging,vol. 13, pp. 111-134, 1991.

[20]M. O'Donnell, A.R. Skovoroda, B.M. Shapo and S.Y.Emelianov, "Internal displacement and strain imaging using ultrasonic speckle tracking", IEEE Trans. Ultrason. Ferroelect. Freq. Contr., vol. 41, no. 3, pp. 314-325, 1994.

[21]U. Techavipoo and T. Varghese, "Wavelet denoising of displacement estimates in elastography", Ultrasound. Med. & Biol., vol. 30, no. 4, pp. 477-491, 2004.

[22]Muskhelishvili NI. Some Basic Problems of the Mathematical Theory of Elasticity. Groningen, The Netherlands: Noordhoff, 1963 (transl. from Russian by JRM Radok); Chap. 9; pp. 216-223.

[23]Varghese T, Ophir J. "An analysis of elastographic contrast-to-noise ratio performance", Ultrasound Med. & Biol. 1998; 24:915-924.

[24]H. M. Ozaktas, O. Arikan, M. A. Kutay, and G. Bozdagi, "Digital computation of the fractional Fourier transform," IEEE Trans. Sig. Proc., vol. 44, pp. 2141-2150, 1996.

[25]Delph, SL, Arnold, AS, Speers RA and Moore, CA. Hamstrings and psoas lengths during normal and crouch gait: Implications for muscle-tendon surgery, Journal of Orthopedic Research 14(1), 144-151, 1996.

[26]Delph, SL, Loan, P., Basdogan, C. and Rosen, JM. Surgical simulation: An emerging technology for training in emergency medicine, Presentce-Teleoperators and Virtual Environments 6(2), 147-159, 1997.

[27]Piazza, SJ, Delph, SL, Stulberg, SD and Stern, SH. Posterior tilting of the tibial component decreases femoral rollback in posterior-substituting knee replacement: A computer simulation study, Journal of Orthopedic Research 16(2), 264-270, 1998.

[28]Yu, B. and Andrews, JG. The relationship between free limb motions and performance in the triple jump, Journal of Applied Biomechanics 14(2), 223-237, 1998.

[29]Nigg, BM, Khan, AR, Fisher, V. and Stefanyshyn, D. Effect of shoe insert construction on foot and leg movement, Medicine and Science in Sports and Exersice 30(4), 550-555, 1998.

[30]Tsirakos D., Baltzopoulos V. and Bartlett RM. Inverse optimization: Functional and physiological considerations related to the force-sharing problem, Critical Reviews in Biomedical Engineering 25(4-5), 371-407, 1997.

Chapter 4

Optimal Filtering in a Single FrFT Domain

It has been established that filtering in rotated time-frequency domains (i.e. fractional Fourier filtering) can lead to significant performance advantages for certain types of signals as compared to conventional linear time invariant systems. In this chapter, the process of designing an optimized estimator to operate in a single FrFT domain is described. The work described in this chapter has been reported in [1].

Introduction

Linear time-invariant (LTI) filtering has enjoyed unparalleled popularity mainly thanks to its ease of implementation. However, it is known that such an approach is limiting for a multitude of signal processing purposes, as illustrated in previous chapters. The problem lies with the fact that the frequency response of an LTI filter is fixed over time. Therefore, unless the observed signal's frequency content remains unchanged with time (stationary signal) – or at least is made up of intervals of stationary behavior and sufficient duration for the local adjustment of the system's frequency response using adaptive methods – the LTI filter may produce poor results.

Ideally, a filter should be able to trail the temporal evolution of the non-stationary signal's frequency content, as illustrated in examples of Chapter 3. The time-variant thresholds used in the previous chapter were realized through the fractional domain-convolution process described in (2.19). Another approach in implementing these time-varying cutoff boundaries is to refer to the joint time-frequency (T-F) domain, which has

indeed provided a convenient platform for the description and understanding of such systems. Since the T-F representation of a signal can unfold its frequency content over time, the desired time-varying pass band can potentially be identified. Then, one can operate directly in the T-F plane by first isolating the selected area and subsequently recovering the portion of the signal therein using synthesis techniques [2], [3]. Alternatively, the signal can be decomposed in the eigenvector basis of the T-F subspace indicated by the specified region [4], [5]. Although these methods can offer great flexibility in relation to the shape of their pass bands, in real-life problems it may be difficult to determine the required T-F regions in such detail. Moreover, it may not be practical to compute the T-F representation of a given signal each time it changes.

In cases where the signals of interest generally lie within narrow tilted areas in the T-F plane then such schemes as the 'swept-frequency filters' [6], the 'strip filters' [7], [8] and the 'fractional Fourier domain filters' [9] have been proposed for their treatment. These approaches amount to simple linear time-varying operators. In fact, as discussed in [8], they can further be viewed as special cases of the filtering methodologies based on the Weyl correspondence [5], where the T-F (Weyl) symbol has been restricted to a strip. All of these methods were developed independently, but are closely related as they are all founded on the concept of T-F rotation. As described in Section 2.2, T-F rotation is a transformation of the signal into domains represented in general as oblique axes in the T-F plane. Therefore, filtering in a rotated domain may be realized as the concatenation of three operations; a T-F rotation, a modification in the resulting domain via a multiplicative window, and an inverse T-F rotation.

An optimized estimator of the required multiplicative function was discussed in [10], while the rotation angle was determined based on a trial-and-error approach. In particular, the profile of the window was estimated such that the mean square error (MSE) between the desired signal and the output of the system was minimized. The underlying observation

model comprised a multiplicative degradation process, and additive zero-mean noise which was further considered to be independent of the desired signal. The degradation operator, as well as the auto-correlation matrices of the signal and the corrupting noise were assumed to be known.

Although in certain applications it may be possible to make the above assumptions, there is a wide range of signal processing problems in which a degree of dependency may exist between the noise and the ideal signal. Furthermore, noise may not be a strictly zero-mean process. In such cases, the solution proposed in [10] will only yield suboptimal results. What is worse, when the statistics of the noise are unavailable altogether, the above solution cannot be used at all. Therefore in this chapter, the design of an optimum estimator operating in a specific FrFT domain is presented, in which the need for any assumptions about the noise model is eliminated.

4.1 Proposed Filter Design

4.1.1 Problem Formulation

In this work, the input signal and the corrupting noise are considered to be discrete-time, finite-length random processes of size *N*. In measurements under additive noise, the following observation model can be assumed in discrete form:

$$\boldsymbol{y} = \boldsymbol{x} + \boldsymbol{n} \ , \tag{4.1}$$

where $\boldsymbol{y}, \boldsymbol{x}, \boldsymbol{n}$ are column vectors of size *N* representing the acquired signal, the desired signal, and the noise, respectively. The goal of the filter is to find an estimate $\hat{\boldsymbol{x}}$ which would be as close as possible to the ideal $\boldsymbol{x}$. A natural optimality criterion is the mean square error (MSE),

$$\text{mse}(\hat{\boldsymbol{x}}) = \frac{1}{\text{N}} \text{E}[\|\hat{\boldsymbol{x}} - \boldsymbol{x}\|^2] \ , \tag{4.2}$$

where $\|\boldsymbol{z}\|^2$ denotes the 2-norm of the vector $\boldsymbol{z}$, that is, $\|\boldsymbol{z}\|^2 = \boldsymbol{z}^H \boldsymbol{z}$.

In line with the process describing a single-stage FrFT-based filter in (2.18), the estimate $\hat{\boldsymbol{x}}$ can be obtained as:

$$\hat{\boldsymbol{x}} = F_{-a} G F_a \boldsymbol{y} \,, \tag{4.3}$$

where $F_{a\ (\mathrm{NxN})}$ and $F_{-a(\mathrm{NxN})}$ are the discrete FrFT matrices (as stated in 2.21) which correspond to the transformations of order a and $-a$, respectively; $G_{(\mathrm{NxN})}$ is a diagonal matrix whose elements are composed of the filter's fractional-frequency response $\boldsymbol{g}$,

$$G = \begin{bmatrix} g_0 & 0 & \cdots & 0 & 0 \\ 0 & & & & 0 \\ \vdots & & \ddots & & \vdots \\ 0 & & & & 0 \\ 0 & 0 & \cdots & 0 & g_{N-1} \end{bmatrix},$$

thus, $\boldsymbol{g} = diag(G) = (g_0, \ldots, g_{N-1})$. The objective is then to determine the vector $\boldsymbol{g_{opt}}$ which minimises (4.2).

A possible solution to the problem above has been proposed in [10]. The design steps can be summarised as follows:

Starting with the optimum estimator presented in [10],

$$g_{opt,j} = \frac{E[x_{a,j}\ y^*_{a,j}]}{E[y_{a,j}\, y^*_{a,j}]} \,, \tag{4.4}$$

where $x_{a,j}$ is the j^{th} element of the vector $\boldsymbol{x}_a = F_a \boldsymbol{x}$, and similarly for $y_{a,j}$, plus under the assumption of statistical independence between the noise and the desired signal, along with, given that the noise is a zero-mean process, (4.4) can be re-written as:

$$g_{opt,j} = \frac{E[x_{a,j}\ x^*_{a,j}]}{E\left[x_{a,j}\, x^*_{a,j}\right] + E\left[n_{a,j}\, n^*_{a,j}\right]} \,. \tag{4.5}$$

Alternatively;

$$g_{opt}, j = \frac{E\left[|x_{a,j}|^2\right]}{E\left[|x_{a,j}|^2\right] + E\left[|n_{a,j}|^2\right]} \tag{4.6}$$

which can be seen as taking the ensemble average energy density of the signal at the fractional frequency sample j and dividing by the sum of the ensemble averages of the energy densities of the signal and noise at the same fractional frequency sample.

Therefore, to determine $\boldsymbol{g_{opt}}$ knowledge of the statistics of the desired signal and the corrupting noise is required. In practice, since (4.5) refers to ensemble averages of the ideal signal and noise processes, approximations of the optimized window $\boldsymbol{g_{opt}}$ may be obtained if a number of realisations can be recorded independently for both the signal and the noise – and then transformed into the appropriate domain. It is clear that such a requirement restricts the applicability of the above solution.

Therefore, in this work, an alternative route to the filter design problem is taken by estimating (4.2) with the average error over *M* realisations,

$$\frac{1}{M}\sum_{i=1}^{M}\|\hat{\boldsymbol{x}}_i - \boldsymbol{x}_i\|^2, \tag{4.7}$$

where $\boldsymbol{x}_i$ is the i^{th} realisation of $\boldsymbol{x}$. By substituting (4.3) into (4.7) one then can obtain the following cost function:

$$J(\boldsymbol{g}) = \frac{1}{M}\sum_{i=1}^{M}\|F_{-a}GF_a\boldsymbol{y}_i - \boldsymbol{x}_i\|^2 \tag{4.8}$$

4.1.2 Derivation of the Solution

The aim is now to minimize the cost function defined in (4.8) with respect to the vector $\boldsymbol{g}$ which is constrained to be real-valued in line with (4.4). Let,

$$\boldsymbol{z}_i = [z_{i,0} \dots\dots z_{i,N-1}]^T = F_a\boldsymbol{y}_i \,,$$

so that (4.8) becomes

$$J(\boldsymbol{g}) = \frac{1}{M}\sum_{i=1}^{M}\|F_{-a}G\boldsymbol{z}_i - \boldsymbol{x}_i\|^2 \tag{4.9}$$

$$= \frac{1}{M}\sum_{i=1}^{M}(F_{-a}G\boldsymbol{z}_i - \boldsymbol{x}_i)^H\,(F_{-a}G\boldsymbol{z}_i - \boldsymbol{x}_i)\,. \tag{4.10}$$

It can be observed that since G is a diagonal matrix then,

$$G\boldsymbol{z}_i = Z_i\boldsymbol{g}\,,$$

where $Z_{i(\text{NxN})}$ is a diagonal matrix such that $\boldsymbol{z}_i = diag(Z_i)$. Now (4.10) can be further simplified as:

$$J(\boldsymbol{g}) = \frac{1}{M}\sum_{i=1}^{M}(\overline{Z}_\iota \boldsymbol{g} - \boldsymbol{x}_i)^H (\overline{Z}_\iota \boldsymbol{g} - \boldsymbol{x}_i) , \tag{4.11}$$

where $\overline{Z}_{\iota(\text{NxN})}$ is equal to $F_{-a}Z_i$. Expanding (4.11) yields:

$$J(\boldsymbol{g}) = \frac{1}{M}\sum_{i=1}^{M}\left(\boldsymbol{g}^H \overline{Z}_\iota{}^H \overline{Z}_\iota \boldsymbol{g} - \boldsymbol{g}^H \overline{Z}_\iota{}^H \boldsymbol{x}_i - \boldsymbol{x}_i{}^H \overline{Z}_\iota \boldsymbol{g} + \boldsymbol{x}_i{}^H \boldsymbol{x}_i\right)$$

$$= \frac{1}{M}\sum_{i=1}^{M}\left(\boldsymbol{g}^H \overline{Z}_\iota{}^H \overline{Z}_\iota \boldsymbol{g} - (\boldsymbol{x}_i{}^H \overline{Z}_\iota \boldsymbol{g})^H - \boldsymbol{x}_i{}^H \overline{Z}_\iota \boldsymbol{g} + \boldsymbol{x}_i{}^H \boldsymbol{x}_i\right)$$

$$= \frac{1}{M}\sum_{i=1}^{M}\left(\boldsymbol{g}^H \overline{Z}_\iota{}^H \overline{Z}_\iota \boldsymbol{g} - 2Re(\boldsymbol{x}_i{}^H \overline{Z}_\iota \boldsymbol{g}) + \boldsymbol{x}_i{}^H \boldsymbol{x}_i\right),$$

since $\boldsymbol{g}$ is real-valued, the above equation becomes:

$$= \frac{1}{M}\sum_{i=1}^{M}\left(\boldsymbol{g}^T Q_i \boldsymbol{g} + \boldsymbol{b}_i{}^T \boldsymbol{g} + c_i\right) \quad , \tag{4.12}$$

where the matrix $Q_{i\ (\text{NxN})}$, the column vector $\boldsymbol{b}_i$, and the scalar c_i are:

$$Q_i = \overline{Z}_\iota{}^H \overline{Z}_\iota = (F_{-a}Z_i)^H (F_{-a}Z_i) = Z_i{}^H F_{-a}{}^H F_{-a} Z_i = Z_i{}^H Z_i ,$$

$$\boldsymbol{b}_i = (-2Re(\boldsymbol{x}_i{}^H \overline{Z}_\iota))^T = (-2Re(\boldsymbol{x}_i{}^H F_{-a} Z_i))^T ,$$

$$c_i = \boldsymbol{x}_i{}^H \boldsymbol{x}_i = \|\boldsymbol{x}_i\|^2 .$$

It can be observed that since Z_i is diagonal then Q_i is also diagonal as well as real-valued. Finally, (4.12) can be expressed as:

$$J(\boldsymbol{g}) = \boldsymbol{g}^T Q \boldsymbol{g} + \boldsymbol{b}^T \boldsymbol{g} + c , \tag{4.13}$$

where $Q = \frac{1}{M}\sum_{i=1}^{M} Q_i$, $\boldsymbol{b} = \frac{1}{M}\sum_{i=1}^{M} \boldsymbol{b}_i$, and $c = \frac{1}{M}\sum_{i=1}^{M} c_i$. To obtain the vector $\boldsymbol{g_o}$ that minimizes (4.13), the following equation must be solved:

$$\nabla_{\boldsymbol{g}} J(\boldsymbol{g})\big|_{\boldsymbol{g}=\boldsymbol{g_o}} = 0 \tag{4.14}$$

Where $\nabla_{\boldsymbol{g}} J(\boldsymbol{g}) = \begin{bmatrix} \frac{\partial J(\boldsymbol{g})}{\partial g_1} \\ \vdots \\ \frac{\partial J(\boldsymbol{g})}{\partial g_N} \end{bmatrix}_{N\times 1}$.

It can easily be confirmed that the derivative of the first term of (4.13) with respect to the vector $\boldsymbol{g}$ is in general equal to:

$$\nabla_{\boldsymbol{g}}\{\boldsymbol{g}^T Q\boldsymbol{g}\} = Q\boldsymbol{g} + Q^T\boldsymbol{g} \tag{4.15}$$

and since Q is diagonal the right-hand side becomes $2Q\boldsymbol{g}$. Similarly, the second term can be resolved as,

$$\nabla_{\boldsymbol{g}}\{\boldsymbol{b}^T\boldsymbol{g}\} = \boldsymbol{b} \tag{4.16}$$

Based on (4.15) and (4.16), (4.14) can be re-written as

$$2Q\boldsymbol{g_o} + \boldsymbol{b} = 0 \tag{4.17}$$

The system of *N* linear equations in *N* unknowns defined in (4.17) can then be solved to specify the designed filter's response $\boldsymbol{g_o}$ in the fractional frequency t_a. Of course, since Q is diagonal, it is trivial to find its inverse. However, the problem of finding the most suitable FrFT domain, namely the value of *a* which minimizes (4.8) is difficult to solve analytically. Instead, as in [10], an iterative approach in which $\boldsymbol{g_o}$ is consecutively computed for a finely sampled set of values over the entire range of *a,* is adopted here. The value of *a* which causes the smallest average error (4.7) is retained.

Reflecting on this presented solution, one can see that given a number of realizations of the desired signal $\boldsymbol{x}$ and their respective observations $\boldsymbol{y}_i$, the most appropriate T-F rotation as well as the corresponding multiplicative window can easily be determined. Furthermore, a distinct advantage of the presented derivation as compared to (4.5) is that it does not require knowledge of the noise statistics. Although the simple observation model of (4.1) was employed here, more generic assumptions for the distortion could equally be accommodated. For instance, if a multiplicative degradation of $\boldsymbol{x}$ is assumed as in [10], this will still be incorporated into $\boldsymbol{y}$, hence knowledge of the degradation process would also be unnecessary for the derivation of the solution, as in (4.17).

4.1.3 Experimental Results

In order to demonstrate the performance of the presented algorithm in Section 4.1.2, three illustrative examples are shown here. In each example, a set of thirty realizations of the desired signal along with their corresponding noisy observations are generated. Based on these, the most appropriate rotated domain and the associated window are established. The resulting filter is then applied to a previously unseen realization of the distorted signal. For the sake of comparison, this particular waveform is also filtered in the conventional frequency domain by fixing the order a to 1 and using the corresponding $\boldsymbol{g_o}$ to compute (4.3).

The first example, considers a Gaussian signal with randomized amplitude and time shift, i.e. $x(t) = Ae^{-\pi(t-s)^2}$, where A and s are random variables uniformly distributed in the interval [1, 3]. The noise component which was then added to corrupt the signal was generated as follows; white noise of finite duration between [-2, 2] was low-pass filtered (normalized cut-off frequency at 0.04), and subsequently modulated using the quadratic complex exponential (chirp) function $e^{-j2\pi t^2}$ in order to tilt the noise component in the T-F plane. A similar pair of signal and noise was also employed in [10]. The normalized MSE achieved for different values of a is plotted in Figure 4-1a where it can be seen that the most appropriate domain for filtering the type of signal at hand is the one at $a = 0.8$. The related fractional-frequency response of the filter is presented in Figure 4-1b. A realization of the desired signal $x(t)$ and the corresponding observed signal $y(t)$ are shown in Figure 4-2a and 4-2b. The resulting estimates $\hat{x}(t)$ after processing the depicted $y(t)$ with the proposed filter in the Fourier domain ($a = 1$) and the FrFT domain at $a = 0.8$ are shown in Figure 4-2c and 4-2d, respectively.

The desired signal in the second example is a linear chirp whose amplitude and time-shift are random variables, that is, $x(t) = Ae^{j4\pi(t-s)^2}$, where A and s are uniformly

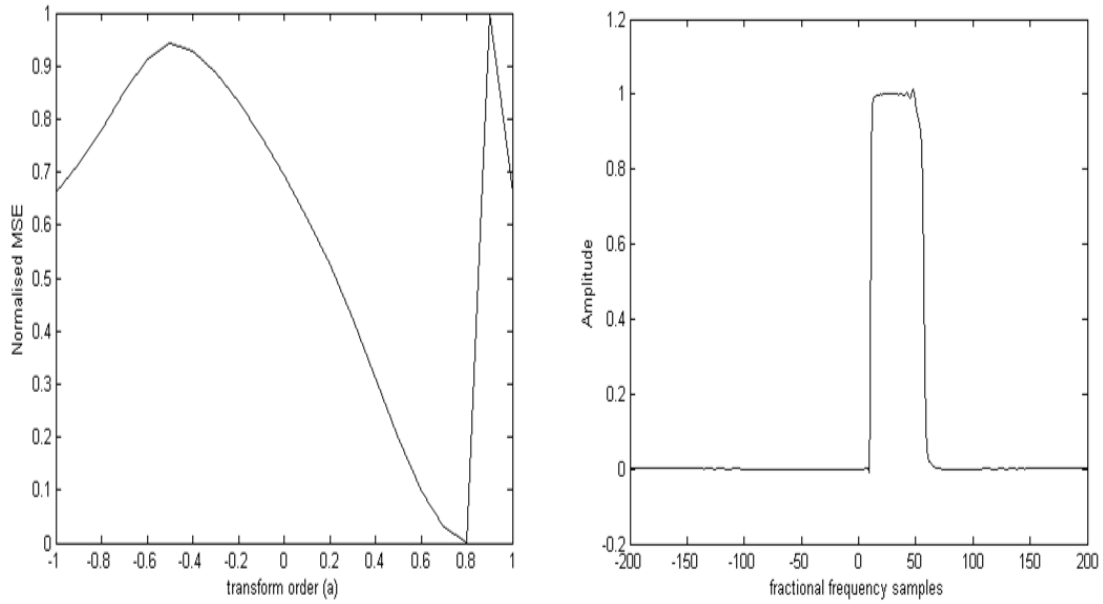

(a) (b)

Figure 4-1 *(a) Normalized MSE for different values of a, (b) Corresponding window* $\mathbf{g_o}$ *in the 0.8th domain.*

distributed on the intervals [1, 3] and [-0.1, 0.1], respectively. The interference consists of the sum of two different linear chirps of equal slopes, which can be defined as $Ae^{j2\pi(3(t-s)^2+5(t-s))} + Ae^{j2\pi(3(t-s)^2-5(t-s))}$. The sum of the desired signal and the interference is then quantized such that further distortion is added to it in the form of quantization noise. This can be expressed as $y(t) = \frac{\text{round}(\text{b}\, x_c(t))}{\text{b}}$, where $x_c(t)$ is the corrupted signal and *b* is the quantization factor which can be any positive integer. The lower the value of *b* the coarser the quantization effect, producing large rounding-off errors. In this example, *b* was set to the lowest value of 1. It should be stressed that this is a kind of distortion whose statistics is impossible to know in advance because it is a function of the input process. For such type of noise it is not feasible to collect a set of independent realizations either, therefore it cannot be dealt with using (4.5). The normalized MSE achieved for different values of *a* is depicted in Figure 4-3a where it can be seen that the most appropriate domain for filtering in this example is the one at *a = -0.7.*

The corresponding transfer function of the filter is presented in Figure 4-3b. A realization of the desired signal $x(t)$ and the corresponding corrupted signal $y(t)$ are

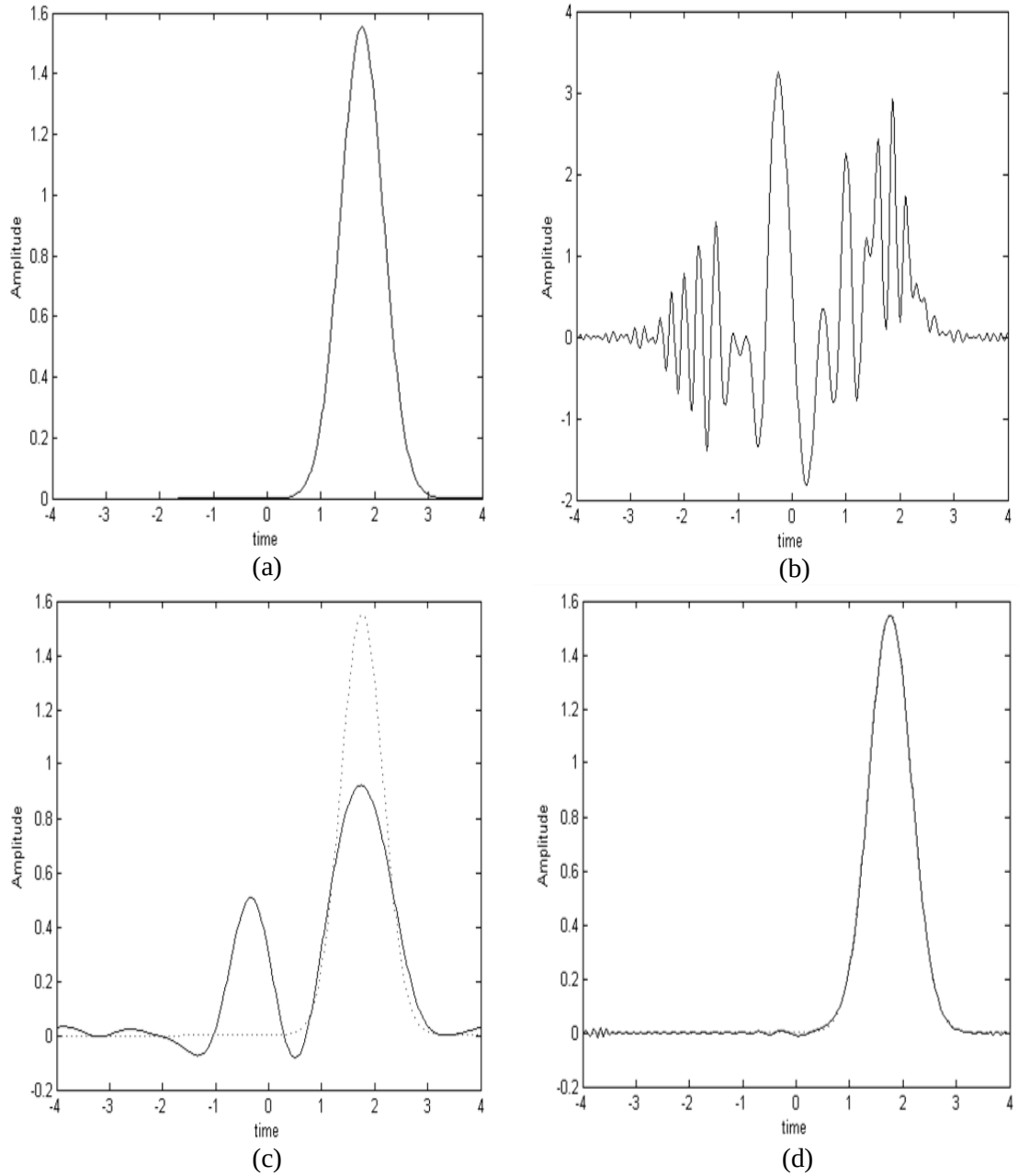

Figure 4-2 *(a) A realization of the desired signal $x(t)$, (b) Corresponding corrupted signal $y(t)$, (c) Estimate obtained by filtering in the Fourier (a = 1) domain (solid) and the desired signal (dotted), and (d) Estimate obtained by filtering in the a = 0.8th domain (solid) and the desired signal (dotted).*

depicted in Figure 4-4a and 4-4b. The results after filtering in the conventional frequency domain (*a = 1*), and the most suitable domain (*a = -0.7*) are shown in Figure 4-4c and 4-4d, respectively. It can be seen that a nearly perfect recovery of the desired signal can be achieved as a result of filtering in the specific FrFT domain.

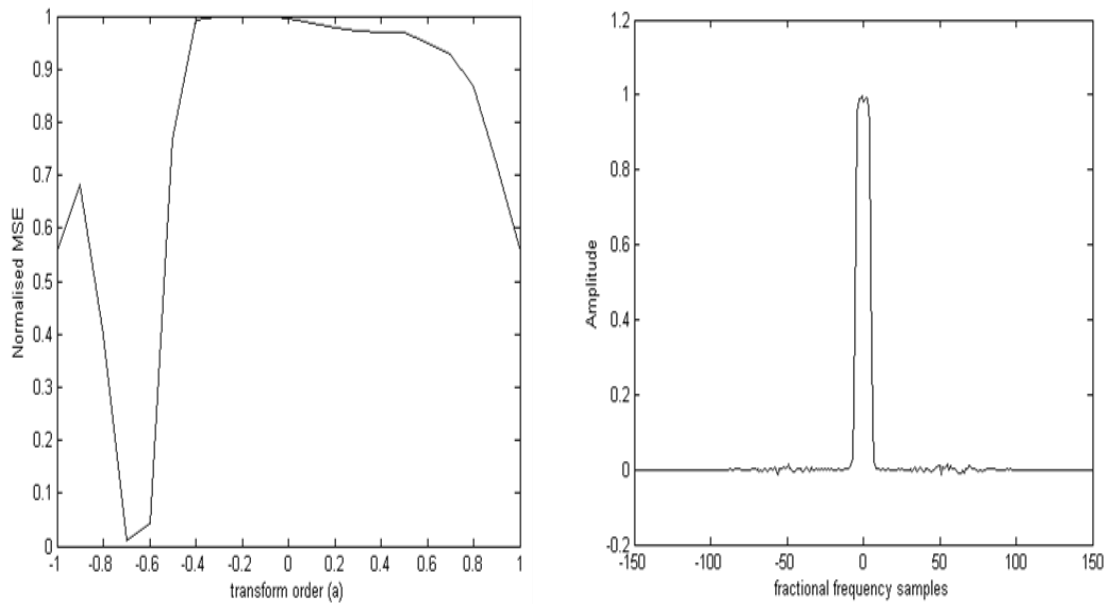

(a) (b)

Figure 4-3 *(a) Normalized MSE for different values of a, (b) Corresponding window* $\mathbf{g_o}$ *in the –* 0.7^{th} *domain.*

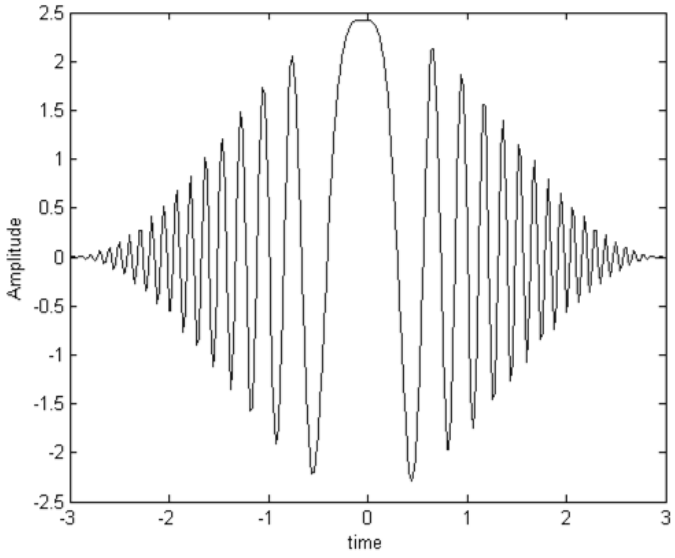

Figure 4-4a:

A realization of the desired signal $x(t)$.

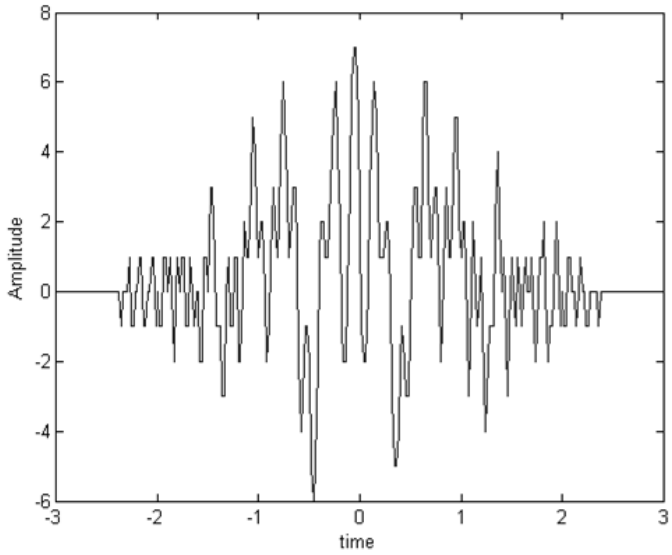

Figure 4-4b:

Corresponding corrupted signal $y(t)$.

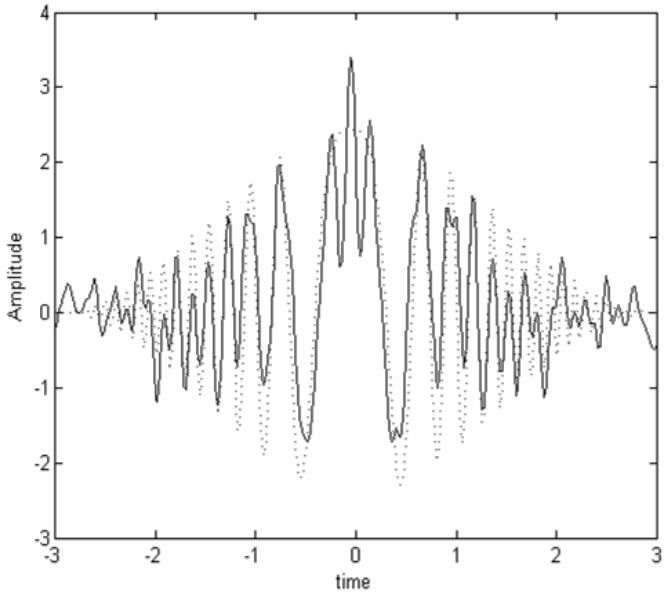

Figure 4-4c:

Estimate obtained by filtering in the Fourier (a = 1) domain (solid) and the desired signal (dotted).

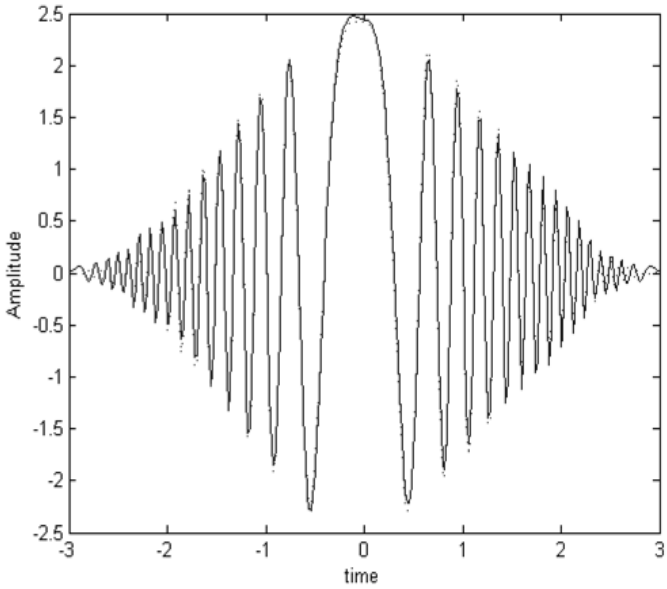

Figure 4-4d:

Estimate obtained by filtering in the a = -0.7th domain (solid) and the desired signal (dotted).

In the final example, the input process is now given as $x(t) = Ae^{j2\pi(3(t-s)^2+5(t-s))} + Ae^{j2\pi(3(t-s)^2-5(t-s))}$, which is degraded by the addition of zero-mean white Gaussian noise at 0dB SNR plus the signal $Ae^{j4\pi(t-s)^2}$, where *A* and *s* are uniformly distributed on the intervals [1, 3] and [-0.1, 0.1], respectively. The normalized MSE is presented for different values of *a* in Figure 4-5a. The minimum MSE was obtained in the *-0.6th* FrFT domain. The related window $\boldsymbol{g_o}$ in this domain is shown in Figure 4-5b. A realization of the desired signal $x(t)$ and the corresponding observed signal $y(t)$ are shown in Figure 4-6a and 4-6b. The estimate $\hat{x}(t)$ obtained by filtering the specific distorted signal of 4-6b in

the Fourier domain is shown in Figure 4-6c, whereas the result after filtering in the favorable domain (a = *-0.6*) is presented in 4-6d. Once again, it can be seen that, for certain types of signals, filtering in an appropriately rotated T-F domain can yield a superior performance as compared to that of conventional Fourier filters.

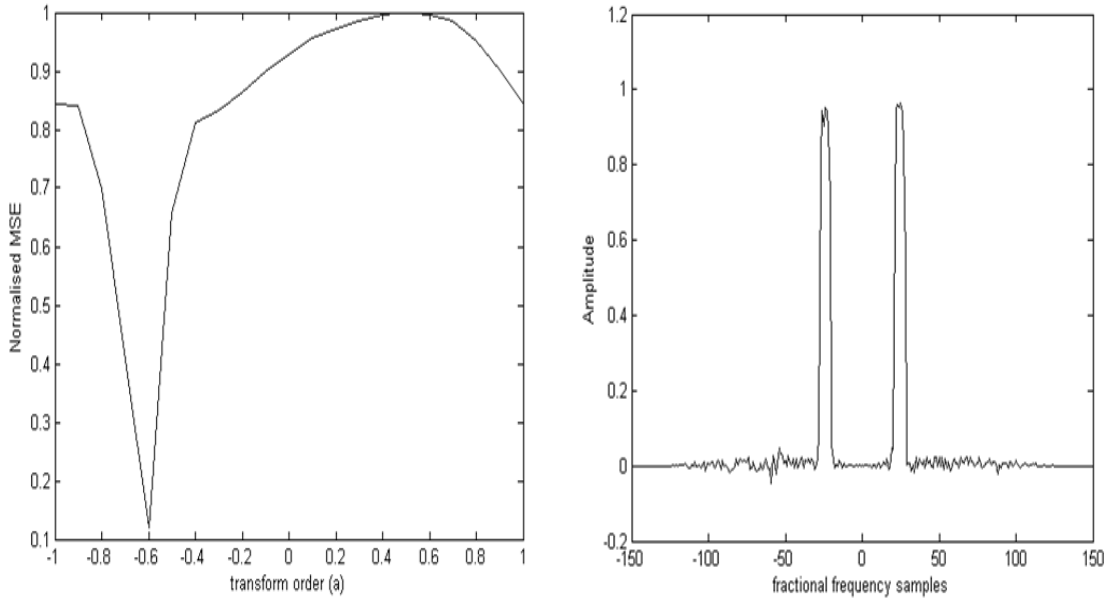

(a) (b)

Figure 4-5 *(a) Normalized MSE for different values of a, (b) Corresponding window* $\mathbf{g_o}$ *in the –* 0.6^{th} *domain.*

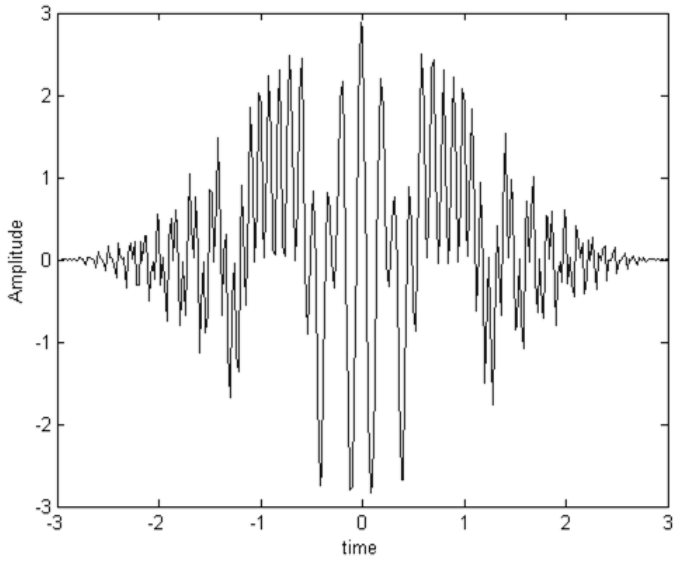

Figure 4-6a:

A realization of the desired signal $x(t)$.

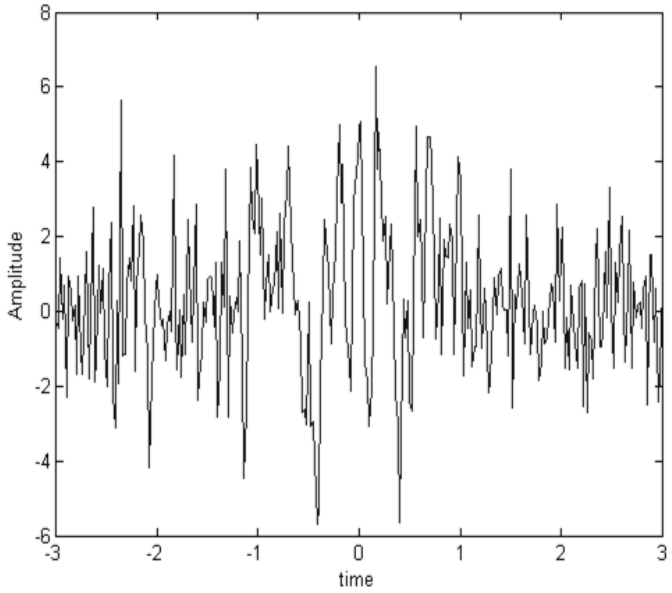

Figure 4-6b:

Corresponding corrupted signal $y(t)$.

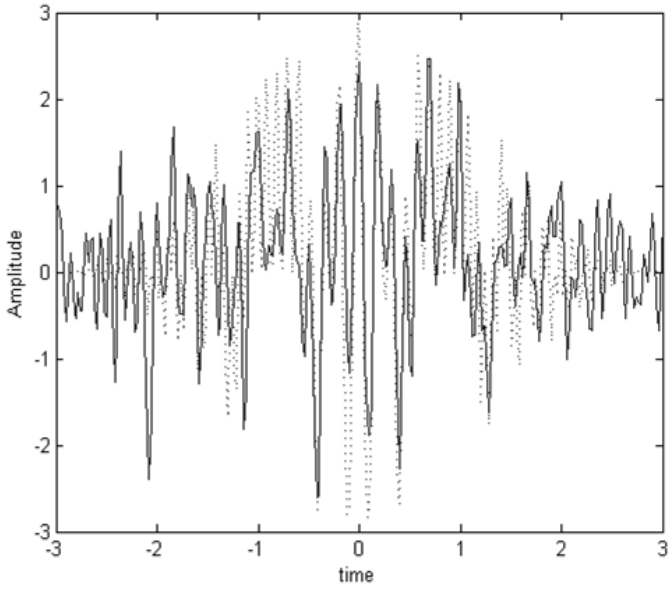

Figure 4-6c:

Estimate obtained by filtering in the Fourier (a = 1) domain (solid) and the desired signal (dotted).

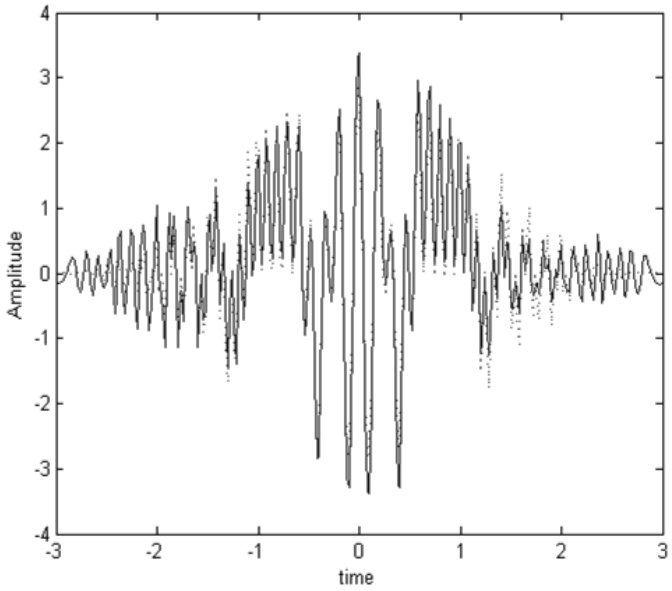

Figure 4-6d:

Estimate obtained by filtering in the a = -0.6th domain (solid) and the desired signal (dotted).

4.2 Summary/Key Contributions

In this chapter, an estimator resulting in an overall optimized pass band in the mean square sense, is thoroughly described. This proposed solution, as compared to the alternative solution of [10], reduces the number of parameters that are needed to be known and minimizes the relevant underlying assumptions. Specifically, the presented formulation does not require knowledge of the noise statistics or of any other degradation process, for that matter. This in turn may make it easier to apply the above filters in real-world signal processing problems.

Although this new proposed scheme has been restricted to operate in a single FrFT domain, it is actually possible to generalize the above formulation to include consecutive FrFT domains. However the challenges faced in optimizing such systems are non-trivial. In the following chapter, this problem is investigated and solutions that overcome these challenges are proposed.

References

[1] S. R. Subramaniam, B. W.-K. Ling, and A. Georgakis, "Filtering in rotated time-frequency domains with unknown noise statistics", IEEE Trans. Signal Process., vol. 60, no. 1, pp. 489 - 493, January 2012.

[2] J. B. Allen, "Short-Term Spectral Analysis, Synthesis, and Modification by Discrete Fourier-Transform," IEEE Transactions on Acoustics Speech and Signal Processing, vol. 25, pp. 235-238, 1977.

[3] G. F. Boudreaux-Bartels and T. W. Parks, "Time-Varying Filtering and Signal Estimation Using Wigner Distribution Synthesis Techniques," IEEE Trans. on Acoustics, Speech and Signal Processing, vol. ASSP-34,pp. 442-451, June 1986.

[4] F. Hlawatsch, W. Kozek, and W. Krattenthaler, "Time-Frequency Subspaces and Their Application to Time-Varying Filtering," in IEEE ICASSP Proceedings, pp. 1607-1610, 1990.

[5] F. Hlawatsch and W. Kozek, "Time-Frequency Projection Filters and Time-Frequency Signal Expansions," IEEE Transactions on Signal Processing, vol. 42, pp. 3321-3334, December 1994.

[6] L. B. Almeida, "The fractional Fourier transform and time-frequency representations," IEEE Trans. Signal Processing, vol. 42, pp.3084-3091, Nov. 1994.

[7] B. A. Weisburn and T. W. Parks, "Design of Time Frequency Strip Filters," in 29th Annual Asilomar Conf. on Signals, Systems and Computers, Oct. 29 1995.

[8] B. A. Weisburn and R.G. Shenoy, "Time-frequency strip filters," in IEEE ICASSP Proceedings, vol.3, no., pp.1411-1414, 7-10 May 1996.

[9] H. M. Ozaktas, B. Barshan, D. Mendlovic, and L. Onural, "Convolution, filtering, and multiplexing in fractional Fourier domains and their relation to chirp and wavelet transforms," J. Opt. Soc. Amer. A., vol. 11, pp. 547-559, 1994.

[10]M. A. Kutay, H.M. Ozaktas, O. Arikan, and L. Onural, "Optimal filtering in fractional Fourier domains," IEEE Trans. Signal Process., vol. 45, no. 5, pp. 1129-1143, May 1997.

Chapter 5

Successive Signal Modifications in the TF Plane

Based on the concept of time-frequency rotation, one can implement linear time-varying operators which could prove useful in a range of signal processing applications. It has been shown, that restoration of certain types of signals can be improved substantially by filtering in fractional domains. It has further been revealed that involving more than one domain in the filtering process can potentially outperform single-stage modifications. In this chapter, the problem of optimally designing such schemes to operate in both the conventional and fractional Fourier domains, are explored respectively. Parts of the work described in this chapter have been reported in [1].

Introduction

As shown in Chapter 3, operating successively in different domains may lead to significant performance advantages as compared to single-stage modifications. To fully appreciate the potential benefits of such a scheme, one can consider the simple example of Figure 5-1 where two distinct signal elements submerged in noise are depicted in the joint time-frequency plane. It can be observed that, in this case, a Fourier filter alone will have to remove a significant amount of noise still residing within the horizontal strip defined by the filter's cut-off thresholds. On the contrary, the combined effect of a frequency filter cascaded with the time window can better isolate the desired signal. Clearly, the resulting overall system faces a higher signal-to-noise (SNR) ratio inside its pass band and is therefore in a more favorable position to suppress the interference component.

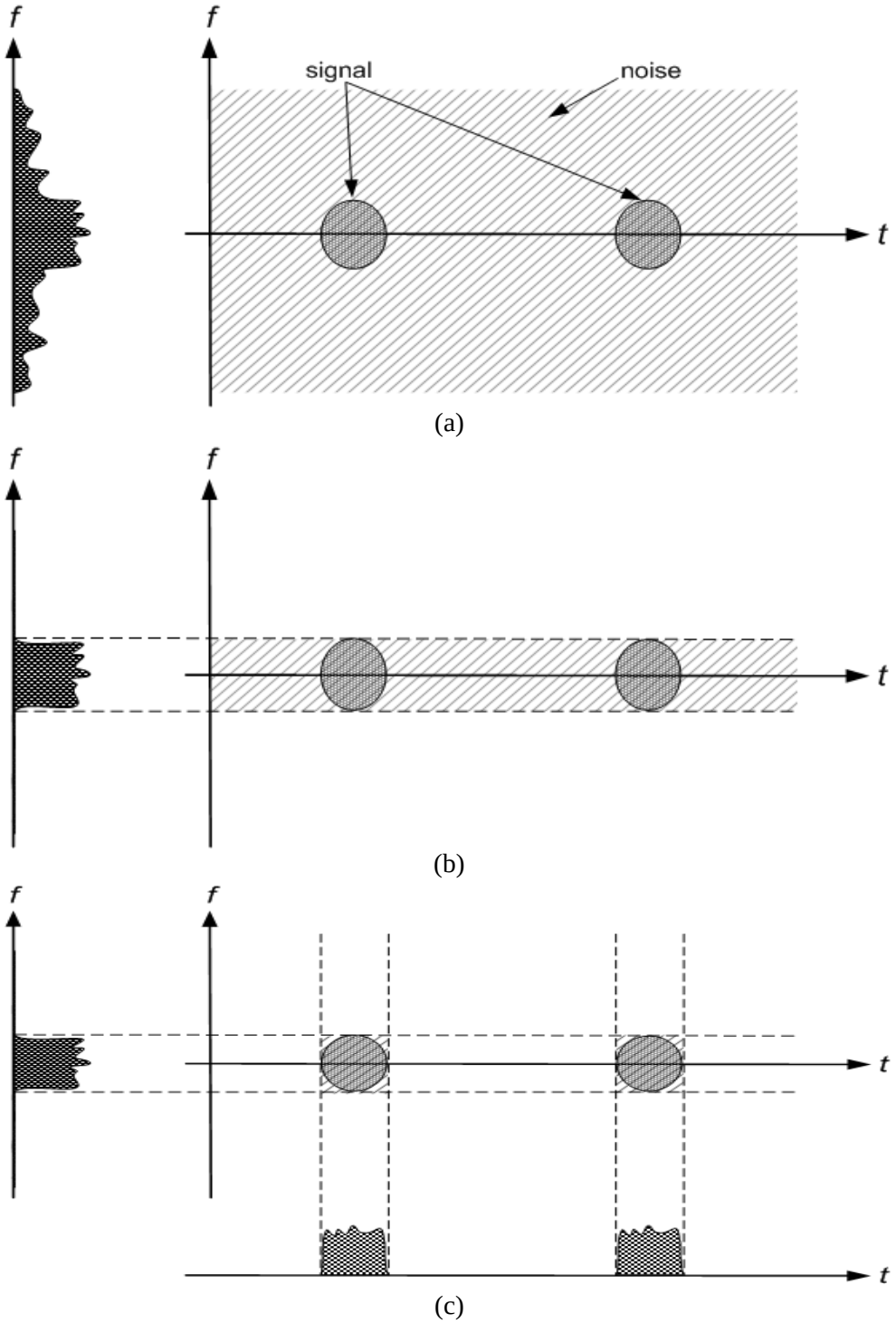

Figure 5-1 *Joint time-frequency visualization of: (a) an assumed signal with two distinct elements embedded in noise; (b) a low-pass filtered version of the signal, and (c) the signal after its successive modifications by a frequency filter and a time window.*

Although the above has only been illustrated using conventional Fourier domains, this concept is completely analogous when extended into fractional domains as well. Furthermore, based on previous discussions regarding the advantages of generalizing

Fourier-domain concepts in the fractional Fourier transform case, one can also expect significant improvements to be attainable here as well. Similar conclusions were also reported in [2]. However, optimizing such cascaded configurations, either in the conventional or fractional Fourier domains has proven to be quite a challenging task, as it will be exposed in the following sub-sections.

5.1 Repeated Signal Modifications in Conventional Fourier Domains

Our aim is to optimally recover a signal in the mean square error sense, operating in the frequency domain. To illustrate this, the same observation model and optimality criterion defined in (4.1) and (4.2) shall be used. It is easy to show that due to Parseval's relation, (4.2) can also be expressed as:

$$\text{mse}(\widehat{\mathbf{X}}) = \frac{1}{\text{N}}\text{E}[\left\|\widehat{\mathbf{X}} - \mathbf{X}\right\|^2], \tag{5.1}$$

where $\widehat{\mathbf{X}}$ is the Fourier transform of $\hat{\mathbf{x}}$, i.e. $\widehat{\mathbf{X}} = F\,\hat{\mathbf{x}}$, with F being the DFT matrix. For the common setting depicted in Figure 5-2a it holds that:

$$\widehat{\mathbf{X}} = \Lambda \boldsymbol{Y}, \tag{5.2}$$

where $\mathbf{Y} = F\boldsymbol{y}$, and Λ is a diagonal matrix whose non-zero elements $(h_0,h_1,\ldots,h_{N-1})$ form the frequency response of the filter. Thus, by minimising (5.1) with respect to $(h_0,h_1,\ldots,h_{N-1})$ the N components of the optimized frequency response can be determined as [3]:

$$h_{\text{opt,i}} = \frac{\text{E}[\text{X(i)Y}^*\text{(i)}]}{\text{E}[\text{Y(i)Y}^*\text{(i)}]} \qquad i = 0,1,\ldots,N-1\,. \tag{5.3}$$

Moreover, under the assumption that the noise is independent of the input process and has zero mean, (5.3) can be further expressed as:

$$h_{opt,i} = \frac{E\left[|X[i]|^2\right]}{E[|X[i]|^2]+E[|N[i]|^2]}\,, \tag{5.4}$$

which represents the ensemble average energy density of the signal at the frequency sample i, divided by the sum of the ensemble averages of the energy densities of the signal and noise at the same frequency sample. This is completely analogous to the process

described in (4.6). This system can further be extended to incorporate two domains, such as described alongside Figure 5-1.

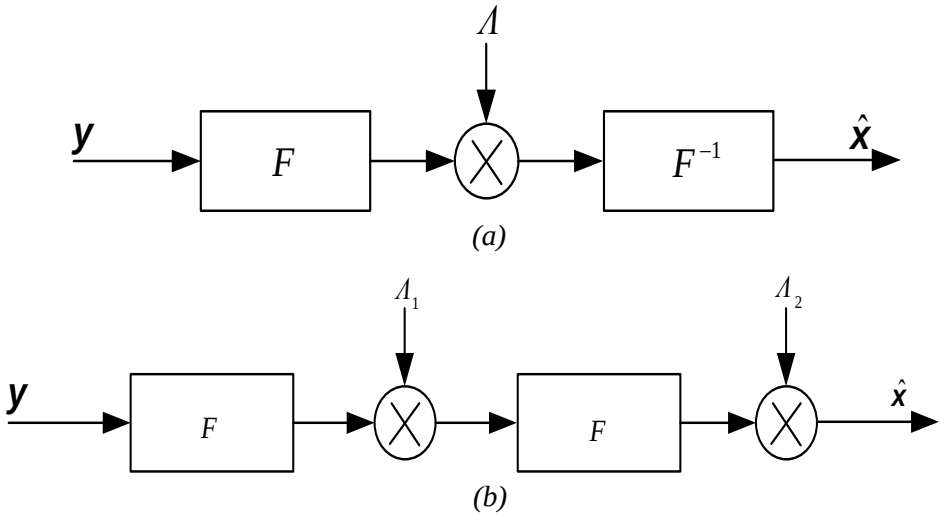

Figure 5-2 *(a) Block diagram of a single-stage filter, (b) Block diagram of the two-stage filtering approach.*

Thus, the cascaded system configuration shown in Figure 5-2b will have to be considered, whereby the estimate $\hat{\mathbf{x}}$ is now equal to:

$$\hat{\mathbf{x}} = \Lambda_2 F \Lambda_1 F \boldsymbol{y} \,, \tag{5.5}$$

where

$$\Lambda_k = \begin{bmatrix} h_{k,1} & 0 & \cdots & 0 & 0 \\ 0 & & & & 0 \\ \vdots & & \ddots & & \vdots \\ 0 & & & & 0 \\ 0 & 0 & \cdots & 0 & h_{k,N} \end{bmatrix}, \qquad k=1, 2$$

with $\boldsymbol{h_k} = diag(\Lambda_k)$, i.e. $\boldsymbol{h_1} = (h_{1,0}, h_{1,1}, \ldots, h_{1,N-1})$ and $\boldsymbol{h_2} = (h_{2,0}, h_{2,1}, \ldots, h_{2,N-1})$, being the frequency response of the filter and the window function, respectively. The objective is then to determine the optimized $\boldsymbol{h_1}$ and $\boldsymbol{h_2}$ which minimises (4.2). However it can be observed from (5.5) that, the relationship between the estimate $\hat{\mathbf{x}}$ and the filtering functions seems to be highly non-linear. As a result, it becomes very challenging to obtain an analytic solution for the filters. A usual approach in such optimisation problems is to adopt an iterative procedure in which one function is optimised at a time by keeping the other fixed to its values obtained during the preceding iteration. Such an approach has also been

followed in [4] and is briefly summarised in the following paragraphs.

At the beginning, both the diagonal matrices Λ_1 and Λ_2 are initialized to identity matrices. Then, starting with the first function $\boldsymbol{h_1}$, an estimate for its optimum expression can be calculated based on (5.3). In the second iteration, the preliminary solution for $\boldsymbol{h_1}$ is used to obtain an initial estimate of the optimum $\boldsymbol{h_2}$. Thus, (5.5) can be written as $\hat{\mathbf{x}} = A\Lambda_2 B\boldsymbol{y}$, where $A = I$ (the identity matrix) and $B = F\Lambda_1 F$. Minimising (4.2) with respect to $\boldsymbol{h_2}$ yields [4]:

$$\boldsymbol{h_2} = D^{-1}\boldsymbol{c} \ , \tag{5.6}$$

where $D = (A^H A) * \left(BR_{yy}B^H\right)^T$, and '*' denotes the element-wise multiplication between two matrices, whereas $\boldsymbol{c} = diag\left(A^H R_{xy} B^H\right)$. Also, $R_{xy} = E[\boldsymbol{xy}^H]$ and $R_{yy} = E[\boldsymbol{yy}^H]$ are correlation matrices, which under the assumption of the noise being independent of the ideal signal can also be obtained as $R_{xy} = R_{xx}$ and $R_{yy} = R_{xx} + R_{nn}$.

The third iteration focuses back on $\boldsymbol{h_1}$ with (5.5) now expressed as $\hat{\mathbf{x}} = A\Lambda_1 B\boldsymbol{y}$, where $A = \Lambda_2 F$ and $B = F$. By minimising (4.2) with respect to $\boldsymbol{h_1}$, the solution is obtained similarly to (5.6), i.e. $\boldsymbol{h_1} = D^{-1}\boldsymbol{c}$, with D and $\boldsymbol{c}$ having the same structure as before. The above steps are repeated with $\boldsymbol{h_1}$ and $\boldsymbol{h_2}$ being updated accordingly at each iteration. Once the solutions converge the iterations stop. This procedure is further summarized in a flow-chart form, which is depicted in Figure 5-3.

5.1.1 Experimental Results

To examine its performance, this proposed method is again applied in the area of ultrasound elastography [1]. The tissue displacement data that is used in the following experiments are those mentioned in Section 3.1.2. However, this time the denoising scheme is applied in the 1st derivative domain (i.e. on the Strain signal). Furthermore, the level of noise added to the input process is even more substantial as compared to the

previous example in Section 3.1.2. Specifically, -16.28dB SNRst (where SNRst is the equivalent signal-to-noise ratio in the strain signal), is added to the ideal signal. Both the ideal and corrupted elastograms are depicted in Figure 5-4 (a) and (b), respectively. Once more, it can be observed how severely the differentiation process amplifies the amount of noise and degrades the strain profiles.

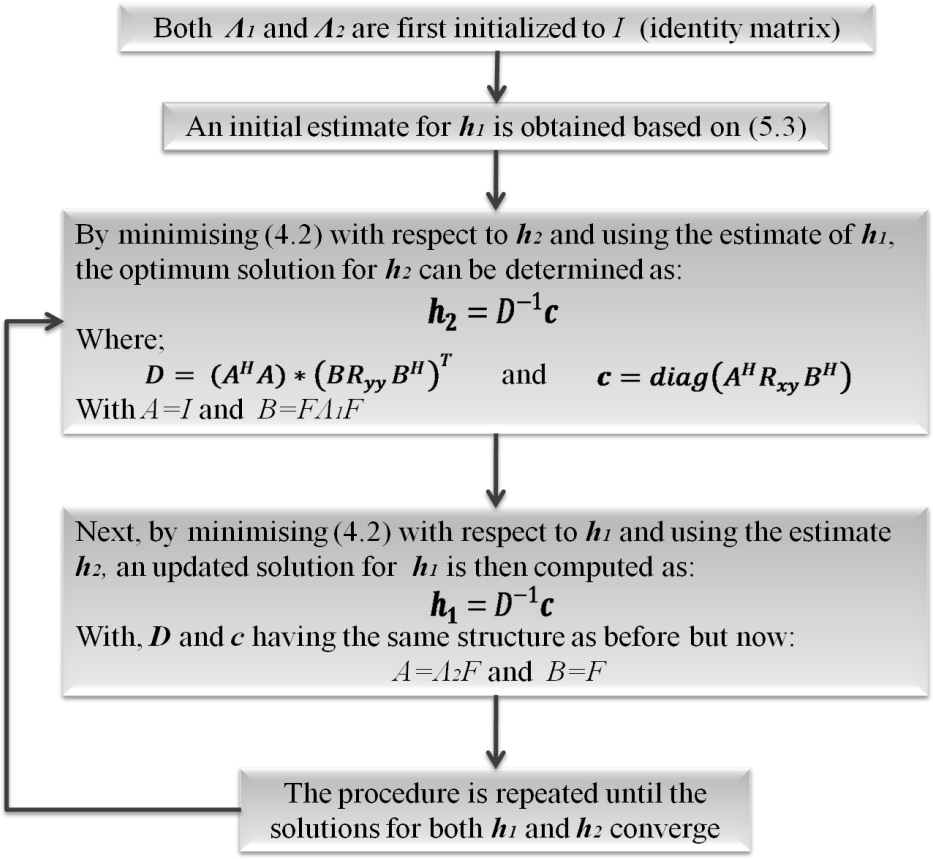

Figure 5-3 *A flow-chart to illustrate the iterative procedure involved in solving for the optimized filters described in (5.5).*

To illustrate the performance advantages that this method may have over a simple single-stage Fourier filter, presented in Figure 5-2a, the best-case scenarios for both filters is compared, i.e. by assuming the statistics of the ideal signal and the noise to be known, one can inspect what is the optimum result that can be achieved by each of the two methods. The denoised result of the single-stage optimized filter (Figure 5-2a) is presented in Figure 5-4c, whereas the result based on the application of the two-stage scheme (Figure 5-2b) is shown in Figure 5-4d. It is clear that the second method yields a much more

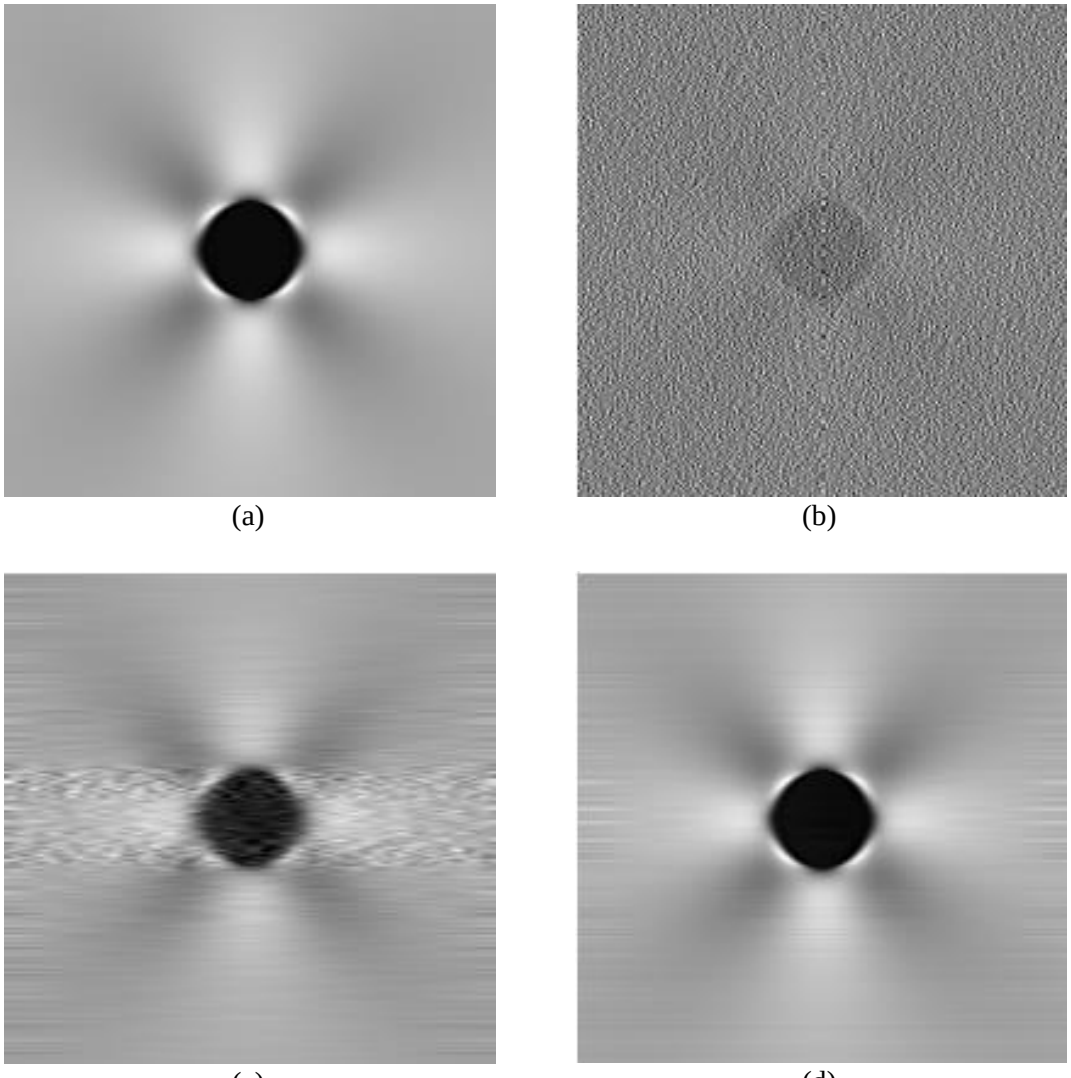

(a) (b)

(c) (d)

Figure 5-4 *(a) Simulation of ideal elastogram, and (b) corrupted elastogram (SNR= –16.28dB). Recovered elastogram after denoising with: (c) the single-stage (frequency) optimized filter, and (d) the optimized two-stage (frequency-time) system.*

accurate estimate of the ideal elastogram. The contrast-to-noise ratio (CNRe) detailed in Section 3.1.2, is again used to evaluate the quality of the achieved elastogram.

Along with the single-stage Fourier filter and the two-stage filtering system described above, two other recently proposed methods have been included in the conducted experiments. The FrFT-based denoising method (as described in Section 3.1.2) and the masked STFT scheme described in [5] were applied to the same noisy realization of the simulated elastogram that was used for all the presented results. The parameters required for the latter two methods were determined empirically as it was done in Section 3.1.1 and

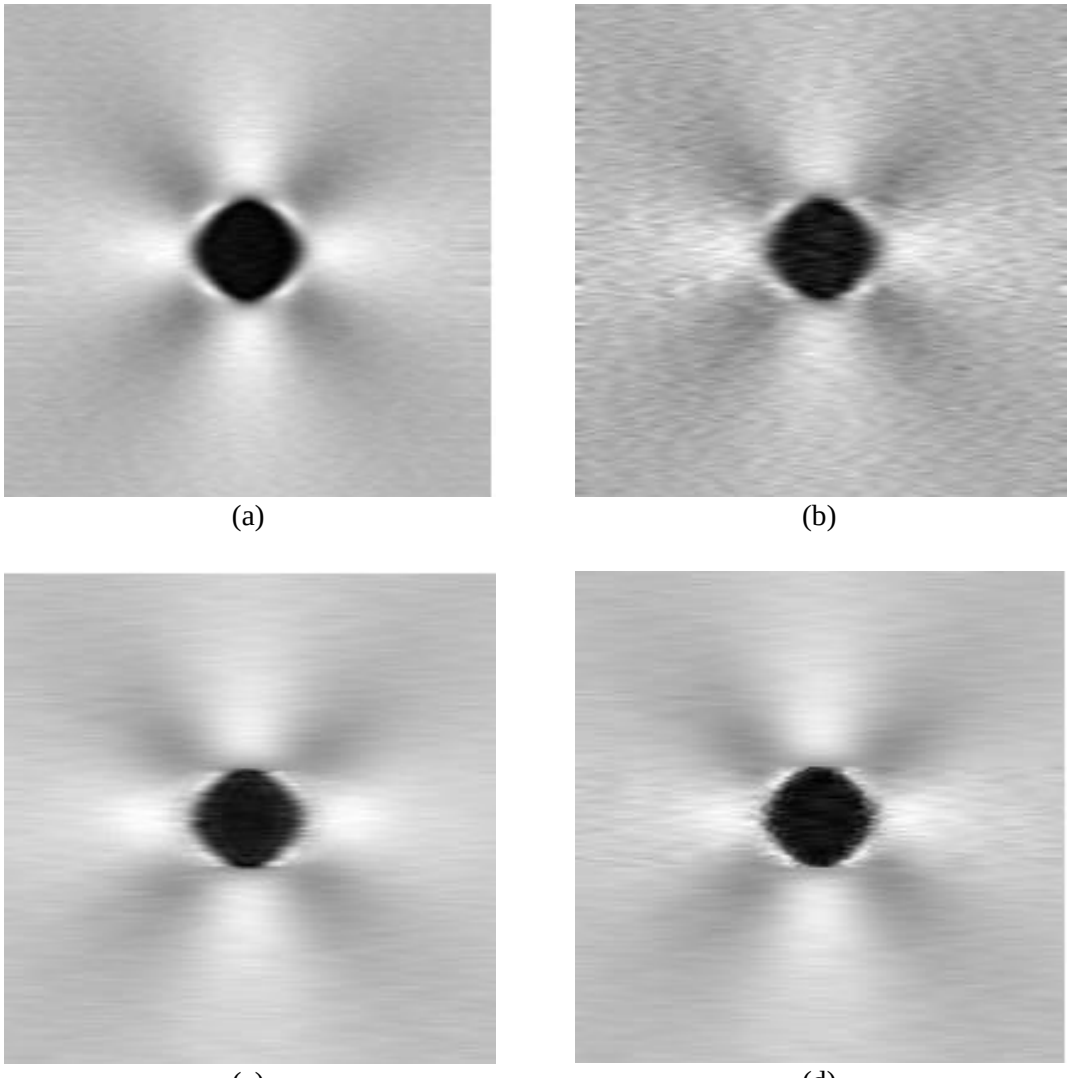

(a) (b)

(c) (d)

Figure 5-5 *Calculated elastogram after denoising with: (a) the two-stage (frequency-time) filter, (b) the single-stage (frequency) filter, (c) the FrFT-based filter, and (d) the masked STFT method.*

[5], respectively. For the given realization, the FrFT-based method achieved a CNR_e value of 65.69dB whereas the masked STFT approach resulted in a value of 60.60dB.

The resulting elastograms are shown in Figure 5-5c and Figure 5-5d, while the axial strains corresponding to the central slices of the filtered elastograms are compared in Figure 5-6c and Figure 5-6d. Both equations (5.4) and (5.6) refer to averages obtained from ensembles of realizations of the ideal and noise processes. In a real-world experiment these would not be available and therefore need to be estimated. In this work, the simulated elastogram was treated as an experimental measurement therefore assuming that the ideal

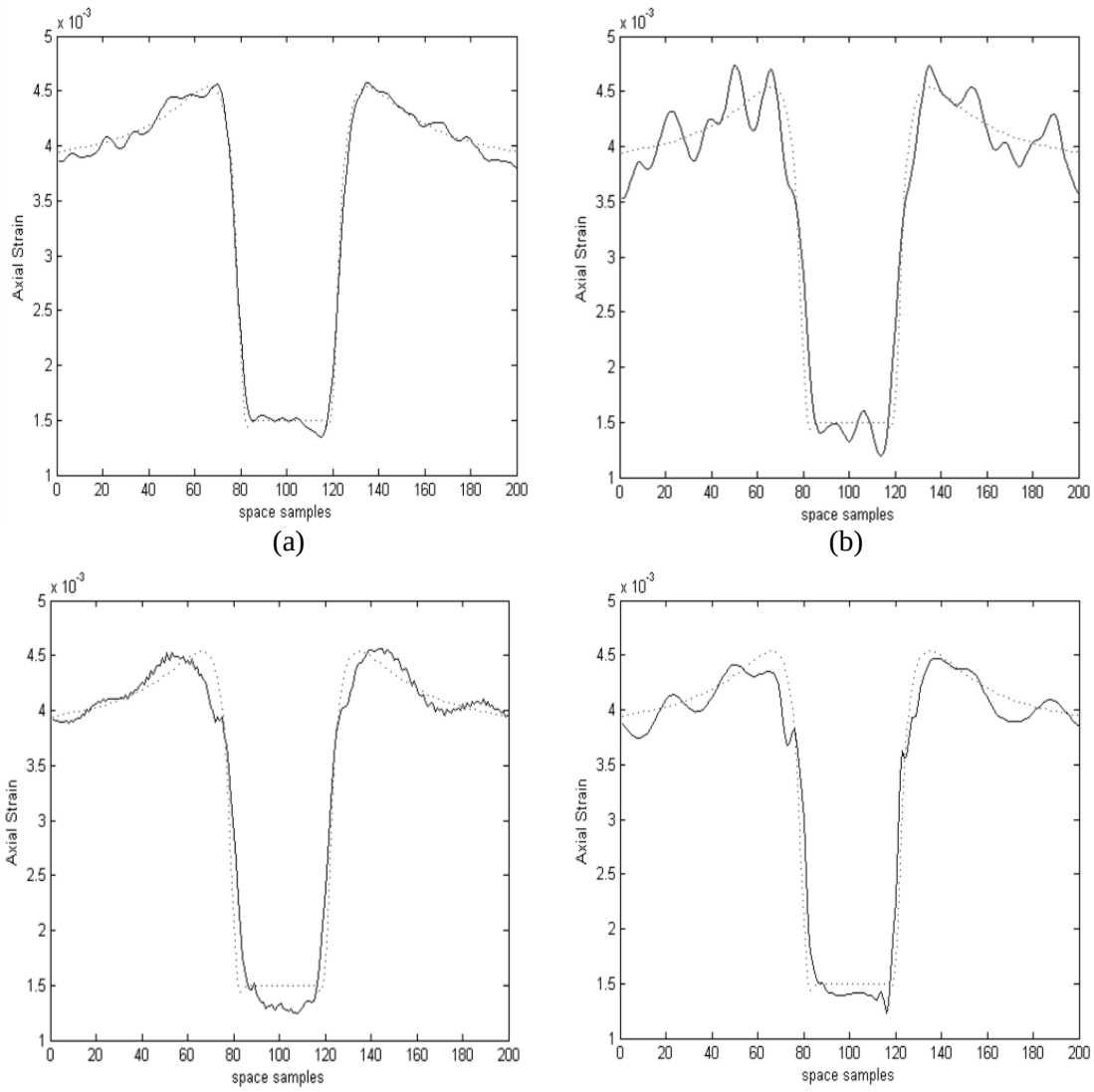

Figure 5-6 *Axial strain slices (solid lines) taken along the center of the resulting elastogram after denoising with: (a) the two-stage filter, (b) the single-stage filter, (c) the FrFT-based filter, and (d) the masked STFT method. The reference axial strain is also shown (dotted line).*

signal is unknown. Instead, a number of estimates of the ideal process were generated by low-pass filtering simulated noisy elastograms at different cut-off frequencies. The simulated noisy elastograms could represent repeated ultrasonic measurements of the same tissue area under varied compression levels. The noise ensemble was created by generating a number of noise realizations and then taking their first derivative. In the clinical lab, this could be replaced by a few measurements of healthy-tissue displacements, which would then be differentiated, with their offset being subsequently removed.

Based on the above sets, estimates of the correlations R_{xx} and R_{nn} were obtained and used for the derivation of the multiplicative filtering functions defined in both (5.2) and (5.5), respectively. The two-stage scheme resulted in a CNR_e value of 66.93dB whereas the single-stage filter achieved a lower ratio of 49.08dB. The resulting elastograms are shown in Figure 5-5a and Figure 5-5b. The central slices of the filtered elastograms are compared in Figure 5-6a and Figure 5-6b. Thus, it can be seen that by including an additional domain in the optimization process, one can significantly improve the quality of the obtained results.

5.1.2 Optimized Estimator with Unknown Noise Models

The method described in Section 5.1 has a major disadvantage. This is that in order to obtain the filter profiles as indicated in (5.6) the statistics of the noise must be known. However, the statistical model of the corrupting noise in many areas of application may be unknown. Hence, this requirement severely restricts the applicability of such methods in a multitude of signal processing problems. In this section, an alternative solution to compensate for this shortcoming is introduced. The presented formulation draws upon a similar concept of derivation as in Section 4.1.2.

The configuration of this new alternative system is shown in Figure 5-7. Essentially, it is still based on the series interconnection of a frequency filter and a time window, similar to Figure 5-2b. The signal is first passed through a linear time-invariant filter. The result is then multiplied with an appropriate time window. Since the input to the time window depends on the output of the filter, the two components cannot be designed independently. Thus they are designed together such that the overall system operates optimally in the mean square error sense. In the next few paragraphs, the approach in which their joint optimization is implemented will be described.

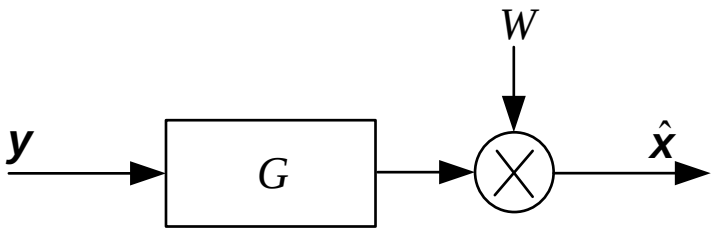

Figure 5-7 *Proposed system configuration.*

Similar to the argument provided in Section 4.1.1, an alternative route to the filter design problem is taken by estimating (4.2) with the average error over *M* realisations,

$$\frac{1}{M}\sum_{i=1}^{M}\|\widehat{\boldsymbol{x}}_i - \boldsymbol{x}_i\|^2, \tag{5.7}$$

where $\boldsymbol{x}_i$ is the i^{th} realisation of $\boldsymbol{x}$. Further, based on the filter circuit of Figure 5-7, the estimate $\widehat{\boldsymbol{x}}$ can be obtained as:

$$\widehat{\boldsymbol{x}} = WF_{-1}GF\boldsymbol{y}\,, \tag{5.8}$$

where $F_{\text{(NxN)}}$ and $F_{-1\text{(NxN)}}$ are the discrete Fourier transform (DFT) matrices which correspond to the Fourier transform and inverse Fourier transform, respectively; $G_{\text{(NxN)}}$ and $W_{\text{(NxN)}}$ are diagonal matrices whose elements are composed of the filter's frequency response $\boldsymbol{g}$ and time window samples $\boldsymbol{w}$, respectively. That is, $\boldsymbol{g} = diag(G) = (g_0, \dots, g_{N-1})$ and $\boldsymbol{w} = diag(W) = (w_0, \dots, w_{N-1})$. The objective is then to determine the vector pair $\boldsymbol{g_{opt}}$ and $\boldsymbol{w_{opt}}$ that minimises (5.7). Additionally, both $\boldsymbol{g_{opt}}$ and $\boldsymbol{w_{opt}}$ is considered to be real-valued.

By substituting (5.8) into (5.7) the following cost function can then be obtained:

$$J(\boldsymbol{g},\boldsymbol{w}) = \frac{1}{M}\sum_{i=1}^{M}\|WF_{-1}GF\boldsymbol{y}_i - \boldsymbol{x}_i\|^2 \tag{5.9}$$

Let,

$$\boldsymbol{a}_i = [a_{i,0} \dots \dots\ a_{i,N-1}]^T = F\boldsymbol{y}_i\,,$$

so that (5.9) becomes

$$\begin{aligned} J(\boldsymbol{g},\boldsymbol{w}) &= \frac{1}{M}\sum_{i=1}^{M}\|WF_{-1}G\boldsymbol{a}_i - \boldsymbol{x}_i\|^2 \\ &= \frac{1}{M}\sum_{i=1}^{M}(WF_{-1}G\boldsymbol{a}_i - \boldsymbol{x}_i)^H\,(WF_{-1}G\boldsymbol{a}_i - \boldsymbol{x}_i) \end{aligned} \tag{5.10}$$

It can be observed that since G is a diagonal matrix then,

$$G\boldsymbol{a}_i = A_i\boldsymbol{g} \ ,$$

where $A_{i\text{(NxN)}}$ is a diagonal matrix such that $\boldsymbol{a}_i = diag(A_i)$. Now (5.10) can be further simplified as:

$$J(\boldsymbol{g},\boldsymbol{w}) = \frac{1}{M}\sum_{i=1}^{M}(W\bar{A}_\iota\boldsymbol{g} - \boldsymbol{x}_i)^H\,(W\bar{A}_\iota\boldsymbol{g} - \boldsymbol{x}_i) \tag{5.11}$$

where $\bar{A}_{\iota\text{(NxN)}}$ is equal to $F_{-1}A_i$. Expanding (5.11) yields:

$$J(\boldsymbol{g},\boldsymbol{w}) = \frac{1}{M}\sum_{i=1}^{M}(\boldsymbol{g}^H\bar{A}_\iota{}^H W^H W\bar{A}_\iota\boldsymbol{g} - \boldsymbol{g}^H\bar{A}_\iota{}^H W^H\boldsymbol{x}_i -$$

$$\boldsymbol{x}_i{}^H W\bar{A}_\iota\boldsymbol{g} + \boldsymbol{x}_i{}^H\boldsymbol{x}_i)$$

$$= \frac{1}{M}\sum_{i=1}^{M}(\boldsymbol{g}^H\bar{A}_\iota{}^H W^H W\bar{A}_\iota\boldsymbol{g} - (\boldsymbol{x}_i{}^H W\bar{A}_\iota\boldsymbol{g})^H -$$

$$\boldsymbol{x}_i{}^H W\bar{A}_\iota\boldsymbol{g} + \boldsymbol{x}_i{}^H\boldsymbol{x}_i)$$

$$= \frac{1}{M}\sum_{i=1}^{M}\left(\boldsymbol{g}^H\bar{A}_\iota{}^H W^H W\bar{A}_\iota\boldsymbol{g} - 2Re(\boldsymbol{x}_i{}^H W\bar{A}_\iota\boldsymbol{g}) + \boldsymbol{x}_i{}^H\boldsymbol{x}_i\right),$$

since $\boldsymbol{g}$ and $\boldsymbol{w}$ are real-valued, the above equation becomes:

$$= \frac{1}{M}\sum_{i=1}^{M}\left(\boldsymbol{g}^T Q_{w,i}\boldsymbol{g} + \boldsymbol{b}_{w,i}{}^T\boldsymbol{g} + c_i\right) \tag{5.12}$$

where the matrix $Q_{w,i\ \text{(NxN)}}$, the column vector $\boldsymbol{b}_{w,i}$, and the scalar c_i are:

$$Q_{w,i} = \bar{A}_\iota{}^H W^H W\bar{A}_\iota = \bar{A}_\iota{}^H WW\bar{A}_\iota \ ,$$

$$\boldsymbol{b}_{w,i} = (-2Re(\boldsymbol{x}_i{}^H W\bar{A}_\iota))^T \ ,$$

$$c_i = \boldsymbol{x}_i{}^H\boldsymbol{x}_i = \|\boldsymbol{x}_i\|^2 \ .$$

Finally, (5.12) can be expressed as:

$$J(\boldsymbol{g},\boldsymbol{w}) = \boldsymbol{g}^T Q_w\boldsymbol{g} + \boldsymbol{b}_w{}^T\boldsymbol{g} + c \ , \tag{5.13}$$

where $Q_w = \frac{1}{M}\sum_{i=1}^{M} Q_{w,i}$, $\boldsymbol{b}_w = \frac{1}{M}\sum_{i=1}^{M}\boldsymbol{b}_{w,i}$, and $c = \frac{1}{M}\sum_{i=1}^{M} c_i$. To obtain the vector $\boldsymbol{g_o}$ that minimizes (5.13), the following equation must be solved:

$$\nabla_{\boldsymbol{g}} J(\boldsymbol{g},\boldsymbol{w})\big|_{\boldsymbol{g}=\boldsymbol{g_o}} = 0 \ . \tag{5.14}$$

As in Section 4.1.2, the derivative of the first term of (5.13) with respect to the vector $\boldsymbol{g}$ is equal to:

$$\nabla_{\boldsymbol{g}}\{\boldsymbol{g}^T Q_w \boldsymbol{g}\} = Q_w \boldsymbol{g} + {Q_w}^T \boldsymbol{g}, \tag{5.15}$$

Likewise, the second term can be expressed as,

$$\nabla_{\boldsymbol{g}}\{{\boldsymbol{b}_w}^T \boldsymbol{g}\} = \boldsymbol{b}_w \, . \tag{5.16}$$

Based on (5.15) and (5.16), (5.14) can be re-written as

$$\left(Q_w + {Q_w}^T\right)\boldsymbol{g_o} + \boldsymbol{b}_w = 0 \, . \tag{5.17}$$

The system of *N* linear equations in *N* unknowns defined in (5.17) can then be solved to specify the designed filter's frequency response $\boldsymbol{g_o}$.

The second window, $\boldsymbol{w_o}$ can also be solved in a similar manner. From (5.11), it can be observed that since W is a diagonal matrix then,

$$W\bar{A}_\iota \boldsymbol{g_o} = \widetilde{Z}_\iota \boldsymbol{w}$$

where $\widetilde{Z}_{\iota(\mathrm{NxN})}$ is a diagonal matrix so that $\bar{A}_\iota \boldsymbol{g_o} = diag(\widetilde{Z}_\iota)$. Now (5.11) can be re-written as:

$$J(\boldsymbol{g}, \boldsymbol{w}) = \tfrac{1}{M}\textstyle\sum_{i=1}^{M}\left(\widetilde{Z}_\iota \boldsymbol{w} - \boldsymbol{x}_i\right)^H \left(\widetilde{Z}_\iota \boldsymbol{w} - \boldsymbol{x}_i\right) \tag{5.18}$$

Expanding (5.18) gives:

$$J(\boldsymbol{g}, \boldsymbol{w}) = \tfrac{1}{M}\textstyle\sum_{i=1}^{M}(\boldsymbol{w}^H {\widetilde{Z}_\iota}^H \widetilde{Z}_\iota \boldsymbol{w} - \boldsymbol{w}^H {\widetilde{Z}_\iota}^H \boldsymbol{x}_i - {\boldsymbol{x}_i}^H \widetilde{Z}_\iota \boldsymbol{w} + {\boldsymbol{x}_i}^H \boldsymbol{x}_i)$$

$$= \tfrac{1}{M}\textstyle\sum_{i=1}^{M}(\boldsymbol{w}^H {\widetilde{Z}_\iota}^H \widetilde{Z}_\iota \boldsymbol{w} - ({\boldsymbol{x}_i}^H \widetilde{Z}_\iota \boldsymbol{w})^H - {\boldsymbol{x}_i}^H \widetilde{Z}_\iota \boldsymbol{w} + {\boldsymbol{x}_i}^H \boldsymbol{x}_i)$$

$$= \tfrac{1}{M}\textstyle\sum_{i=1}^{M}\left(\boldsymbol{w}^H {\widetilde{Z}_\iota}^H \widetilde{Z}_\iota \boldsymbol{w} - 2Re({\boldsymbol{x}_i}^H \widetilde{Z}_\iota \boldsymbol{w}) + {\boldsymbol{x}_i}^H \boldsymbol{x}_i\right)$$

since $\boldsymbol{w}$ is real-valued, the above equation becomes:

$$= \tfrac{1}{M}\textstyle\sum_{i=1}^{M}\left(\boldsymbol{w}^T Q_{g,i} \boldsymbol{w} + {\boldsymbol{b}_{g,i}}^T \boldsymbol{w} + c_i\right) \tag{5.19}$$

Where the matrix $Q_{g,i\ (\mathrm{NxN})}$, the column vector $\boldsymbol{b}_{g,i}$, and the scalar c_i are:

$$Q_{g,i} = {\widetilde{Z}_\iota}^H \widetilde{Z}_\iota \, ,$$

$$\boldsymbol{b}_{g,i} = (-2Re({\boldsymbol{x}_i}^H \widetilde{Z}_\iota))^T \, ,$$

$$c_i = {\boldsymbol{x}_i}^H \boldsymbol{x}_i = \|\boldsymbol{x}_i\|^2 \, .$$

Then, (5.19) can be expressed as:

$$J(\boldsymbol{g}, \boldsymbol{w}) = \boldsymbol{w}^T Q_g \boldsymbol{w} + \boldsymbol{b}_g{}^T \boldsymbol{w} + c \ , \tag{5.20}$$

where $Q_g = \frac{1}{M}\sum_{i=1}^{M} Q_{g,i}$, $\boldsymbol{b}_g = \frac{1}{M}\sum_{i=1}^{M} \boldsymbol{b}_{g,i}$, and $c = \frac{1}{M}\sum_{i=1}^{M} c_i$

Similarly, the vector $\boldsymbol{w_o}$ that minimizes (5.20) is determined, i.e. $\nabla_{\boldsymbol{w}} J(\boldsymbol{g}, \boldsymbol{w})|_{\boldsymbol{w}=\boldsymbol{w_o}} = 0$, thus, based on the same principles as in (5.15) and (5.16) the following expression can then be obtained:

$$\left(Q_g + Q_g{}^T\right)\boldsymbol{w_o} + \boldsymbol{b}_g = 0 \ . \tag{5.21}$$

The system of *N* linear equations in *N* unknowns defined in (5.21) can then be solved to specify the time window $\boldsymbol{w_o}$.

Since both (5.17) and (5.21) require knowledge of $\boldsymbol{w_o}$ and $\boldsymbol{g_o}$ respectively, an iterative procedure is adopted, which is as follows:

Step 1: Initialize W and G to identity matrices and set *k = 0.*

Step 2: Solve for $\boldsymbol{g_{o,k}}$ using (5.17)

Step 3: Based on the $\boldsymbol{g_{o,k}}$, obtain $\boldsymbol{w_{o,k}}$ using (5.21)

Step 4: Iterate Steps 2 and 3 until the solution converges.

5.1.2.1 Experimental Results

A preliminary experimental validation of this method has been performed through its application on ECG (Electrocardiogram) data obtained from the MIT-BIH Arrhythmia database.

ECG signals are measurements of the bioelectrical activity of the heart and are widely used for the diagnosis of cardiovascular diseases. A particularly useful type of ECG is the one acquired during graded exercise assessment – stress testing – of the subject on a cardiovascular machine. Stress ECG is more likely to reveal certain underlying heart conditions in contrast to ECG recordings from a resting patient. On the other hand, the

acquisition of ECG during the subject's activity is a difficult task resulting in a signal corrupted with various types of interference. Electrode motion artifact [6] – annotated as 'em' by clinicians on ECG recordings – is generally considered to be the most troublesome among those interferences. It is therefore crucial to remove this distortion prior to any clinical evaluation.

Filtering electrode motion artifact out of the ECG is a non-trivial task because this interference overlaps with the useful signal in both the time and the frequency domains [6]. Consequently, any basic pass-band type of filter would be inadequate in dealing with this problem as it would not be able to suppress noise components and preserve useful signal information at the same time. A better result could be obtained if the statistics of the interference were known. In that case, the frequency response of the filter could be designed to optimally remove the noise – using, for instance, a Wiener filter-based approach [3]. Alternatively, if some estimate of the motion artifact was available then adaptive interference cancellation methods could be applied to enhance the ECG [7], and [8]. Subsequently, it was identified that additional performance advantages may be achieved by replacing the single filter in the aforementioned approaches with the system depicted in Figure 5-7. Moreover since, the statistics of the motion interference are not known, this would be a good example to illustrate the applicability of the above alternative solution.

Thus, the rationale behind this work is that by modifying the signal consecutively in the frequency and the time domains it may be possible to create a system that can better suppress interference as compared to a Fourier filter on its own. Drawing upon the simple example of Figure 5-1 one may assume that the above is feasible, at least for signals with similar time-frequency characteristics. By examining the pseudo-Wigner distribution of a noiseless ECG recording (Figure 5-8a) it becomes apparent that this signal consists of distinct higher-frequency elements (corresponding to QRS complexes) (Figure 5-8b).

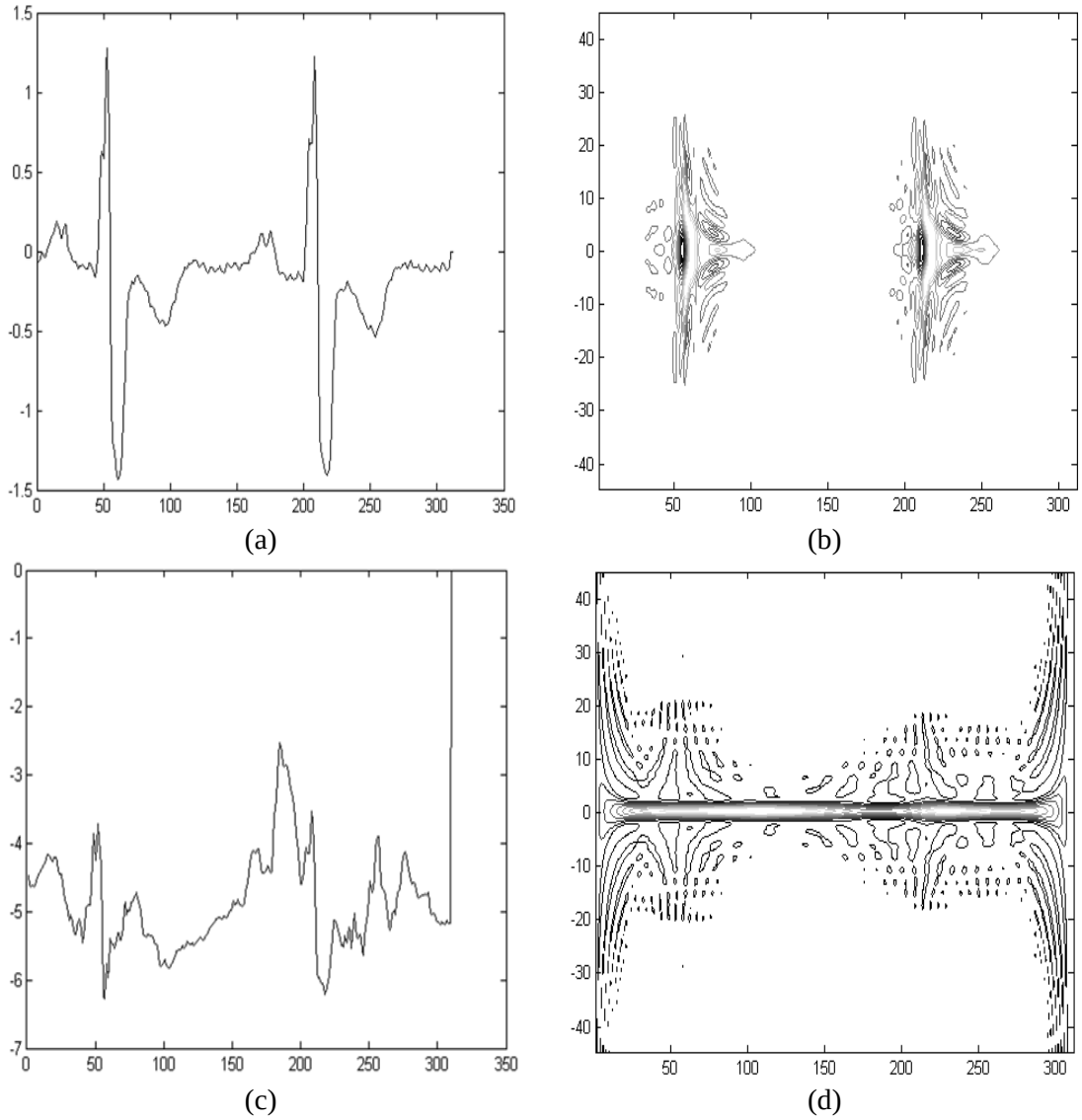

Figure 5-8 *(a) A segment of a clean ECG signal, (b) the corresponding time-frequency plot, (c) the above segment corrupted with 'em' noise at 6dB SNR, (d) time-frequency plot of the noisy ECG.*

Figure 5-8c shows the same ECG segment corrupted by motion artifact noise of 6dB SNR. It is evident that the useful waveform is now severely distorted, and that its frequency content is obscured across time (Figure 5-8d).

As previously indicated, the ECG data used in this study was obtained from the MIT-BIH Arrhythmia database [9]. The database contains clean ECG recordings along with their corresponding versions contaminated with additive 'em' (electrode motion artifact) noise at six different SNR levels.

To demonstrate the legitimacy of the original assumption, i.e. that the proposed two-stage system can outperform a single filter on enhancing the ECG, the same set of data is filtered with an optimized filter designed to minimize (5.7). The associated frequency response can be obtained from the derivations presented above, by simply setting *W* equal to an identity matrix and solving the resulting set of linear equations.

To quantify the performance of the two compared approaches, the root-mean-square error (RMSE) and the normalized correlation coefficient (NCC) [10] are used. The NCC can be calculated as,

$$NCC = \frac{\sum_{n=1}^{N} x(n)\hat{x}(n)}{\sqrt{\sum_{n=1}^{N} x^2(n) \sum_{n=1}^{N} \hat{x}^2(n)}}$$

where *N* is the signal length, $x(n)$ is the desired signal and $\hat{x}(n)$ is the filtered signal. A higher value of NCC signifies a good correlation between the filtered result and ideal signal. The results of the experiments are listed in Table 5-1, where it is clear that this two-stage system consistently outperforms the single-stage filter at all noise levels both in terms of the RMSE and the NCC measures.

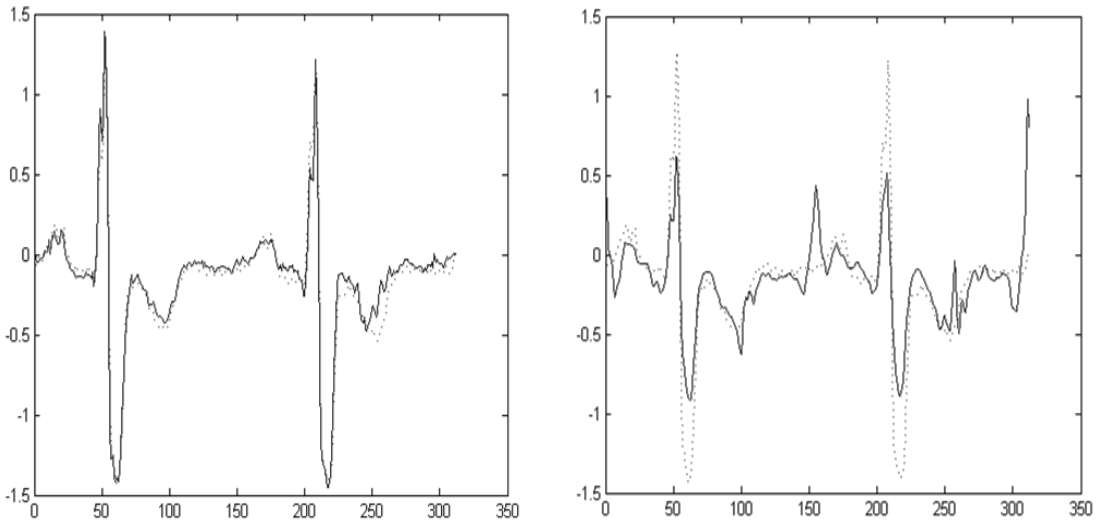

(a) (b)

Figure 5-9 *Filtered ECG signal after applying: (a) the proposed method (solid line), and (b) a single optimized Fourier filter (solid line). The ideal ECG is also shown (dotted lines). The contaminated ECG contained motion artifact noise of 18dB SNR.*

TABLE 5-1

RMSE AND NCC VALUES OF THE FILTERED ECG SIGNALS CORRESPONDING TO DIFFERENT LEVELS OF MOTION ARTIFACT DENOISED WITH THE PRESENTED METHOD AND A SINGLE OPTIMIZED FOURIER FILTER

Method \ SNR(dB)		24	18	12	6	0	-6
Proposed	RMSE	0.0595	0.0721	0.1003	0.2005	0.1532	0.1391
	NCC	0.9905	0.9859	0.9724	0.9007	0.9354	0.9531
Optimized Fourier Filter	RMSE	0.2110	0.2239	0.2568	0.3144	0.3670	0.3910
	NCC	0.8811	0.8653	0.8165	0.6918	0.5207	0.4152

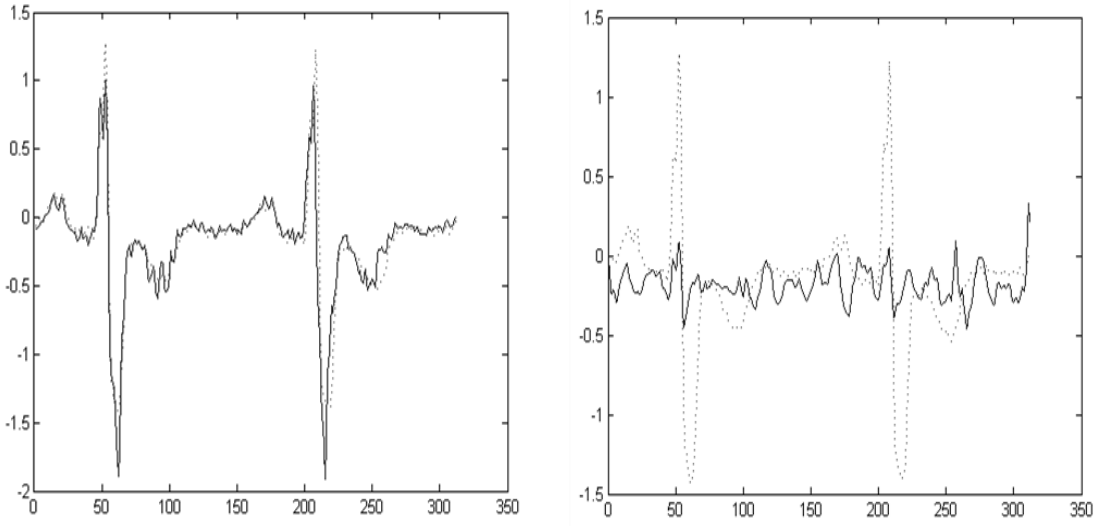

(a) (b)

Figure 5-10 *Filtered ECG signal after applying: (a) the proposed method (solid line), and (b) a single optimized Fourier filter (solid line). The ideal ECG is also shown (dotted lines). The contaminated ECG contained motion artifact noise of 0dB SNR.*

Figures 5-9 and 5-10 show the same segment of a filtered ECG signal based on the above approaches for two different noise levels.

Thus it can be seen that, through this work, an alternative filtering scheme for the removal of motion artifacts from stress ECG signals has been presented. The method is based on a two-stage system comprising a linear time-invariant filter and a time window. The overall system was designed based on the MSE minimization criterion, and the two components were optimized accordingly. Furthermore, the presented formulation does not require knowledge of the corrupting noise statistics.

As demonstrated in previous chapters, the flexibility offered by T-F rotation could be harnessed further by involving more than one domain in the filtering process. This way, superior results can be achieved as compared to single-stage filters and additionally, filters operating successively in conventional domains, as presented thus far. Therefore in following section, this concept of filtering will further be generalised to operate in consecutive fractional Fourier domains.

5.2 Repeated Signal Modifications in Fractional Fourier Domains

Figure 5-11 depicts the configuration of a filtering system operating consecutively in *M* fractional Fourier domains:

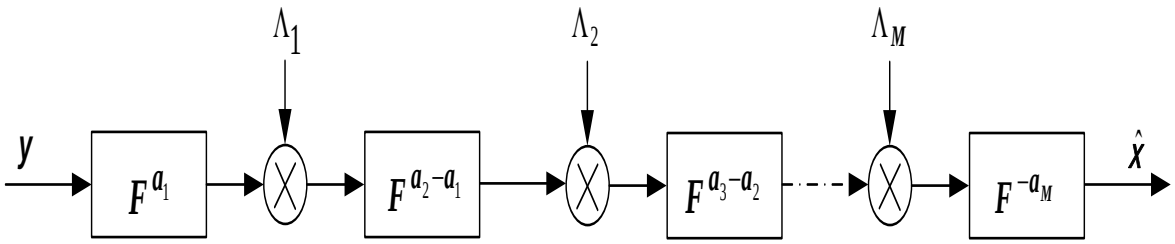

Figure 5-11 *Block diagram of a filtering system operating successively in M fractional Fourier domains.*

The above diagram can be expressed analytically as follows:

$$\hat{\boldsymbol{x}} = F_{-a_M} \Lambda_M \cdots F_{a_{k+1}-a_k} \Lambda_k \ldots F_{a_2-a_1} \Lambda_1 F_{a_1} \boldsymbol{y} \tag{5.22}$$

Where $\Lambda_{k(\mathrm{NxN})}$ are diagonal matrices composed of the elements of the corresponding windows $\boldsymbol{h_1}, \ldots, \boldsymbol{h_k}, \ldots, \boldsymbol{h_M}$; thus, $\boldsymbol{h_k} = diag(\Lambda_k) = \left[h_{k,0}, \ldots, h_{k,N-1}\right]^T$; F_{a_1} (NxN), $F_{a_2-a_1(\mathrm{NxN})}, \ldots, F_{a_{k+1}-a_k(\mathrm{NxN}), \ldots,} F_{-a_M}$ (NxN) are the discrete FrFT matrices defined in (2.21), which transforms the signal from the time domain to the a_1^{th} domain, from the a_1^{th} to the a_2^{th}, from the a_k^{th} to the a_{k+1}^{th} and so on until the a_M^{th} domain is reached, at which point the final discrete FrFT matrix will convert the signal back to the time domain.

The filtering goal is to deliver an estimate $\hat{\boldsymbol{x}}$ which will be as close as possible to the desired signal $\boldsymbol{x}$, using the modification process of (5.22). A natural criterion of closeness is the mean square error (MSE),

$$\text{mse}(\hat{\boldsymbol{x}}) = \frac{1}{\text{N}}\text{E}[\|\boldsymbol{e}\|^2]\,, \tag{5.23}$$

where the error signal $\boldsymbol{e}$ equals to $\hat{\boldsymbol{x}} - \boldsymbol{x}$, and $\|\boldsymbol{e}\|^2 = \boldsymbol{e}^H\boldsymbol{e} = \sum_{m=0}^{N-1}|e_m|^2$, ($\boldsymbol{e}^H$is the conjugate transpose of $\boldsymbol{e}$). To optimally design the filtering system of Figure 5-11, the vectors $\boldsymbol{h_1}, \boldsymbol{h_2}, \dots, \boldsymbol{h_M}$ must be determined so that (5.23) is minimised. Therefore, a similar observation model defined in (4.1) shall be used again to guide this derivation. Precisely, in measurements under additive noise, the following generic observation model can be assumed:

$$\boldsymbol{y} = D\boldsymbol{x} + \boldsymbol{n}, \tag{5.24}$$

where $\boldsymbol{y}, \boldsymbol{x}, \boldsymbol{n}$ are column vectors of size *N* standing for the acquired signal, the desired signal, and the noise, respectively. Matrix *D* represents some additional degradation function acting upon the signal.

Similar to (4.7), the MSE defined in (5.23) can likewise be estimated by the sum,

$$\frac{1}{MN}\sum_{i=1}^{M}\|\hat{\boldsymbol{x}}_i - \boldsymbol{x}_i\|^2 = \frac{1}{MN}\sum_{i=1}^{M}\|\boldsymbol{e_i}\|^2, \tag{5.25}$$

where $\boldsymbol{x}_i$ is the i^{th} realisation of signal $\boldsymbol{x}$ and $\hat{\boldsymbol{x}}_i$ is the corresponding estimate. By substituting (5.22) into (5.25) the following cost function can then be obtained:

$$J(\boldsymbol{\theta}) = \frac{1}{MN}\sum_{i=1}^{M}\left\|F_{-a_M}\Lambda_M \cdots F_{a_{k+1}-a_k}\Lambda_k \dots F_{a_2-a_1}\Lambda_1 F_{a_1}\boldsymbol{y}_i - \boldsymbol{x}_i\right\|^2 . \tag{5.26}$$

Where $\boldsymbol{\theta}$ represents the corresponding windows $\boldsymbol{h_1}, \boldsymbol{h_2}, \dots, \boldsymbol{h_M}$; thus,. $\boldsymbol{\theta} = \{\boldsymbol{h_1}, \boldsymbol{h_2}, \dots, \boldsymbol{h_M}\}$. For simplicity, $\boldsymbol{h_1}, \boldsymbol{h_2}, \dots, \boldsymbol{h_M}$ are constrained to be real-valued windows.

Let's now derive an optimum expression for the k^{th} filter (i.e. $\boldsymbol{h_k}$) from (5.26). However before proceeding, it can be observed that (5.26) is not a convenient expression for the purpose of optimization.

Thus, to convert it into a more suitable form, further manipulations are required. Let, $\boldsymbol{a}_i = F_{a_k - a_{k-1}} \Lambda_{k-1} F_{a_{k-1} - a_{k-2}} \Lambda_{k-2} \cdots \Lambda_1 F_{a_1} \boldsymbol{y}_i$ and $B = F_{-a_M} \Lambda_M \cdots F_{a_{k+2} - a_{k+1}} \Lambda_{k+1}$ so that (5.26) becomes:

$$J(\boldsymbol{\theta}) = \frac{1}{MN} \sum_{i=1}^{M} \left\| B F_{a_{k+1} - a_k} \Lambda_k \boldsymbol{a}_i - \boldsymbol{x}_i \right\|^2 . \tag{5.27}$$

Since Λ_k is a diagonal matrix it is easy to show that $\Lambda_k \boldsymbol{a}_i = A_i \boldsymbol{h_k}$, where $A_{i(\text{NxN})}$ is a diagonal matrix such that $\boldsymbol{a}_i = diag(A_i)$. Thus (5.27) can be further simplified as:

$$J(\boldsymbol{\theta}) = \frac{1}{MN} \sum_{i=1}^{M} \| B \bar{A}_i \boldsymbol{h_k} - \boldsymbol{x}_i \|^2 , \tag{5.28}$$

where $\bar{A}_{i(\text{NxN})} = F_{a_{k+1} - a_k} A_i$.

Now (5.28) can also be represented as:

$$J(\boldsymbol{\theta}) = \frac{1}{MN} \sum_{i=1}^{M} (B \bar{A}_i \boldsymbol{h_k} - \boldsymbol{x}_i)^H (B \bar{A}_i \boldsymbol{h_k} - \boldsymbol{x}_i) \tag{5.29}$$

Expanding (5.29) yields:

$$\begin{aligned} J(\boldsymbol{\theta}) = \frac{1}{MN} \sum_{i=1}^{M} (& \boldsymbol{h_k}^H \bar{A}_i^H B^H B \bar{A}_i \boldsymbol{h_k} - \boldsymbol{h_k}^H \bar{A}_i^H B^H \boldsymbol{x}_i - \\ & \boldsymbol{x}_i^H B \bar{A}_i \boldsymbol{h_k} + \boldsymbol{x}_i^H \boldsymbol{x}_i) \\ = \frac{1}{MN} \sum_{i=1}^{M} (& \boldsymbol{h_k}^H \bar{A}_i^H B^H B \bar{A}_i \boldsymbol{h_k} - (\boldsymbol{x}_i^H B \bar{A}_i \boldsymbol{h_k})^H - \\ & \boldsymbol{x}_i^H B \bar{A}_i \boldsymbol{h_k} + \boldsymbol{x}_i^H \boldsymbol{x}_i) \\ = \frac{1}{MN} \sum_{i=1}^{M} \Big(& \boldsymbol{h_k}^H \bar{A}_i^H B^H B \bar{A}_i \boldsymbol{h_k} - 2Re(\boldsymbol{x}_i^H B \bar{A}_i \boldsymbol{h_k}) + \boldsymbol{x}_i^H \boldsymbol{x}_i \Big) , \end{aligned}$$

Since $\boldsymbol{h_k}$ is real-valued, the above equation becomes:

$$= \frac{1}{MN} \sum_{i=1}^{M} \left(\boldsymbol{h_k}^T Q_i \boldsymbol{h_k} + \boldsymbol{d}_i^T \boldsymbol{h_k} + c_i \right) \tag{5.30}$$

where the matrix $Q_{i\ (\text{NxN})}$, the column vector $\boldsymbol{d}_i$, and the scalar c_i are:

$$Q_i = \bar{A}_i^H B^H B \bar{A}_i ,$$

$$\boldsymbol{d}_i = (-2Re(\boldsymbol{x}_i^H B \bar{A}_i))^T ,$$

$$c_i = \boldsymbol{x}_i^H \boldsymbol{x}_i = \| \boldsymbol{x}_i \|^2 .$$

Finally, (5.30) can be expressed as:

$$J(\boldsymbol{\theta}) = \boldsymbol{h_k}^T Q \boldsymbol{h_k} + \boldsymbol{d}^T \boldsymbol{h_k} + c , \tag{5.31}$$

where $Q = \frac{1}{MN} \sum_{i=1}^{M} Q_i$, $\boldsymbol{d} = \frac{1}{MN} \sum_{i=1}^{M} \boldsymbol{d}_i$, and $c = \frac{1}{MN} \sum_{i=1}^{M} c_i$. To obtain the vector $\boldsymbol{h_k}^*$ that minimizes (5.31), the following equation must be solved:

$$\nabla_{\boldsymbol{h_k}} J(\boldsymbol{\theta}) \big|_{\boldsymbol{h_k} = \boldsymbol{h_k}^*} = 0 . \tag{5.32}$$

As presented in Section 5.1.1, the derivative of the first term of (5.31) with respect to the vector $\boldsymbol{h_k}$ can be computed as:

$$\nabla_{\boldsymbol{h_k}}\{\boldsymbol{h_k}^T Q \boldsymbol{h_k}\} = Q\boldsymbol{h_k} + Q^T\boldsymbol{h_k} \quad , \tag{5.33}$$

Likewise, the second term can be expanded as,

$$\nabla_{\boldsymbol{h_k}}\{\boldsymbol{d}^T\boldsymbol{h_k}\} = \boldsymbol{d} \, . \tag{5.34}$$

Based on (5.33) and (5.34), (5.32) can be re-written as

$$(Q + Q^T)\boldsymbol{h_k}^* + \boldsymbol{d} = 0 \, . \tag{5.35}$$

The system of *N* linear equations in *N* unknowns defined in (5.35) can then be solved to specify the designed filter's frequency response $\boldsymbol{h_k}^*$. Furthermore, since (5.35) requires knowledge of both the preceding and proceeding windows from the k^{th} position, an iterative procedure is adopted, which is as follows:

Step 1: Initialize all windowing functions in $\boldsymbol{\theta}$ to identity matrices.

Step 2: Set *k = 1* and solve for $\boldsymbol{h_k}$ using (5.35)

Step 3: Based on the $\boldsymbol{h_k}$, obtain $\boldsymbol{h_{k+1}}$ using (5.35) and set *k = k+1*.

Step 4: Repeat step 3 until the final windowing function is reached (i.e. $\boldsymbol{h_M}$) .

Step 5: Iterate Steps 2 to 4 until the solution converges.

To illustrate this iterative process, let's consider the following example to obtain the optimized frequency response $\boldsymbol{h_1}, \boldsymbol{h_2}$ involved in a 2-stage filtering configuration:

In the beginning, all diagonal matrices Λ_1, Λ_2 are initialized to the identity matrix, I. Then starting with the first iteration, an estimate for the optimum expression of h_1 is calculated based on (5.35) with; $A_i = diag(F_{a_1} y_i)$; $B = F_{-a_2}\Lambda_2$; $\bar{A_i} = F_{a_2 - a_1} A_i$. Then using this preliminary solution of h_1, an initial estimate for the optimum h_2 is obtained by means of (5.35) again but now with; $A_i = diag(F_{a_2 - a_1}\Lambda_1 F_{a_1} y_i)$; $B = I$; $\bar{A_i} = F_{-a_2} A_i$. The above steps are repeated with Λ_1, Λ_2 being updated accordingly at each iteration. Once the solutions converge the iterations stop.

5.2.1 Experimental Results

To demonstrate the advantages of this extension, three different signal scenarios of the kind typically used in relevant studies [4], [11]-[13] were considered. These are computer-simulated waveforms consisting of multiple elements overlapping both in time and frequency. The aim is then to recover individual components – the 'desired' signals – from their corresponding mixtures. A certain degree of randomness has been added to the amplitudes and time locations of the simulated signals. In each example, a set of ten realizations of the desired waveforms along with their associated noisy observations have been generated. Based on these, the most suitable domains and modification windows are established. The resulting filters are subsequently applied to a previously unseen realization of the distorted signal. For comparisons, the above sets of signals have also been used to design single-stage filters operating in the most suitable rotated domain in each case, according to the work presented in Section 4.1.2.

The test signal in the first example involves the sum:

$$Ae^{-\pi(t-s)^2} + Ae^{-\pi((t-s)0.5)^2}e^{(j2\pi(t-s)1.75)} + Ae^{-\pi((t-s)0.5)^2}e^{(-j2\pi(t-s)1.75)} + Ae^{-\pi(t+s)^2}$$

where *A* and *s* are random variables uniformly distributed in the interval [1.5, 2.5]. The first of the four terms corresponds to the desired waveform. The signal also contains added white noise of finite duration between [-2, 2], which has been low-pass filtered (normalized cut-off frequency at 0.05), and subsequently modulated by the quadratic complex exponential term $e^{-j2\pi(0.35)t^2}$ in order to tilt this noise component in the T-F plane. A second noise element designed in the same manner but modulated using the function $e^{j2\pi(0.35)t^2}$ has also been added to the signal. Figure 5-12a shows a realization of the desired signal $x(t)$, whereas the overall signal $y(t)$ is depicted in Figure 5-12b. The recovered signals $\hat{x}(t)$ after treating $y(t)$ with the different filtering schemes are illustrated in Figures 5-12c and 5-12d. The order of the most suitable domain for the single-stage

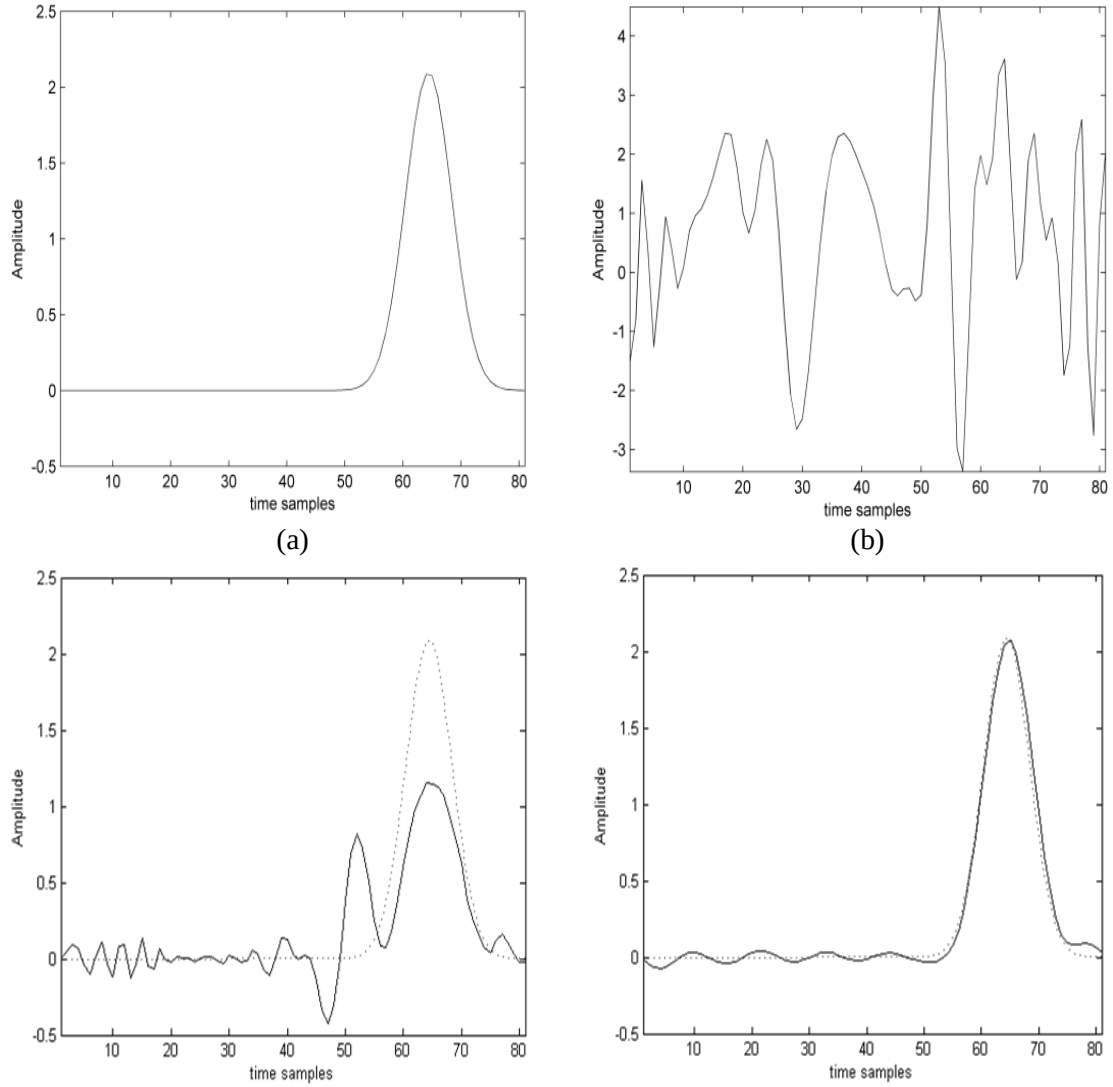

Figure 5-12 *(a) A realization of the desired signal $x(t)$, (b) the resultant corrupted signal $y(t)$, (c) Estimate obtained by filtering in the a = 0.71 domain (solid) and the desired signal (dotted), (d) Estimate obtained by filtering in the a = 0 and b =1 domain (solid) and the desired signal (dotted).*

filter was found to be a = 0.71, while the ordinary time and frequency domains were the most suitable ones for the dual modification system. The superiority of this two-stage system is obvious in this example. The scenario in the second example considers the sum of three linear frequency-modulated complex exponentials: $Ae^{-j9\pi t^2} + Ae^{j2\pi(-4t^2+6t)} + Ae^{j2\pi(-4t^2-6t)}$, where A is uniformly distributed in the interval [1, 3]. The first component of this sum is the waveform to be recovered. White Gaussian noise of 10dB SNR has been superimposed on the three chirps, and the overall signal is further degraded by way of the

quantization process, $\frac{\text{round}(\text{b}\, z(t))}{\text{b}}$, where $z(t)$ is the input signal. The positive integer b is the quantization factor; the lower the value of b, the coarser the quantization effect (in this example, b was set to its lowest level, 1). It should be noted that the statistical model for this kind of distortion cannot be known in advance because it is a function of the input process. Neither is it possible to collect a set of independent realizations of such type of noise in order to approximate its statistics.

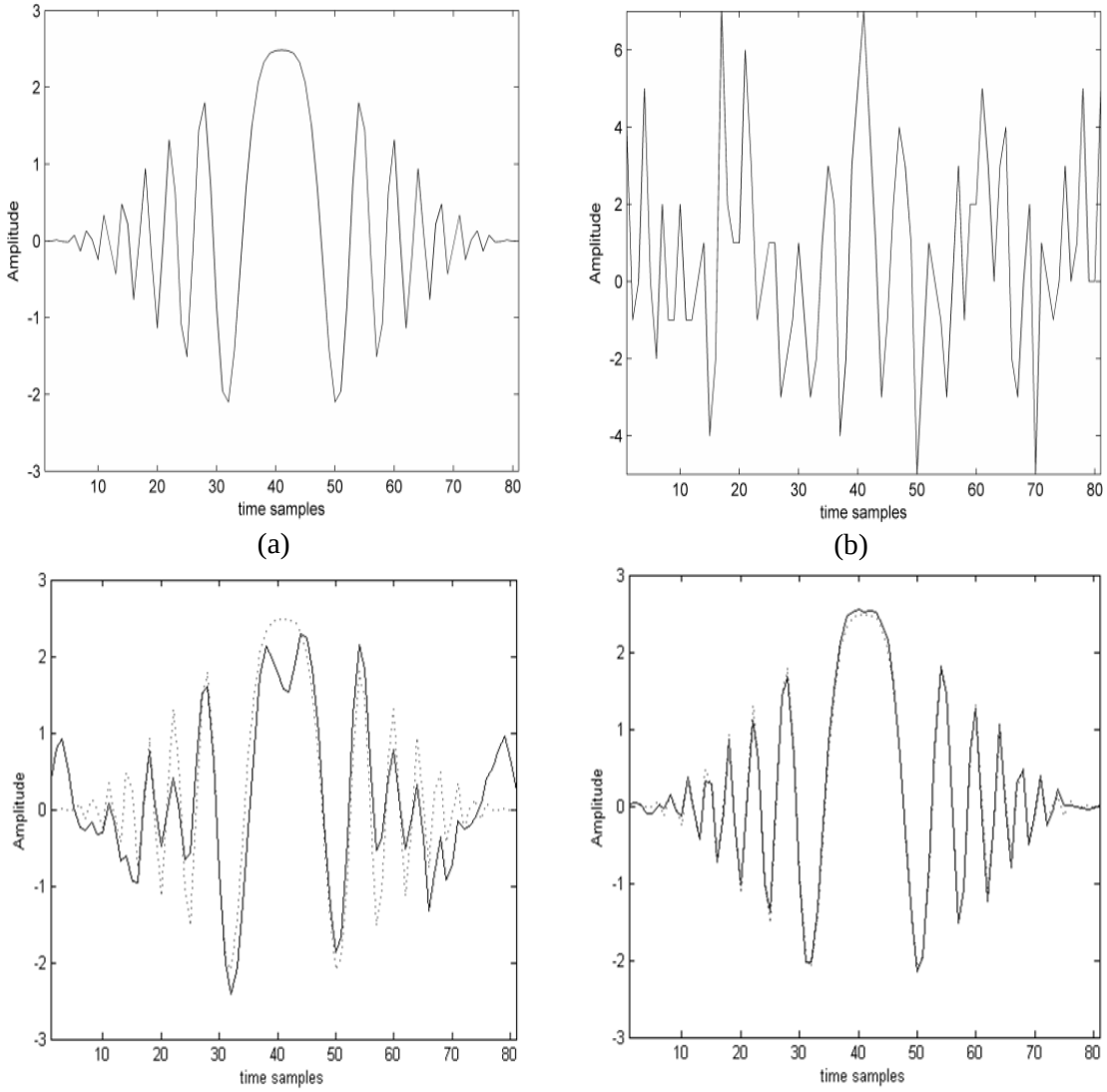

Figure 5-13 *(a) A realization of the desired signal $x(t)$, (b) the resultant corrupted signal $y(t)$, (c) Estimate obtained by filtering in the a = 0.77 domain (solid) and the desired signal (dotted), (d) Estimate obtained by filtering in the a = 1.35 and b = 0.55 domain (solid) and the desired signal (dotted).*

Figures 5-13a and 5-13b depict the desired signal and the corrupted mixture, respectively. The results after filtering with the different approaches are presented in Figures 5-13c and 5-13d. The most suitable domain for a single filtering application was the one obtained for $a = 0.77$. The most suitable domains for the two-stage system were equal to $a = 1.35$, and $b = 0.55$, respectively. It is clear that yet again a two-stage configuration can provide a more accurate restoration of the desired signal.

The scenario in a third example considers a signal separation problem, where the sum of the resultant signal can be expressed as;

$$\left(Ae^{-\pi(0.2t)^2}e^{(-j2\pi t)} + Ae^{-\pi(0.22t)^2}e^{(-j2\pi(0.3)t)}\right)e^{(j2\pi Ft)} +$$
$$5Ae^{-\pi(0.2(t+5))^2}e^{(j2\pi(0.5(t+5))^2)} + 5Ae^{-\pi(0.2(t-5))^2}e^{(j2\pi(-0.5(t-5))^2)} +$$
$$(7Ae^{-\pi(1.7(t+7))^2}e^{(j2\pi(-0.5)t)} + 7Ae^{-\pi(1.7(t-7))^2}e^{(j2\pi(-0.5)t)})e^{(j2\pi Ft)} +$$
$$7Ae^{-\pi(1.5(t+s))^2}e^{(j2\pi(3)t)},$$

where *A, F and s* are random variables, uniformly distributed over the intervals [1, 3], [-1, 1] and [-2, 2], respectively. The aim is then to recover the first two components in the above resultant signal. In this example, the best-attainable results based on a single-stage, two-stage and finally three-stage system are contrasted. Figure 5-14a shows a realization of corrupted mixture $y(t)$. The results after filtering with the different approaches are presented in Figures 5-14b, c and d, respectively. The most suitable domain for a single filtering application was the one obtained for $a_1 = 1$. The most suitable domains for the two-stage system were equal to $a_1 = 0.5$, and $a_2 = 1.5$, respectively. Meanwhile, the most suitable domains for the three-stage system were equal to $a_1 = 0.5$, $a_2 = 1$ and $a_3 = 1.5$, respectively. It is clear that a three-stage filtering system in this scenario can yield in a more accurate restoration of the desired signal. From Figure 5-14, it is also evidently clear that by increasing the number of filtering stages, one could gradually improve the final result. These findings are in accordance to the theoretical conclusions at the beginning of this chapter.

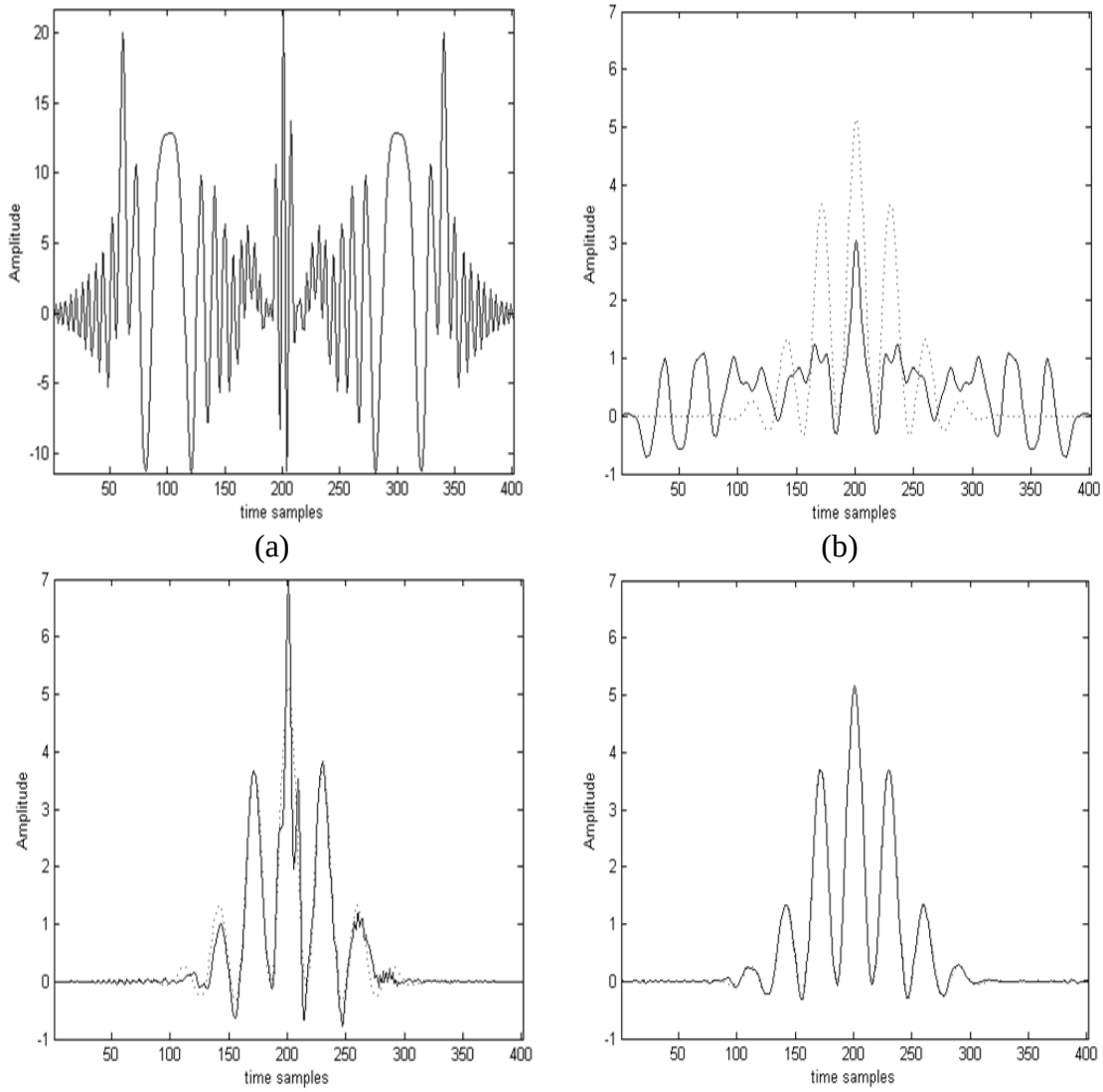

Figure 5-14 *(a) The resultant corrupted signal $y(t)$, (b) Estimate obtained by filtering in the a_1 = 1 domain (solid) and the desired signal (dotted), (c) Estimate obtained by filtering in the a_1 = 0.5 and a_2 =1.5 domain (solid) and the desired signal (dotted) (d) Estimate obtained by filtering in the a_1 = 0.5, a_2 =1 and a_3=1.5 domain (solid) and the desired signal (dotted).*

So far, it can be appreciated that optimizing an M-stage system configuration is not a straightforward task, as it entails dealing with non-linear objective functions. One way around this problem is to adopt an iterative approach, in which each filter in the system is obtained one at a time whilst keeping the remainder fixed to the values computed in preceding iterations. During each cycle, individual estimates will be refined accordingly, and this whole process is continued until convergence has been reached. An alternative to this iterative approach is also explored and detailed in the following section.

5.2.2 Alternative Minimization Approach

In the final part of this work, an alternative method for finding the optimized filter profiles for a given filtering configuration, which does not involve an iterative-based solution, is explored. For simplicity, a two-stage system has been chosen to illustrate this approach. Thus, the overall filtering process for a two-stage formation can be expressed as,

$$\hat{\boldsymbol{x}} = F_{-b}HF_{b-a}GF_a\boldsymbol{y}\ , \tag{5.36}$$

where $G_{(\mathrm{NxN})}$ and $H_{(\mathrm{NxN})}$ are diagonal matrices composed of the elements of the corresponding windows $\boldsymbol{g}$ and $\boldsymbol{h}$, respectively; thus, $\boldsymbol{g} = diag(G) = [g_0, \dots, g_{N-1}]^T$ and $\boldsymbol{h} = diag(H) = [h_0, \dots, h_{N-1}]^T$; $F_{a\ (\mathrm{NxN})}$, $F_{b-a(\mathrm{NxN})}$ and $F_{-b\ (\mathrm{NxN})}$ are the discrete FrFT matrices defined in (2.21), which transform the signal from the time domain to the *a*th domain, from the *a*th to the *b*th, and from the *b*th domain back to time, respectively.

The filtering goal is exactly the same as before, which is to deliver an estimate $\hat{\boldsymbol{x}}$ which is as similar as possible to the desired signal $\boldsymbol{x}$, using the modification process of (5.36). Thus by basing ourselves on a similar observation model as in (5.24) and using the MSE estimate described in (5.25), the cost function for an two-stage FrFT filtering configuration can now be defined, which is as follows:

$$J(\boldsymbol{h},\boldsymbol{g}) = \frac{1}{MN}\sum_{i=1}^{M}\|F_{-b}HF_{b-a}GF_a\boldsymbol{y}_i - \boldsymbol{x}_i\|^2\ . \tag{5.37}$$

Additionally as before, $\boldsymbol{g}$ and $\boldsymbol{h}$ are constrained to be real-valued windows for simplicity. Nevertheless, it can be appreciated that (5.37) is not a convenient expression for the purpose of optimization. To convert it into a more suitable form, further manipulations are required. Let $\boldsymbol{z}_i = F_a\boldsymbol{y}_i$, so that (5.37) becomes:

$$J(\boldsymbol{h},\boldsymbol{g}) = \frac{1}{MN}\sum_{i=1}^{M}\|F_{-b}HF_{b-a}G\boldsymbol{z}_i - \boldsymbol{x}_i\|^2\ . \tag{5.38}$$

Since G is a diagonal matrix it is easy to show that $G\boldsymbol{z}_i = Z_i\boldsymbol{g}$, where $Z_{i(\mathrm{NxN})}$ is a diagonal matrix such that $\boldsymbol{z}_i = diag(Z_i)$. Thus (5.38) can be further simplified as:

$$J(\boldsymbol{h},\boldsymbol{g}) = \frac{1}{MN}\sum_{i=1}^{M}\|F_{-b}H\overline{Z}_i\boldsymbol{g} - \boldsymbol{x}_i\|^2\ , \tag{5.39}$$

where $\bar{Z}_{\iota(\mathrm{NxN})} = F_{b-a} Z_i$ .By carrying out the matrix multiplications inside the norm of (5.39), the m^{th} element e_{i_m} of the error vector $\boldsymbol{e_i}$ (from (5.25)) becomes:

$$e_{i_m} = \sum_{l=0}^{N-1} \sum_{k=0}^{N-1} f_{-b\ m,l}\, h_{\ l}\ \bar{z}_{i\ l,k}\ g_{\ k} \ -\ x_{i_m}\,, \tag{5.40}$$

where $f_{-b\ m,l}$, $h_{\ l}$, $\bar{z}_{i\ l,k}$, $g_{\ k}$, and x_{i_m}, (*m=0, …, N-1*), are the elements of F_{-b} , H , $\bar{Z}_{\iota}$, $\boldsymbol{g}$, and $\boldsymbol{x}_i$, respectively. The above double summation can alternatively be expressed as a matrix multiplication,

$$\sum_{l=0}^{N-1} \sum_{k=0}^{N-1} f_{-b\ m,l}\, h_{\ l}\ \bar{z}_{i\ l,k}\, g_{\ k} =$$

$$= [h_0 \cdots h_{N-1}] \begin{bmatrix} f_{-b\ m,0} & \cdots & 0 \\ \vdots & \ddots & \vdots \\ 0 & \cdots & f_{-b\ m,N-1} \end{bmatrix} \begin{bmatrix} \bar{z}_{i\ 0,0} & \cdots & \bar{z}_{i\ 0,N-1} \\ \vdots & \ddots & \vdots \\ \bar{z}_{i\ N-1,0} & \cdots & \bar{z}_{i\ N-1,N-1} \end{bmatrix} \begin{bmatrix} g_0 \\ \vdots \\ g_{N-1} \end{bmatrix} =$$

$$= \boldsymbol{h}^T\, F_{-b}^{\,m}\, \bar{Z}_{\iota}\, \boldsymbol{g}\,, \tag{5.41}$$

where $F_{-b}^{\,m}$ is a diagonal matrix containing the elements of the m^{th} row of F_{-b}. Further, the vectors $\boldsymbol{h}$ and $\boldsymbol{g}$ is integrated into a single vector $\boldsymbol{w}_{(2N\times 1)}$, $\boldsymbol{w} = [\boldsymbol{h^T} \quad \boldsymbol{g^T}]^{\boldsymbol{T}}$. By augmenting $F_{-b}^{\,m}$ and $\bar{Z}_{\iota}$ with zero-element submatrices, the following matrices of size $(2N \times 2N)$ can then be formed:

$$\overline{F_{-b}^{\,m}} = \begin{bmatrix} f_{-b\ m,0} & \cdots & 0 & 0 & \cdots & 0 \\ \vdots & \ddots & \vdots & \vdots & \ddots & \vdots \\ 0 & \cdots & f_{-b\ m,N-1} & 0 & \cdots & 0 \\ 0 & \cdots & 0 & 0 & \cdots & 0 \\ \vdots & \ddots & \vdots & \vdots & \ddots & \vdots \\ 0 & \cdots & 0 & 0 & \cdots & 0 \end{bmatrix} \quad \text{,and}$$

$$\overline{\bar{Z}_{\iota}} = \begin{bmatrix} 0 & \cdots & 0 & \bar{z}_{i\ 0,0} & \cdots & \bar{z}_{i\ 0,N-1} \\ \vdots & \ddots & \vdots & \vdots & \ddots & \vdots \\ 0 & \cdots & 0 & \bar{z}_{i\ N-1,0} & \cdots & \bar{z}_{i\ N-1,N-1} \\ 0 & \cdots & 0 & 0 & \cdots & 0 \\ \vdots & \ddots & \vdots & \vdots & \ddots & \vdots \\ 0 & \cdots & 0 & 0 & \cdots & 0 \end{bmatrix}.$$

This way, (5.41) can be modified as,

$$\boldsymbol{h}^T\, F_{-b}^{\,m}\, \bar{Z}_{\iota}\, \boldsymbol{g} = \boldsymbol{w}^T\, \overline{F_{-b}^{\,m}}\ \overline{\bar{Z}_{\iota}}\, \boldsymbol{w}. \tag{5.42}$$

Based on (5.42), e_{i_m} can be rewritten as,

$$e_{i_m} = \boldsymbol{w}^T \overline{F_{-b}^{\,m}}\ \overline{\overline{Z_i}}\ \boldsymbol{w} \ - \ x_{i_m} = \boldsymbol{w}^T\ Q_i^m\ \boldsymbol{w} \ - \ x_{i_m}$$

where $Q_i^m = \overline{F_{-b}^{\,m}}\ \overline{\overline{Z_i}}$. Finally, by substituting the new expression for $\boldsymbol{e_i}$ into (5.39) and expanding the norm, the following can be obtained:

$$J(\boldsymbol{w}) = \frac{1}{MN}\sum_{i=1}^{M}\sum_{m=0}^{N-1}\left|\boldsymbol{w}^T\ Q_i^m\ \boldsymbol{w} \ - \ x_{i_m}\right|^2 , \tag{5.43}$$

The objective function (5.43) simplifies the optimization problem in the sense that there is now a single variable to be determined instead of two. Moreover, the minimization of (5.43) will yield the optimized modification windows $\boldsymbol{g}$ and $\boldsymbol{h}$ simultaneously. Regarding the FrFT transformations involved in (5.39), these have been incorporated into the matrices Q_i^m. Thus, keeping the rotation orders fixed, the windows $\boldsymbol{h}$ and $\boldsymbol{g}$ which minimize (5.43) can be determined. To establish the most suitable domains for filtering, the optimization process is repeated for different combinations of *a* and *b*.

Since the cost function defined in (5.43) cannot be solved analytically, one has to resort to numerical optimization. Precisely, the 'Quasi-Newton' method was used among a multitude of unconstrained minimization algorithms available in commercial scientific packages (e.g. Matlab).

5.2.2.1 Experimental Results

To validate the above proposed approach, the example 2 (presented in Section 5.2) was again experimented upon. It can be seen from Figure 5-15, that this alternative approach was successfully applied and the obtained result is comparable to that of in Figure 5-13d. However, since this alternative approach is analytical, it has a higher computational complexity as compared to the iterative approach, discussed in Section 5.2.

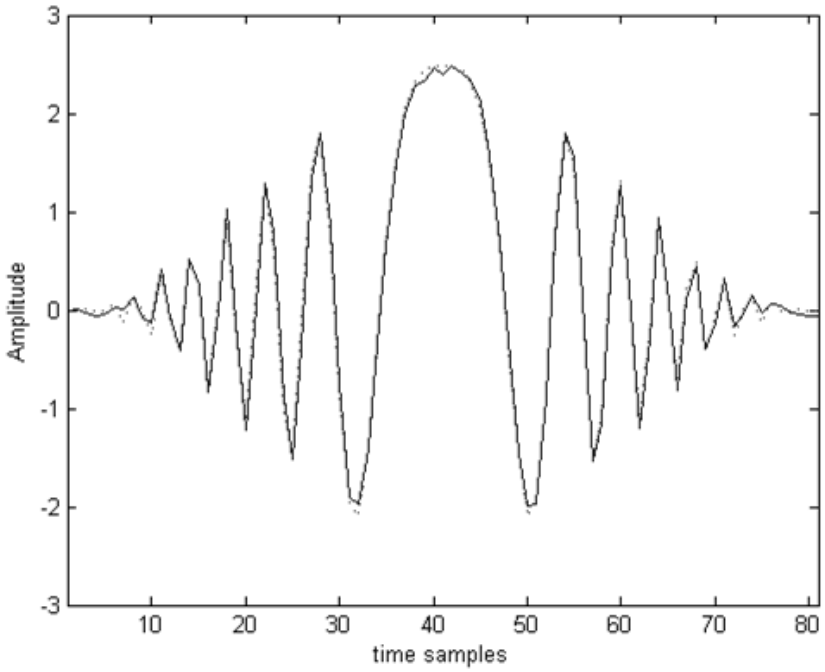

Figure 5-15 *Alternate estimate of example 2 obtained by filtering in the a = 1.35 and b = 0.55 domain (solid) and the desired signal (dotted).*

5.3 Summary/Key Contributions

The main focus of this chapter has been the optimization of an M-stage filtering configuration, in both conventional and fractional Fourier domains. The advantages of the methods proposed in this chapter can be summarised as follows:

- The MSE was estimated as the average square error over a number of realisations. This way, the use of the expectation operator in (4.2) and (5.23) was avoided, which eliminated the need to know – or make assumptions about – the statistics of the distortion. This was proven to be quite useful for the ECG denoising scheme presented in Section 5.1.2.1.
- A unique and novel formulation for an optimized M-stage fractional Fourier filtering configuration was presented for the first time in the literature, in Section 5.2.

- Discrete FrFT operators were directly engaged in the formulation of the optimisation problem in (5.22). Therefore, the rotation orders became defining design parameters, which were then explicitly determined.
- The objective function in Section 5.2.2 was compactly expressed in terms of a single variable which encompasses the individual modification windows. Thus, the optimized windows were obtained simultaneously.

References

[1] S.R. Subramaniam, Tsz K. Hon, Bingo Wing-Kuen Ling, and A. Georgakis, “Optimal Two-Stage Filtering of Elastograms”, 33rd Annual International Conference of the IEEE Engineering in Medicine and Biology Society (EMBC), 2011, Boston, Massachusetts.

[2] S.-C. Pei, and J.-J. Ding, “Fractional Fourier Transform, Wigner Distribution, and Filter Design for Stationary and Nonstationary Random Processes,” IEEE Transactions on Signal Processing, vol. 58, no. 8, pp. 4079-4092, Aug, 2010.

[3] N. Mohanty, Signal Processing. New York: Van Nostrand Reinhold, 1987.

[4] M.F. Erden, M.A. Kutay, and H.M. Ozaktas, “Repeated filtering in consecutive Fractional Fourier Domains and Its Application to Signal Restoration”, IEEE Trans. Sig. Proc., vol. 47, pp. 1458-1462, 1999.

[5] T. K. Hon, S. R. Subramaniam, A. Georgakis, and S. Alty, “STFT-based denoising of elastograms”, in Proc. IEEE Int. Conf. Acoust., Speech Signal Process. (ICASSP), Prague, Czech Republic, 2011.

[6] N.V. Thakor and Y. Zhu, "Applications of adaptive filtering to ECG analysis: Noise Cancellation and Arrhythmia Detection," IEEE Trans. Biomed. Eng., Vol. 38, No. 8, pp. 785-794, 1991.

[7] P.S. Hamilton, and M.G. Curley, “Adaptive Removal of Motion Artifact”, in Proc. IEEE Eng. in Med. and Biol., 1997.

[8] M.A.D. Raya, and L.G. Sison, “Adaptive Noise Cancelling of Motion Artifact in Stress ECG Signals Using Accelerometer”, in Proc. IEEE Eng. in Med. and Biol., 2002.

[9] G.B. Moody, R.G. Mark, and A. L. Goldberger, “PhysioNet: a Web-based resource for the study of physiologic signals”, IEEE Eng. Med. and Biol. Mag., vol. 20, no. 3, pp. 70-75, 2001.

[10] Y. F. Wu and R. M. Rangayyan, “An algorithm for evaluating the performance of adaptive filters for the removal of artifacts in ECG signals,” in Proc. 20th Canadian Conf. Elec. and Comp. Engineering, 2007.

[11] M. A. Kutay, H. M. Ozaktas, O. Arikan, and L. Onural, "Optimal filtering in fractional Fourier domains," IEEE Trans. Signal Process., vol. 45, no. 5, pp. 1129-1143, May 1997.

[12] B. A. Weisburn and R. G. Shenoy, "Time-frequency strip filters," in Proc. IEEE Int. Conf. Acoust., Speech, Signal Process. (ICASSP), May 7-10, 1996, vol. 3, pp. 1411-1414.

[13] S. R. Subramaniam, B. W.-K. Ling, and A. Georgakis, "Filtering in rotated time-frequency domains with unknown noise statistics", IEEE Trans. Signal Process., vol. 60, no. 1, pp. 489 - 493, January 2012.

Chapter 6

Conclusions & Future Work

6.1 Summary of Main Conclusions

The work presented in this thesis focused upon the novel concept of fractional Fourier-based filtering to design single, as well as multi-stage, serial filter configurations for the restoration of both simulated and real-world signals. The work has explored the fractional Fourier transform and examined some of its essential properties relating to filtering. Specifically, the concept of rotated domains in the joint time-frequency plane is detailed and further utilized to develop a variety of novel fractional Fourier-based filtering configurations for the treatment of various types of non-stationary signals. Prominent results of this work include the 2-stage fractional Fourier-based low-pass filtering circuit, and the optimized formulations of a single-stage, as well as an M-stage serial filtering system. The results presented in this thesis indicate that the new methods are superior to existing, advanced and conventional techniques. The main achievements of this thesis can be summarized as follows:

Fractional Fourier-Based Low-Pass Filtering Circuits

In Chapter 3, fractional Fourier-based low-pass filtering circuits have been presented for the first time in the literature, to deal with the scenario of denoising corrupted signals in real-world problems. Particularly, each filter circuit applied a time-varying low-pass cutoff

threshold, realized in distinct fractional Fourier transform domains, on the signals. Comparisons with current, conventional and advanced techniques showed that the proposed fractional Fourier-based filter circuits can recover a non-stationary signal from noise more effectively without distorting its useful features, i.e. edges or other transients of interest. This success was mainly attributed to certain key variables such as the FrFT orders, the applied filtering functions, and the structure of the filter circuit. In this work, these elements were specified in the time-frequency plane, based on the geometry of the designed cutoff frequency threshold. This was made possible by the choice of a simple triangular boundary, which in turn, was motivated by the spectral characteristics of the signals used. Additionally, it was also shown in Chapter 3, that there may exist more than one possible configuration for achieving the same filtering result as the proposed circuits.

Optimized Signal Estimator in FrFT-Based Serial Configurations

In Chapter 4, an optimized estimator operating in a single fractional Fourier domain is presented. The proposed solution produced an overall optimized pass band in the mean square sense. Similarly, in Chapter 5, a novel formulation for an optimized estimator operating in consecutive M-stage fractional Fourier domains is derived. Furthermore, through the presented formulation in Sections 4.1.2 and 5.2, the discrete FrFT operators were directly engaged in the optimisation problem. Therefore, the rotation orders became defining design parameters, which could be explicitly determined. Additionally, an alternative technique for optimizing a two-stage FrFT filtering system was also detailed. In this approach, the described objective function was compactly expressed in terms of a single variable that encompassed the individual modification windows. Thus, the optimized windows were obtained simultaneously. In fact, this thesis is the first in the

literature to present optimized formulations of systems operating in consecutive fractional Fourier domains.

Optimized Signal Estimation with Unknown Noise Models

Through the optimum estimators presented in Sections 4.1.2, 5.1.2 and 5.2, an alternative solution to that of in [1] is presented, which reduces the number of parameters that need to be known and minimize the relevant underlying assumptions. Specifically, the presented estimators do not require knowledge of the noise statistics or of any other degradation process, for that matter. This in turn may make it easier to apply these estimators in real-life signal processing problems. As an illustration of this notion, this principle has been successfully applied to filter experimentally acquired ECG data. The data contained electrode motion artifacts or 'em' noise, which had no statistical information whatsoever. Results indicated that the proposed technique was superior to existing conventional methods.

6.2 Future Work

Future extensions of the work presented in this thesis can be outlined as follows:

1) **Global optimized estimator**

   The resulting cost function associated with a typical M-stage filtering configuration turns out to be non-convex. As such, it may have several feasible regions, as well as multiple local minima within each region. To find the globally optimized solution of a given non-convex problem one could seek to progressively improve on previously determined local optima. The sequential search for better solutions can be performed rigorously by employing adaptively constructed auxiliary functions. The idea is to assist the optimization algorithm to escape from points of local

convergence, and find alternative solutions which get increasingly closer to the global optimum. Examples of this strategy could include the use of the tunnelling method [2], the bridging method [3] and the filled function [4]-[8].

2) **Optimizing the fractional order, *a***

Thus far, there are 4 ways in which one could obtain the most suitable fractional order (a_{opt}); they are:

- Direct measurements from the T-F plane (e.g. [9], [10])
- Based upon prior knowledge of a given signal (e.g. [11])
- Based on an exhaustive search of a given set (e.g. [1])
- Based on frequency content assessments through empirical algorithms (e.g. [12])

There might be another more efficient method in which the most suitable fractional order could be derived. This is based upon the decomposition of the fractional Fourier matrix defined in (2.21). Precisely, one can exploit the elegant structure of the FrFT matrix to just optimize the eigenvalues of (2.21), to produce an optimized fractional matrix.

3) **Signal-specific transformations**

In this thesis, a variety of methods have been presented to optimize the multiplicative windows used in fractional Fourier domains. The same methods could be applied for optimizing filters based in other linear-transform domains. The suitability of these transforms could be determined by experience. Ultimately, it would be interesting to derive a new approach in which the transform operator could be included as a minimization variable together with the filtering functions, such that the entire system can be optimized.

References

[1] M. A. Kutay, H. M. Ozaktas, and O. Arikan, “Optimal filtering in fractional Fourier domains,” IEEE Transactions on Signal Processing, vol. 45, no. 5, pp. 1129-1143, May, 1997.

[2] Yao, Y. (1989), Dynamic tunneling algorithm for global optimization, IEEE Transactions on Systems, Man, and Cybernetics 19, 1222-1230.

[3] Liu, Y. and Teo, K. (1999), A bridging method for global optimization, Journal of Australian Mathematical Society Series B 41, 41-57.

[4] R. P. Ge and Y. F. Qin, "A class of filled functions for finding global minimizers of a function of several variables," J. Optim. Theory Appl., vol. 54, no. 2, pp. 241-252, 1987.

[5] R. Ge, "A filled function method for finding a global minimizer of a function of several variables," Math. Program., vol. 46, pp. 191-204, 1990.

[6] X. Liu, "Finding global minima with a computable filled function," J. Global Optim., vol. 19, pp. 151-161, 2001.

[7] Y. Zhang, Liansheng, and Y. Xu, "New filled functions for nonsmooth global optimization," Appl. Math. Model., vol. 33, pp. 3114-3129, 2009.

[8] Charlotte Yuk-Fan Ho, Bingo Wing-Kuen Ling, Lamia Benmesbah, Ted Chi-Wah Kok, Wan-Chi Siu, and Kok-Lay Teo, “Two-Channel Linear Phase FIR QMF Bank Minimax Design via Global Nonconvex Optimization Programming,” IEEE Transactions on Signal Processing, pp. 4436-4441, vol. 58, no. 8, 2010.

[9] S.-C. Pei, and J.-J. Ding, “Relations between Gabor transforms and fractional Fourier transforms and their applications for signal processing,” IEEE Transactions on Signal Processing, vol. 55, no. 10, pp. 4839-4850, Oct, 2007.

[10] S.-C. Pei, and J.-J. Ding, “Fractional Fourier Transform, Wigner Distribution, and Filter Design for Stationary and Nonstationary Random Processes,” IEEE Transactions on Signal Processing, vol. 58, no. 8, pp. 4079-4092, Aug, 2010.

[11] C. Capus and K. Brown, “Short-time fractional fourier methods for the time-frequency representation of chirp signals,” J. Acoust. Soc. Am., vol. 113, pp. 3253–3263, 2003.

[12] A. Georgakis, and S.R. Subramaniam, “Estimation of the second derivative of kinematic impact signals using fractional Fourier filtering”, IEEE Trans. Biomed. Eng., vol. 56, pp. 996-1004, 2009.